Search for Type-III Seesaw heavy leptons using proton-proton collisions at $\sqrt{s} = 13$ TeV with the ATLAS detector

Relatore: Presentata da:
Prof. Maximiliano Sioli   Giuseppe Carratta

Correlatori:
Dott.ssa Giulia Ucchielli
Dott. Matteo Franchini

Sommario

La scoperta delle oscillazioni di sapore dei neutrini comporta una massa non nulla per queste particelle. Masse così piccole risultano difficili da spiegare in maniera naturale attraverso un puro accoppiamento di Yukawa con il campo di Higgs, come per gli altri fermioni.

Il meccanismo Type-III Seesaw è un'estensione del Modello Standard che introduce almeno due nuovi tripletti di campi fermionici con ipercarica nulla nella rappresentazione aggiunta del gruppo $SU(2)_L$, rappresentati da due leptoni carichi pesanti di Dirac e un leptone neutro pesante di Majorana.

In questo elaborato, la ricerca dei leptoni pesanti è stata eseguita basandosi sul processo $pp \to W^* \to L^\pm N^0 \to W^\pm \nu W^\pm \ell^\mp$ usando i dati raccolti dal rivelatore dell'esperimento ATLAS a energie del centro di massa $\sqrt{s} = 13$ TeV con una luminosità integrata di 79.8 fb^{-1}. Le potenzialità di questo canale puramente leptonico sono dovute alla capacità di rigetto di molti processi di fondo del Modello Standard.

Non è stato trovato alcun eccesso rispetto alle predizioni del Modello Standard, per cui è stato possibile stabilire un limite inferiore sulla massa dei leptoni pesanti di 419 GeV con un livello di confidenza del 95%.

Abstract

The discovery of neutrino flavour oscillations implies non-null masses for these particles. The smallness of neutrino masses is difficult to accommodate in a natural way through a pure Standard Model Yukawa coupling to the Higgs field.

Type-III SeeSaw mechanism extends the Standard Model, introducing at least two new triplets of fermionic fields with zero hypercharge in the adjoint representation of $\mathrm{SU(2)_L}$, resulting in two heavy Dirac charged leptons and a heavy Majorana neutral lepton.

In this work, the search for heavy leptons based on the $pp \to W^* \to L^{\pm}N^0 \to W^{\pm}\nu W^{\pm}\ell^{\mp}$ process and using the data collected by ATLAS detector at $\sqrt{s} = 13$ TeV with an integrated luminosity of 79.8 fb^{-1}, is performed. The power of the fully leptonic channel lies in the low expected background from Standard Model processes.

No excess over the Standard Model predictions is found and a lower limit on the heavy leptons mass is set at 419 GeV at 95% confidence level.

CONTENTS

IV

LIST OF FIGURES

VII

LIST OF TABLES

INTRODUCTION

The Standard Model (SM) of particle physics represents the most complete theory describing the behaviour of fundamental constituents of matter and their interactions. It was finalized in the second half of the XX century and it is today greatly supported by experimental evidence.

The mechanism through which neutrinos acquire their mass is not included in the SM. In the SM all fermions are massless and the mass is given only by Yukawa couplings with the Higgs field, involving fermion chiralities. The neutrino case is instead special because only left-handed neutrinos have been observed up to now. Furthermore, one of the most puzzling feature of particles physics is the lightness of neutrino masses with respect to those of the charged leptons. With the discovery of neutrino oscillations it became clear that neutrinos are not massless, although they have a very small mass compared to the charged lepton ones. This peculiar mass hierarchy is a theory issue known as "naturalness problem". In this context, the Type-III SeeSaw mechanism provides an elegant way to explain the origin of neutrino masses. This model predicts the existence of a new heavy degrees of freedom, represented by the introduction of a new heavy fermionic triplet with zero hypercharge in the adjoint representation of $SU(2)_L$. If these new mediators are light enough, around the TeV scale, it is possible to observe their signature at the Large Hadron Collider (LHC) energies.

The LHC, located at CERN laboratories in Geneva, is the largest and most powerful particle accelerator in the world and it reaches nowadays energies of 13 TeV in the center-of-mass of the colliding protons, allowing the search for beyond SM processes at TeV energy scales.

The search here presented uses the data collected by the ATLAS detector, a multi-purpose particle detector placed along the LHC tunnel. The ATLAS Collaboration already presented the results of a search for Type-III Seesaw heavy leptons in the final state with two light leptons, two jets and two neutrinos. Here an anal-

ysis in the three-lepton final state at 13 TeV in the context of Type-III Seesaw models with ATLAS is performed for the first time. This analysis is restricted to heavy leptons decay into W bosons, and paves the way to a more general and complete analysis with all the decay channels. Data collected by the ATLAS detector during 2015, 2016 and 2017 in LHC pp collisions at a center-of-mass energy of $\sqrt{s} = 13$ TeV are used. Unlike the two leptons topology, the large E_T^{miss} in the three-lepton final state does not allow to reconstruct the main variables of the analysis. To optimize the significance, a dedicated study aimed to maximize the significance in the phase space region was carried out.

The first chapter of this thesis presents the theoretical framework: the Standard Model, a brief description of neutrino physics and the Seesaw mechanism. The second chapter describes the LHC collider and the main features of the ATLAS detector. The third chapter introduces the description of the objects reconstructed with ATLAS and the identification techniques. The last chapter reports the details and the results of the search for Type-III Seesaw heavy lepton production in the three-lepton final state.

CHAPTER 1

THEORETICAL FUNDAMENTA

1.1 The Standard Model

The study of the Universe and the matter that composes it led to the formulation of the *Standard Model of Particle Physics* (SM) that describes elementary particles, the building blocks of Nature, and their interactions, in terms of a *gauge theory* [1]. SM is a quantum field theory (QFT), namely its fundamental objects are treated as *quantum fields* defined everywhere in the space-time. It describes the both strong interactions, via *Quantum Chromodynamics* (QCD) [2], and electroweak interactions (EW) by the Glashow [3]-Weinberg [4]-Salam [5] model[1]. In the SM, every interaction between matter fields is described by a *local gauge symmetry*, that consists in an exchange of bosons, called *mediator bosons* or *gauge bosons*.

The SM is based on the gauge group:

$$SU(3)_C \otimes SU(2)_L \otimes U(1)_Y \tag{1.1}$$

where $SU(3)_C$ describes, through a non-Abelian group, the strong interaction caused by the colour charge; $SU(2)_L \otimes U(1)_Y$ represent the GWS theory, in which the special unitary group $SU(2)_L$ is associated to the weak isospin while the unitary group $U(1)_Y$ is associated to the weak hypercharge.

Using Lie's Algebra groups[2] it is possible to find the number of generators for every groups, that corresponds to the number of gauge bosons:

$SU(3)$**:** 8 generators, corresponding to the *gluons*;

$SU(2)$**:** 3 generators, corresponding to gauge fields, W_i;

---

[1]Gravitational force is not included in the SM.

[2]For a Lie group like $SU(n)$ there are $n^2 - 1$ generators, for $U(n)$ are n^2.

$U(1)$: 1 generators, corresponding to gauge field, B.

The fields associated to the *physical* bosons ($W^\pm$, Z^0, γ) are linear combinations of the gauge fields W_i and B. The symmetry group in (1.1) requires that all bosons should be massless, however it is proved that the weak interactions mediators $W^\pm$ and Z^0 have a mass of 80 GeV and 91 GeV respectively. The explanation for weak bosons and fermion masses was provided by three theorist: Higgs, Englert and Brout. They used a new mechanism, *Spontaneous Symmetry Breaking* (SSB) [6], that introduces a neutral scalar field, named Higgs field, giving mass to all of the SM fundamental particles.

1.1.1 Building blocks of the theory

SM classifies particles into fermions, the bricks of matter, and bosons, the mediators of the forces.

Fermions, spin 1/2 particles including leptons and quarks, follow Fermi-Dirac statistics and obey the Pauli exclusion principle. Leptons are formalized into a leptonic doublets structure with the corresponding neutrinos:

$$\begin{pmatrix} e \\ \nu_e \end{pmatrix} \begin{pmatrix} \mu \\ \nu_\mu \end{pmatrix} \begin{pmatrix} \tau \\ \nu_\tau \end{pmatrix}$$

where for each lepton family it is associated a leptonic number (electronic, muonic, tauonic) with a value of $+1$ (for leptons) and -1 (for anti-leptons), conserved in all interactions. All leptons have a negative charge (positive for anti-leptons), and they can interact via electromagnetic or weak force. Neutrinos, being electrically neutral, only feel weak interactions.

Similarly to leptons, quarks are divided into three generations via weak isospin:

$$\begin{pmatrix} u \\ d \end{pmatrix} \begin{pmatrix} c \\ s \end{pmatrix} \begin{pmatrix} t \\ b \end{pmatrix}$$

formed *up-type* (u, c, t), and *down-type* (d, s, b) quarks having respectively a charge[3] of 2/3 and $-1/3$ of the electron charge Q_e[4]. Quarks can interact via strong, electromagnetic and weak interactions. They are the constituents of hadrons, which can be divided into *mesons* ($q\bar{q}$ states) and *baryons* (qqq states). Quarks are characterized by a color quantum number (*red, blue, green*) corresponding to the strong interaction charge. Color quantum number is conserved in every interaction. Furthermore all quarks have a barionic quantum number of 1/3 ($-1/3$ for the anti-quarks), addictive and conserved by the three fundamental interactions included in

---

[3] Quarks are the only particles with a fractional charge.
[4] $Q_e = -1.6022 \cdot 10^{-19}$ C

the SM. They also have six flavour quantum numbers (up, down, charm, strange, top, bottom) conserved in all the interactions but the weak force.

Bricks (leptons) are "cemented" together by bosons, the quanta of force quantum fields. They follow Bose-Einstein statistics, have an integer spin and are also called *vector bosons*. The bosons in the SM are: As shown in Table 1.1, only the

Interaction	Mediator	Mass (GeV/c^2)	Spin	Charge (in units of Q_e)
Strong	Gluons	0	1	0
Weak	$W^\pm$	80,385 $\pm$ 0,015	1	± 1
Weak	Z^0	91,1876 $\pm$ 0,0021	1	0
Electromagnetic	γ	0	1	0

Table 1.1: Main features of the vector bosons [7].

weak force has massive bosons, and for this reason it has a so short interaction range (see Table 1.2). In Figure 1.1 it is reported the current structure of SM, with the addition of heavy leptons searches by Type-III SeeSaw mechanism, objects of this thesis.

1.2 Funtamental Forces

In a quantum field theory like the SM, the four fundamental interactions, electromagnetic, weak, strong and gravitational, are described by coupling fields with particles. The gravitational force is not included in the theory of SM because of it is not renormalizable. This does not change SM predictions since its contribution is negligible at small scales at the present colliding energies.

Interactions are distinguished in terms of their magnitude and their range. The first is used to compare the intensity of the four forces; the second defines the maximum distance at which the interaction can be felt by particles. These features are quoted in Table 1.2: All of these interactions are included in the SM by a mathematical formalism called *gauge theory* based on the concept of *symmetry*. It means that the Lagrangian is invariant under specific transformation (i.e. translation, rotation, time). According to this theory the SM Lagrangian is invariant for both global and local transformation. Symmetries are divided into:
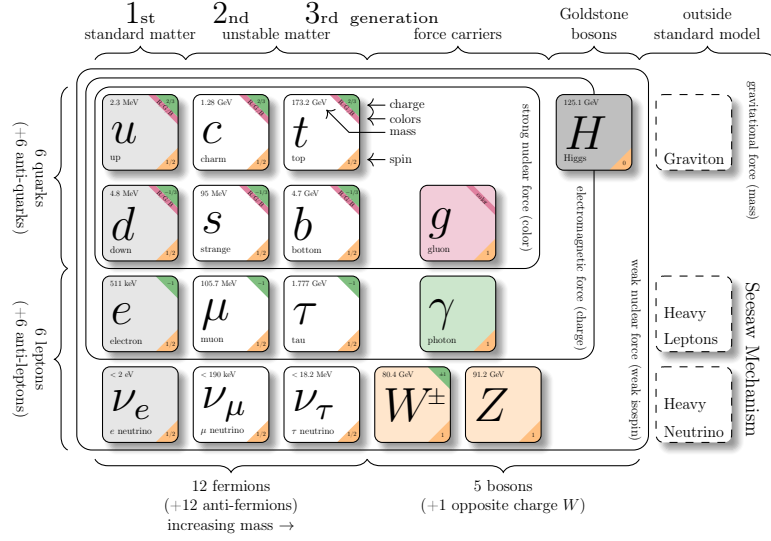
Figure 1.1: Constituents of the SM. Starting from left: fermions (left part), divided into quarks (upper part) and leptons (bottom part), gauge bosons (right part), including the Higgs boson, and particles outside the SM as the graviton or the heavy leptons predicted by the SeeSaw mechanism.

	Strong	Electromagnetic	Weak	Gravitational
Range(m)	10^{-15}	∞	10^{-18}	∞
Magnitude	1	10^{-2}	10^{-6}	10^{-39}

Table 1.2: Main characteristics of the fundamental forces [1].

Global symmetry: Lagrangian is invariant under a transformation who changes the fields of the same quantity in every point of the space-time;

Local symmetry: in this case the transformation depends by a parameter locally defined.

The basic idea of gauge theories was laid by Maxwell in 1864 when he unified the electric and magnetic interactions. This was possible because the electromagnetic potential, generator of fields that comply Maxwell's equation, is not uniquely defined. This is a manifestation of the *gauge invariance*: many different potentials lead to the same fields and physics, without changing the resulting interaction.

1.2.1 The electromagnetic interaction

The quantum field theory describing the electromagnetic interaction is called *Quantum Electrodynamics* (QED). It describes how light (*photons*) and electrically charged matter (*electrically charged particles*) interact; it is one of the most complete quantum theory and for its extremely accurate predictions was called, by R.Feynman, "*the jewel of physics*" [8].

QED is derived by Maxwell's equations, reinterpreted in quantomechanical and relativistic terms. To obtain the QED Lagrangian for matter fields $\psi(x)$, we can start from the Dirac Lagrangian (1.2) for free particles of spin $1/2$ ψ:

$$\mathcal{L}_D = \bar{\psi}(i\gamma^\mu \partial_\mu - m)\psi \tag{1.2}$$

where m is the particles' mass and γ^μ the Dirac matrices [1]. It is required invariance with respect to a local (and then a global) gauge phase rotation of $U(1)$ group associated to the electric charge as:

$$\psi \to \psi' = e^{-\alpha(x)}\psi \tag{1.3}$$

where $\alpha(x)$ is an arbitrary phase. It is easy to see that equation (1.2) is invariant under a global phase rotation, a continuous function that does not depend on x. Thus, through Noether's theorem, charge is conserved. By substituting derivative operator ∂_μ with the *covariant derivative D_μ*:

$$\partial_\mu \to D_\mu = \partial_\mu + iqA_\mu \tag{1.4}$$

the invariance under (1.3) is introduced, with also the addition of the electromagnetic vector potential A_μ. The Lagrangian is then invariant independently on the choice of $\alpha(x)$. So the final form of QED Lagrangian is given combining (1.2) with (1.4) and adding also a kinematic term for the vector field, which describes the propagation of free photons:

$$\begin{aligned}
\mathcal{L}_{QED} = &\bar{\Psi}(i\gamma^\mu \partial_\mu - m)\psi &&\to \quad \textit{Propagation of free fermion} \\
&-\frac{1}{4}F_{\mu\nu}F^{\mu\nu} &&\to \quad \textit{Propagation of free photon} \\
&-J^\mu A_\mu &&\to \quad \textit{Interaction between gauge and matter field}
\end{aligned} \tag{1.5}$$

where J^μ is the conserved electromagnetic current and F_μ the Maxwell's electromagnetic tensor, with the form:

$$J^\mu = q\bar{\psi}\gamma^\mu\psi \tag{1.6}$$

$$F_{\mu\nu} = \partial_\mu A_\nu - \partial_\nu A_\mu. \tag{1.7}$$

A mass term for the photon of the type (1.8):

$$\mathcal{L}_\gamma = \frac{1}{2}m^2 A^\mu A_\mu \tag{1.8}$$

$$A^\mu A_\mu \to (A^\mu - \partial^\mu \alpha)(A_\mu - \partial_\mu \alpha) \neq A^\mu A_\mu \tag{1.9}$$

would violate the local gauge invariance (1.9). Therefore, the vector field associated to the photon is massless. Some QED processes are shown Figure (1.2).
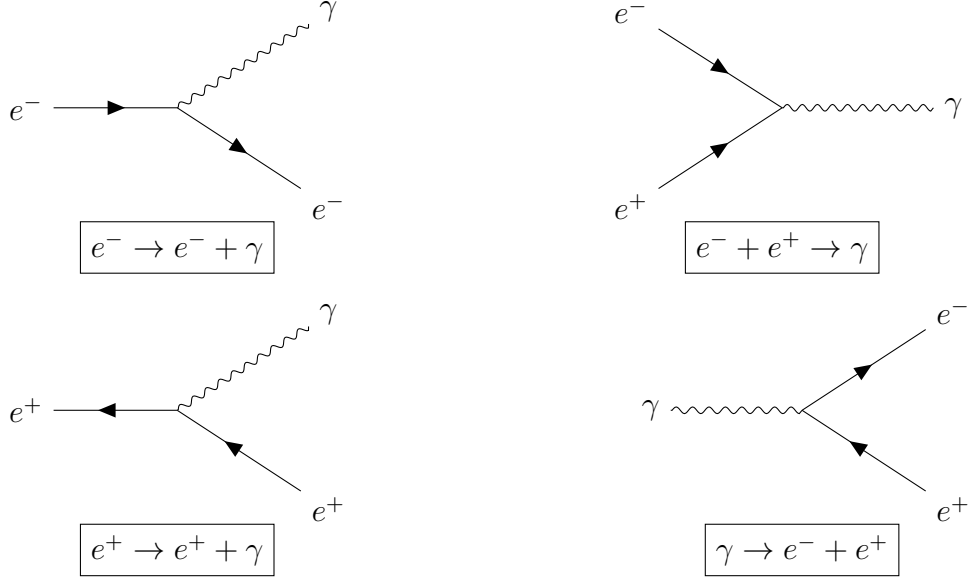
Figure 1.2: The diagrams illustrate basic processes that may occur in positron and electron interactions with a photon. They are: fundamental QED vertex (*top left*); electron-positron annihilation (*top right*); emission of a photon by a positron (*bottom left*); pair production by a photon (*bottom right*).

1.2.2   The weak interactions

Every SM fermion feels weak interactions. Because of its low magnitude, as reported in Table (1.2), it emerges only when others interactions are suppressed. First theoretical developments of the weak theory was laid by the Italian physicist *Enrico Fermi* in 1934 when he tried to explain the nuclear β-decay (see diagrams in Figure 1.3) as a punctual interaction of four fermions [9]. This type of interaction was very interesting for its peculiarity of changing the flavour of particles.

The quantum field theory describing the weak interaction is the *Quantum Flavor-Dynamics* (QFD), which is symmetric with respect to a gauge rotation of $SU(2)_L$. It has 3 generators associated to the physical vector bosons W^+, W^-,

Z^0 (Figure 1.3). Processes mediated by W bosons are called charge current (CC) interactions; if a Z boson exchange occurs, the process is called neutral current (NC) interaction.

Fermi's theory predicted, in analogy with the electromagnetic field, a vectorial (V) propagator exchanged between two particles, but this type of current alone was not enough to explain parity violation experimentally observed. So it was necessary to include an axial (A) term in the weak Hamiltonian to guarantee the Lorentz-invariance. The Hamiltonian with the V-A terms has the form:

$$H_{V-A} = \frac{G}{\sqrt{2}} \left[\bar{\psi}_p \gamma^\mu (1 - \gamma^5) \psi_n \right] \left[\bar{\psi}_e \gamma^\mu (1 - \gamma^5) \psi_\nu \right] \tag{1.10}$$

where G is the Fermi coupling constant. Defining the chirality projector operators:

$$\psi_L = \frac{1 - \gamma^5}{2} \psi \qquad \rightarrow \quad \text{Left component} \tag{1.11}$$

$$\psi_R = \frac{1 + \gamma^5}{2} \psi \qquad \rightarrow \quad \text{Right component} \tag{1.12}$$

with γ^5 chirality operator defined as $\gamma^5 = i\gamma^0\gamma^1\gamma^2\gamma^3$ [1], we can understand that the presence of $(1 - \gamma^5)$ term in the (1.10) selects only "left-handed" (LH) particle and "right-handed"(RH) anti-particle in a weak coupling. Then, SM permits only interactions between LH particles and RH anti-particles.
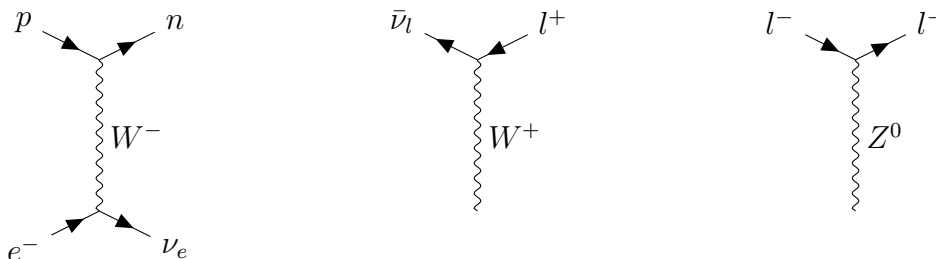
Figure 1.3: Feynman diagrams for: the β-decay (*left*); funtamental vertex of weak interaction in CC (*center*) and in NC (*right*).

1.2.3 The Electroweak Interaction

In the early '60s Glashow, Weinberg and Salam started to search a way to unify the electromagnetic and weak interactions. This was possible in 1968 with their formulation of *electroweak theory*. This force is described by a Lagrangian, invariant under a local gauge transformation, based on the $SU(2)$ group of the weak

isospin T and the $U(1)$ group of the weak hypercharge Y, defined by the Gell-Mann–Nishijima formula:

$$Q = T_3 + \frac{Y}{2} \tag{1.13}$$

where T_3 is the third component of the weak isospin and Q is the electric charge.

The interaction term between the three W vector bosons of $SU(2)$ group and B vector boson of $U(1)$ can be written as:

$$\mathcal{L} = -\frac{1}{4} F^{\mu\nu i} F^i_{\mu\nu} - \frac{1}{4} G^{\mu\nu} G_{\mu\nu} \tag{1.14}$$

where $i = 1, 2, 3$ and the field strength tensors are equal to:

$$F^i_{\mu\nu} = \partial_\mu W^i_\nu - \partial_\nu W^i_\mu - g\epsilon_{ijk} W^j_\mu W^k_\nu \tag{1.15}$$

$$G_{\mu\nu} = \partial_\mu B_\nu - \partial\nu B_\mu \tag{1.16}$$

With these four gauge bosons it is possible to write the mass eigenstates for the physical bosons of the weak and electromagnetic force:

$$W^\pm_\mu = \frac{(W^1_\mu \mp iW^2_\mu)}{\sqrt{2}} \tag{1.17}$$

$$Z_\mu = -B_\mu \sin(\theta_W) + W^3_\mu \cos(\theta_W) \tag{1.18}$$

$$A_\mu = B_\mu \cos(\theta_W) + W^3_\mu \sin(\theta_W) \tag{1.19}$$

where θ_W is the Weinberg angle which is equal to about $30°$ [7]. It is also introduced a difference between the Z^0 and $W^\pm$ masses due to the Weinberg angle:

$$M_W = M_Z \cdot \cos\theta_W. \tag{1.20}$$

The last piece of the electroweak theory was the introduction of the quark sector, which has different coupling mechanism compared to leptons. This was confirmed by K-meson decay: $K^0(d\bar{s}) \rightarrow \pi^-(d\bar{u})\ell^+\nu_l$ [10] , which involves a variation of the strangeness quantum number due to an interaction among quarks of different families (s and u). This phenomenon was explained by Cabibbo with the *mixing of quarks* [11], which describes the eigenstates of weak interaction as a linear combination of the eigenstates of mass. This theory was generalized by Kobayashi and Maskawa [12] with the *CKM-matrix* (1.21) including all the six quarks with an unitary 3×3 matrix:

$$\begin{pmatrix} d' \\ s' \\ b' \end{pmatrix} = \begin{pmatrix} V_{ud} & V_{us} & V_{ub} \\ V_{cd} & V_{cs} & V_{cb} \\ V_{td} & V_{ts} & V_{tb} \end{pmatrix} \begin{pmatrix} d \\ s \\ b \end{pmatrix} \tag{1.21}$$

1.2.4 The strong interaction

Quantum Chromo-Dynamics (QCD) [13] describes strong interactions between quarks and gluons and how they are bound in hadrons. To explain the existence and the composition of hadrons, the *color* -a new quantum number- is introduced. Colour can assume three possible values, so quarks are described by a three Dirac spinor fields. Only quarks and gluons have color charge, so only these particles experience the strong interaction. This theory is described by the symmetry group $SU(3)$, whose generators are defined by the Gell-Mann matrices [1]. QCD invariance under global gauge transformations leads to the colour charge conservation. From the Dirac Lagrangian (1.2) we can write the $SU(3)$ Lagrangian using the gauge principle:

$$\mathcal{L} = \bar{\psi}^\alpha \left(i\slashed{D}^{\alpha\beta} - m\delta^{\alpha\beta} \right) \psi^\beta \tag{1.22}$$

In order to guarantee the local gauge invariance of (1.22) we introduce the covariant derivative in the fundamental representation of the $SU(3)$ group, in analog with (1.4):

$$D_\mu^{\alpha\beta} = \delta^{\alpha\beta}\partial_\mu + ig_s A_{\mu a}(T^a)^{\alpha\beta} \tag{1.23}$$

where T^a are the group generators, $\delta^{\alpha\beta}$ the Kronecker function, g_s the coupling constant of QCD and A_μ the gluonic propagator. As the other QFT, also the QCD has a number of gauge bosons equal to the number of generators of the corresponding symmetry group. In this case they are eight particles called *gluons*. Their propagation is described in the same way of the QED boson (1.5) but with a different representation of the field (1.7):

$$F_{\mu\nu}^a = \partial_\nu A_\mu^a - \partial_\mu A_\nu^a + g_s f_{abc} A_\mu^b A_\nu^c \tag{1.24}$$

with f^{abc} fine structure constants of the group and the indices a, b, c indicate a sum on the eight colour degrees of freedom of the gluon field.

A field structure as (1.24) is typical of a non-abelian group which leads a gluon self-interaction. The final QCD Lagrangian can be written as:

$$\mathcal{L}_{QCD} = -\frac{1}{4}F_{\mu\nu}^a F_a^{\mu\nu} - \sum_{flavour} \bar{\psi}_f \left(\gamma^\mu D_\mu - m_f \right) \psi_f \tag{1.25}$$

The gluon self-interaction has also an effect on the strong coupling constant:

$$\alpha_s(q^2) = \alpha(\mu^2) \left[1 + \frac{\alpha_s(\mu^2)}{12\pi} \log\left(\frac{-q^2}{\mu^2}(2n_f - 11N) + O(\alpha_s^2) \right) \right] \tag{1.26}$$

where μ^2 is a spacelike renormalization point, n_f the number of quark flavours appearing in the loops, N the number of colours. In this equation there are two

opposite terms: one regarding the fermion loop which increases the coupling constant at short distance or large value of μ^2, the other one involves the three-gluon contribution that tends to decrease this coupling at short range (*antiscreening effect*) [14]. Given a region where $\alpha_s(q^2) \ll 1$, it is possible to find a condition to validate QCD perturbation theory. It indicates that at short range (high q^2), quarks can be considered as free particles inside hadrons, a property called *asymptotic freedom*. On the contrary, the enhancement of coupling constant at large distances implies a range where strong interaction becomes dominant. This is an indication of *confinement*, which keeps quarks and antiquaks together within hadrons. Confinement allows quark bound states to be only white (i.e. a quark of each color) or uncolor (i.e. color and the corresponding anti-color). Then, the confinement mechanism [14] provides a short range behaviour to the strong interaction even if its mediators are massless[5]. As consequence at low energies, where α_s is large, quarks and gluons have never been observed as free particles.

1.3   The Physics of Neutrino

The study of the β-decay spectrum, by Chadwick in 1914, motivated the hypothesis of a new particle. In this decay (Figure 1.3) the only detected particles were neutrons and electrons but, excluding a violation of the energy conservation, the process resembled a three body decay. In 1930, Pauli opposed to the violation of this physics fundamental and proposed his *desperate remedy* [15]:

> *Dear Radioactive Ladies and Gentlemen,*
> *… I have hit upon a desperate remedy to save the "exchange theorem" of statistics and the law of conservation of energy. Namely, the possibility that there could exist in the nuclei electrically neutral particles, that I wish to call neutrons, which have spin 1/2 and obey the exclusion principle...*

Pauli called this new particle "neutron", renamed "neutrino"[6] by Fermi in 1934 when he published his article about weak interactions "Tentativo di una teoria dell'emissione dei raggi beta" on the journal *Nuovo Cimento* [9].

The first experimental evidence of electronic neutrinos occurred in 1956, with the Reines-Cowan experiment at nuclear reactor placed in the Savannah River site, in the United States. A few years before, 1947 in Canada, Conversi, Pancini and

---

[5]Indeed the range of strong interaction is of the some order of magnitude of the nuclear radius. A part the top quark that is so unstable that it decays before hadronazing and form a bound state.

[6]Since the neutron was just discovered by Chadwick as the neutral particle which formed atomic nucleus together the proton.

Piccioni [16] realized an experiment where they saw a weakly interaction of muon with nuclei. This observation persuaded Pontecorvo to focus his studies on the physics of neutrino. First of all, he proposed the existence of a neutrino for each leptonic flavour, confirmed by the Lederman-Schwartz-Steinberger [17] experiment in the 1964 with the observation of the interaction of the muonic neutrino. In this context, Pontecorvo [18] had also the idea of the neutrino oscillations.

The first step to investigate their oscillation was the development of the Standard Solar Model (SSM), which predicts the magnitude of neutrinos flux coming from the Sun to the Earth. Because of the advanced technology required, an experimental observation of this phenomena has been made only in the second half of '90 by the Super-Kamiokande observatory [19]. Using the elastic scattering interaction, only one half of the number of electronic neutrinos is formed with respect to the number predicted by SSM. This flavour oscillation during propagation through the space is the evidence of the non-null masses of neutrinos.

The mechanism for which neutrinos acquire mass is not yet clear today. In the SM all fermions are massless and the mass is given only by a Yukawa coupling with the Higgs field, involving both the chiralities of fermions. The neutrino case is instead special because only the left-handed neutrinos have been observed up to now. Furthermore, neutrinos have a mass much smaller than the other fermions leading to a *naturalness problem* [20] that can be solved in different ways:

- introducing a new type of neutrino, called *sterile neutrino* [21], that can interact only through the gravitational force;

- considering a Majorana mechanism [22] to generate the mass of neutrino and requiring the neutrino matches with the anti-neutrino;

- with the introduction of a mechanism Beyond the SM, like the SeeSaw Mechanism [23].

The last two ways will be explained in this section.

1.3.1 Neutrino: Dirac or Majorana particle?

Dirac mass term

In the SM, all fermions obey the Dirac equation:

$$(i\gamma^\mu \partial_\mu - m)\psi = 0 \tag{1.27}$$

where ψ is a Dirac spinor with 4 components, which can be rewritten using the Weyl representation through two bi-dimensional spinors ϕ and χ describing the

left and right components of the Dirac field respectively:

$$\psi = \begin{pmatrix} \psi_1 \\ \psi_2 \\ \psi_3 \\ \psi_4 \end{pmatrix} = \begin{pmatrix} \phi \\ \chi \end{pmatrix} = \begin{pmatrix} \phi^+ \\ \phi^- \\ \chi^+ \\ \chi^- \end{pmatrix} = \left. \begin{pmatrix} \text{Spin} \uparrow \\ \text{Spin} \downarrow \\ \text{Spin} \uparrow \\ \text{Spin} \downarrow \end{pmatrix} \begin{array}{l} \Big\} \text{Particle} \\ \Big\} \text{Antiparticle} \end{array} \right. \tag{1.28}$$

where there are particle and antiparticle states which represent two states, one for every spin orientation, with positive energies and two with negative energies. The impossibility for a free particle to transport $E < 0$ was solved by the reinterpretation of anti-particle states with $E > 0$.

Using the chirality projectors in (1.11)-(1.12), the Dirac Lagrangian (1.2) becomes:

$$\mathcal{L} = (\bar{\psi}_L + \bar{\psi}_R)(i\gamma^\mu \partial_\mu - m)(\psi_L + \psi_R). \tag{1.29}$$

The term we are interested in is related to the mass of fermion:

$$\bar{\psi}_L m \psi_L + \bar{\psi}_R m \psi_R + \bar{\psi}_L m \psi_R + \bar{\psi}_R m \psi_L. \tag{1.30}$$

In can be shown by applying the Dirac matrix properties, that the first two terms are null:

$$\begin{aligned} \bar{\psi}_L m \psi_L = \psi_L^\dagger \gamma_0 m \psi_L &= \psi^\dagger \left(\frac{1 - \gamma^5}{2} \right) \gamma_0 m \left(\frac{1 - \gamma^5}{2} \right) \psi \\ &= \psi^\dagger \gamma_0 m \left(\frac{1 + \gamma^5}{2} \right) \left(\frac{1 - \gamma^5}{2} \right) \psi = \\ &= \psi^\dagger \gamma_0 m \left(\frac{1 - (\gamma^5)^2}{4} \right) \psi = 0 \end{aligned} \tag{1.31}$$

Separating the chiral components of the fields, equation (1.27) splits into two coupled equations:

$$i\gamma^\mu \partial_\mu \psi_L = m \psi_R \tag{1.32}$$
$$i\gamma^\mu \partial_\mu \psi_R = m \psi_L \tag{1.33}$$

So it is clear that to describe a massive fermion with the Dirac equation, it must have four non-nulls chiral projectors. Due to the complete parity violation of the weak interaction, these chiral projectors are not observables and are labelled as "sterile fields".

Majorana mass term

To build a Majorana mass term for neutrinos, we can start from equations (1.32) and (1.33) assuming a massless fermion field ψ. Now these equations are decoupled

into two *Weyl equations* [1]:

$$i\gamma^\mu \partial_\mu \psi_L = 0 \quad , \quad i\gamma^\mu \partial_\mu \psi_R = 0 \tag{1.34}$$

which prove that a massless fermion can be described by a single chiral field. Given also the ansatz about the dependence of the chiral components ψ_L and ψ_R among them, we can assume the two equations (1.32) and (1.33) as two ways to write the same equation with one independent chiral field.

Taking the hermitian of (1.32) multiplied from the right for γ_0, we have:

$$-i\gamma^\mu \partial_\mu \bar{\psi}_R^T = m\bar{\psi}_L \tag{1.35}$$

To have an equation similar to the Dirac coupled equation, we have to transpose the (1.35) and applying the charge conjugation matrix $\mathcal{C}$, so:

$$-i\gamma^\mu \partial_\mu \mathcal{C}\bar{\psi}_R^T = m\mathcal{C}\bar{\psi}_L \tag{1.36}$$

where ψ_R has to satisfy:

$$\psi_R = \xi\mathcal{C}\bar{\psi}_L^T \tag{1.37}$$

with ξ arbitrary phase. This is the condition proposed by Majorana to describe fermions and anti-fermions in the same spinor, which means considering a particle as its anti-particle.

Neglecting the arbitrary phase ξ, we can write the spinor ψ as:

$$\psi = \psi_R + \psi_L = \mathcal{C}\bar{\psi}_L^T + \psi_L = \psi_L^c + \psi_L \tag{1.38}$$

which implies:

$$\psi = \mathcal{C}\bar{\psi}^T = \psi^c \tag{1.39}$$

The (1.39) proves that a Majorana particle must have a neutral charge. So the only fermion that can be described by the Majorana equation is the *neutrino*.

In analogy to the Weyl description, the temporal evolution of the Majorana equation is described by a two components spinor by the substitution of (1.37) into (1.32):

$$i\gamma^\mu \partial_\mu \psi_L = m\xi\mathcal{C}\bar{\psi}_L^T \tag{1.40}$$

Finally, we can rewrite the Majorana Lagrangian mass term as:

$$\mathcal{L} = -\frac{1}{2}m\psi_L\mathcal{C}\bar{\psi}_L^T + h.c. \tag{1.41}$$

This shows the possibility to introduce a mass term without the presence of right-hand chiral component. The factor $1/2$ distinguishes a Majorana from a Dirac Lagrangian and it is required in order to avoid double counting of the dependent fields ψ_L^c and ψ_L when obtaining the equation of motion for Majorana neutrinos.

Since the field ψ_L belongs to the $SU(2)$ doublet ψ, the Majorana mass term would violate the isospin conservation by one unit which would make it difficult to be included in the SM. To solve this problem, Weinberg introduced the operator $\mathcal{O}_5$:

$$\mathcal{O}_5 = \left(\bar{\phi}^\dagger \psi_L\right)^T \mathcal{C} \left(\bar{\phi}^\dagger \psi_L\right) \tag{1.42}$$

where ϕ is the SM Higgs field. It allows to reach the structure upon electroweak symmetry breaking. The Weinberg operator is a 5-dimensional operator, which is not renormalizable. This problem is solved interpreting $\mathcal{O}_5$ as an effective operator produced at low energies by a new physics (NP) mechanism at higher energy scales [24]. An important property of the Weinberg operator is that it can be constructed with SM fields alone.
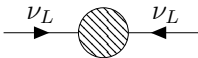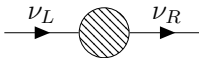
	Majorana	Dirac
Physical State	$\psi = \psi_L + \psi_L^c$	$\psi = \psi_L + \psi_R$
Mass term	$m^M \psi^T \psi = \frac{1}{2} m^M \psi_L^c \psi_L + \text{h.c.}$ $\nu_L \to \bigotimes \leftarrow \nu_L$	$m^D \bar{\psi}\psi = m^D \bar{\psi}_R \psi_L + \text{h.c.}$ $\nu_L \to \bigotimes \to \nu_R$
Lepton Number Variation	$\Delta L = 2$	$\Delta L = 0$
Required Scales	$m \sim yv^2/\Lambda \quad \to \quad \Lambda \sim 10^{15}$ GeV	$m \sim vy \quad \to \quad y \sim 10^{-12}$
U_{PMNS} parameters	3 angles θ_{ij} 3 $C\!\!\!/P\!\!\!/$ phases δ, α, β	3 angles θ_{ij} 1 $C\!\!\!/P\!\!\!/$ phase δ

Table 1.3: Comparison of Dirac and Majorana mass terms. Λ is a new physics mass scale where Majorana neutrinos could acquire its mass, y the Yukawa Couling, v is the vacuum expectation value (vev). PMNS matrix is the equivalent of CKM matrix for the leptonic sector.

1.3.2 The current situation

It is sure by now that neutrino has a non-null mass, but after more than 50 years of neutrino physics, a lot of questions remain without an answer.

In Figure (1.4) are reported the value measured by Super-Kamiokande (atmospheric neutrinos) and KamLAND (solar neutrinos) related to the masses squared difference[7]. They imply, at least, two different neutrinos masses larger than zero.

---

[7]Solar neutrinos are produced by various nuclear fusion in the Sun, mainly in the proton-proton reaction. Atmospheric neutrinos are produced in the interaction between cosmic-ray and

Are these masses are described by Dirac or Majorana equation? This is one of the fundamental questions. Neutrinoless double β-decay experiments [25] are among the most promising possibilities to provide us with an answer. Its observation would represent an evidence of the Majorana neutrinos because of their mass term violates the conservation of the leptonic number by two units (see Table 1.3).

Nowadays it is clear that neutrinos have masses, but their generation mechanism is unknown yet. The SM is not able, at present, to account for neutrino masses. They are much smaller then the other charged leptons by six or more orders of magnitude. For this reason, to acquire mass with the Higgs Mechanism, a high Lagrangian corrections (i.e. *fine tuning*) are needed. Fine tuning of physical parameters turns into a *naturalness problem*. Tiny neutrino masses might manifest from new physics beyond SM with a high-energy scale Λ_{NP}. One of the most natural explanation appears to be one offered by the *SeeSaw mechanism*, explained in the next section.

A CP violation is also searched, with the value of the CP phase which is present in the neutrinos mixing matrix (U_{PMNS}).

An extensive experimental program aims to solve all the just highlighted open points. Here we focus on a possible mechanism for mass generation.
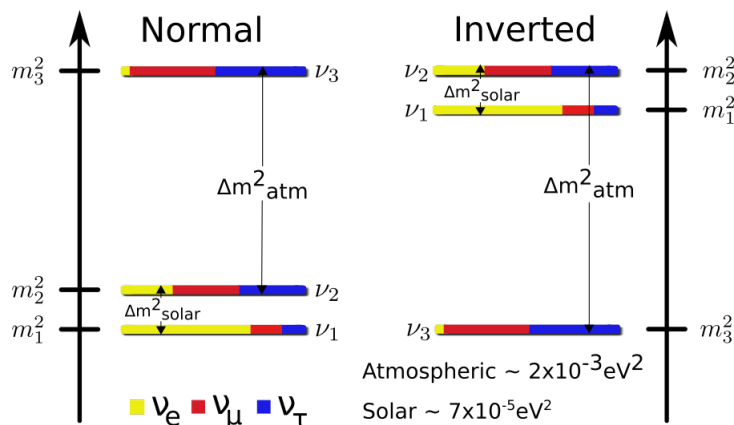
Figure 1.4: Normal versus inverted hierarchy of the neutrino mass.

1.4 Beyond the SM: SeeSaw Mechanism

One of the best known models to achieve the neutrino mass suppression is the See-Saw mechanism. It introduces new heavy particles to generate a small Majorana

---

Earth's atmosphere. Solar neutrinos constitute by far the largest flux of neutrinos from natural sources observed on Earth.

mass for the neutrinos by the coupling with the lepton and the Higgs doublets. In this process the Yukawa coupling is suppressed with respect to the massive neutrino couplings by a factor v/M, where v is the vev (vacuum expectation value) and M the mass of the heavy particle. This mechanism requires heavy particles in a range between 10^2 GeV and 10^{16} GeV. If M is very large, small masses of neutrino are generated of Yukawa coupling of the order of $\mathcal{O}(1)$ or higher. If M is smaller, the Yukawa coupling must be $\sim \mathcal{O}(10^{-6})$ or an alternative suppression mechanism is required, whereas for a mass $\ll M$ neutrinos would be predominantly Majorana particles.

This mechanism introduces a possible realization of the Weinberg operator in (1.42) suggesting an interaction mediated at tree level by new heavy field of mass M, in a mass range above the electroweak scale. Since heavy neutrino masses are proportional to M^{-1}, a small values are expected.

There are three ways of producing the Weinberg operator without the addition of extra gauge symmetries at high energies:

Type-I: introduces a *fermion singlet N*, that represents a RH sterile neutrino which couples to one lepton and one Higgs doublet [27];

Type-II: introduces a *scalar weak triplet* $\Delta = (\Delta^{++}, \Delta^+, \Delta^0)$, which couples to two lepton doublets and to two Higgs [28];

Type-III: introduces a *fermion weak triplet* $\Sigma = (\Sigma^+, \Sigma^0, \Sigma^-)$, whose neutral lepton component is considered as a RH neutrino [29].
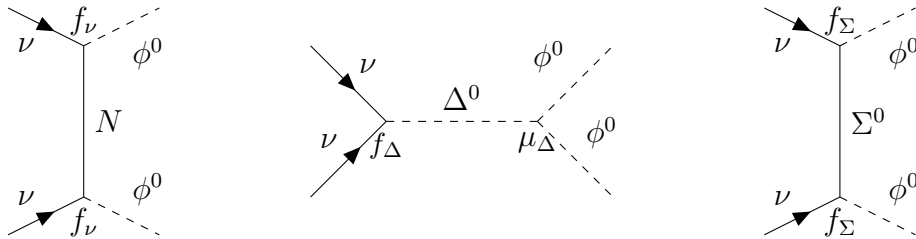
Figure 1.5: Generation of neutrino Majorana mass terms for the three versions of the SeeSaw mechanism.

In Figure 1.5 are shown the diagrams of the three SeeSaw models which give contributions to the Weinberg operator.

The main features of the SeeSaw mechanism are:

- Acquisition of the small neutrino masses in a natural way;

- It is a minimal theory, i.e. the only alteration with respect to the SM is the introduction of the new heavy lepton field;

- It has a finite number of parameters at high energies which can be determined with a finite number of observables at low energies (i.e. it is a renormalizable theory);

- It can be naturally embedded into a unified theory, such as the GUT or the "Left-Right Symmetric Model" (LRSM) [30];

- Considering the presence of a Majorana neutrino which violates the lepton number conservation, it would allow an explanation of the matter-antimatter asymmetry in the Universe. In this context, the lightest Majorana singlet fermion plays the role of DM candidate [36].

1.4.1 Type-I and Type-II Seesaw Mechanism

Type-I Seesaw

In the Type-I Seesaw we have the introduction of a gauge singlet chiral fermion N_R with zero hypercharge, which is a RH Majorana fermion. Adding this term to the Lagrangian and considering just one generation of leptons we have:

$$\mathcal{L} = i\bar{N}_R \slashed{\partial} N_R - y_N \ell_L \psi^* N_R - \frac{M}{2}\bar{N}_R^c N_R + h.c. \tag{1.43}$$

Using the Majorana spinor in (1.38) and performing the electroweak symmetry breaking (EWSB)[8] on this equation, we obtain a mass term of the type:

$$\mathcal{L}_{m_\nu} = \begin{pmatrix} \bar{\nu} & \bar{N}^c \end{pmatrix} \begin{pmatrix} 0 & m_D \\ m_D & M \end{pmatrix} \begin{pmatrix} \nu^c \\ N \end{pmatrix} \tag{1.44}$$

where $m_D = \frac{y_\nu v}{\sqrt{2}}$ is the Dirac mass. The eigenstates of (1.44) are:

$$m_{1,2} = \frac{M}{2} \mp \sqrt{\left(\frac{M}{2}\right)^2 + m_D^2} \tag{1.45}$$

So two masses are generated:

$$m_1 \simeq \frac{m_D^2}{M} \tag{1.46}$$

$$m_2 \simeq M \tag{1.47}$$

---

[8]The electroweak symmetry breaking is the process which gives mass to the weak boson, $W^\pm$ and Z^0.

a very tiny m_1 (1.46), inversely proportional to M and a heavy m_2 (1.47), directly proportional to M.

If $M \ll m_D$ the Dirac mass term is predominant for the neutrino; if $M \simeq m_D$ neutrino is a combination of Dirac and Majorana mass term. The last case provides an explanation of the lightness of the neutrino mass:

$$m_1 = m_\nu = -m_D^T \frac{1}{M} m_D = \frac{v^2}{2} y_\nu \frac{1}{M} y_\nu^T \tag{1.48}$$

One can estimate the order of magnitude of the mass M, considering a Yukawa coupling ~ 1, to be of the order of a typical GUT theory $\sim 10^{15}$ GeV.

Type-II Seesaw

Instead of a RH neutrinos, Type-II Seesaw introduces a scalar triplet. For simplicity we develop this case with a single scalar with hypercharge Y=1:

$$\vec{\Delta} = \begin{pmatrix} \Delta^1 \\ \Delta^2 \\ \Delta^3 \end{pmatrix} \tag{1.49}$$

Considering the dimensional representation of the $SU(2)$ generators (1.58)and using (1.13) to define the base of Δ, we can write the Lagrangian:

$$\mathcal{L} = \left(D_\mu \vec{\Delta}\right)^\dagger \left(D^\mu \vec{\Delta}\right) + \left[\widetilde{\bar{\psi}}_L y_\Delta \Delta \psi_L + \widetilde{\phi}^\dagger \mu_\Delta \Delta^\dagger \phi + h.c.\right] - V\left(\vec{\Delta}\right) \tag{1.50}$$

where $\widetilde{\psi}_L = i\sigma^2 \psi_L^c$, σ^2 is a Pauli matrix, y_Δ the Yukawa coupling and $V(\Delta)$ the scalar potential which includes all couplings in the scalar sector which are compatible with the symmetry. Another important parameter is μ_Δ, a dimensional parameter with mass dimension ~ 1. After the EWSB the mass matrix for the neutrinos is:

$$m_\nu = y_\Delta v^2 \frac{\mu_\Delta}{M_\Delta^2} \tag{1.51}$$

Similarly to Type-I mechanism, also in Type-II the mass M is assumed to be very large. Due to the simultaneous presence of Yukawa and μ_Δ couplings, the baryon number minus lepton number symmetry is broken. This symmetry can be restored, implying a massless neutrino, setting one of these couplings to zero.

With respect to Type-I, neutrino masses have now linear dependence with the Yukawa coupling (instead of quadratic) and they are created with two different mass scales M_Δ and μ_Δ. Given a Yukara coupling of ~ 1, a cut-off of:

$$\Lambda = \frac{M_\Delta^2}{\mu_\Delta} \sim 10^{13} \text{GeV} \tag{1.52}$$

is required, but without specific values for μ_Δ and M_Δ. We can estimate one of them fixing the other. For example if $\mu_\Delta \sim 10^{-6}$ we can lower M up to TeV scale.

1.4.2 Type-III Seesaw Mechanism

The last type of Seesaw mechanism introduces a fermionic triplet with zero hypercharge:

$$\vec{\Sigma} = \begin{pmatrix} \Sigma^1 \\ \Sigma^2 \\ \Sigma^3 \end{pmatrix} \tag{1.53}$$

The quantity used to couple this triplets to the doublets is:

$$\Sigma = \vec{\sigma}\vec{\Sigma} = \frac{1}{\sqrt{2}} \begin{pmatrix} \sqrt{2}\Sigma^3 & \Sigma^1 - i\Sigma^2 \\ \Sigma^1 + i\Sigma^2 & -\sqrt{2}\Sigma^3 \end{pmatrix} = \begin{pmatrix} N^0 & L^- \\ L^+ & -N^0 \end{pmatrix} \tag{1.54}$$

where $\vec{\sigma}$ is the vector of Pauli's matrices. So, the $\vec{\Sigma}$ fields[9] are defined as:

$$L_{\pm} = \frac{\Sigma_1 \mp i\Sigma_2}{\sqrt{2}} \quad , \quad N_0 = \Sigma_3 \tag{1.55}$$

The corresponding Lagrangian is:

$$\mathcal{L} = i\bar{\vec{\Sigma}}_R \slashed{D}\vec{\Sigma}_R - \frac{1}{2}\bar{\vec{\Sigma}}_R M \vec{\Sigma}_R^c - \bar{\vec{\Sigma}}_R y_\Sigma \left(\widetilde{\phi}^\dagger \vec{\sigma} \psi_L \right) + h.c. \tag{1.56}$$

where the covariant derivative is:

$$\slashed{D} = \slashed{\partial} + ig\slashed{\vec{W}}\vec{T} \tag{1.57}$$

and the three-dimensional generators $\vec{T}$ are:

$$T^1 = \begin{pmatrix} 0 & 0 & 0 \\ 0 & 0 & -i \\ 0 & i & 0 \end{pmatrix} \quad , \quad T^2 = \begin{pmatrix} 0 & 0 & i \\ 0 & 0 & 0 \\ -i & 0 & 0 \end{pmatrix} \quad , \quad T^3 = \begin{pmatrix} 0 & -i & 0 \\ i & 0 & 0 \\ 0 & 0 & 0 \end{pmatrix} \tag{1.58}$$

The triplet Majorana mass term is:

$$\mathcal{L}_M = \frac{1}{2}\bar{\vec{\Sigma}}_R M \vec{\Sigma}_R^c + h.c. \tag{1.59}$$

From (1.55) the physical particles as charged Dirac fermions L and neutral Majorana fermions can be derived:

$$L_L = L^+ \quad , \quad L_R = L^- \quad , \quad N_L = N^0 = N_R \tag{1.60}$$

---

[9]Theoretical calculations predict only a small mass splitting due to radiative corrections and the resulting possible new decays among the heavy leptons are highly suppressed.

After the EWSB, from (1.56) the neutrino and charged lepton mass term are given:

$$\mathcal{L}_\nu = -\frac{1}{2} \begin{pmatrix} \bar{\nu}_L & \bar{N}_L \end{pmatrix} \begin{pmatrix} 0 & \frac{v}{\sqrt{2}}y \\ \frac{v}{\sqrt{2}}y^T & M \end{pmatrix} \begin{pmatrix} \nu_R \\ N_R \end{pmatrix} + h.c. \tag{1.61}$$

$$\mathcal{L}_\ell = - \begin{pmatrix} \bar{\ell}_L & \bar{L}_L \end{pmatrix} \begin{pmatrix} \frac{v}{\sqrt{2}}y^\ell & vy \\ 0 & M \end{pmatrix} \begin{pmatrix} \ell_R \\ L_R \end{pmatrix} + h.c. \tag{1.62}$$

We finally have the expression of the generated masses:

$$m_1 = v y_\ell = m_\ell^D \tag{1.63}$$

$$m_2 = -v^2 y_\Sigma^T \left| M \right|^{-1} y_\Sigma = m_\nu = m_\ell^M \tag{1.64}$$

The form of the Majorana neutrino mass (1.64) is identical to that obtained for Type-I (1.46), which leads to the same considerations. However now, the eigenstate (1.63) is of the order of Dirac masses and a direct gauge interaction with the fermionic triplets of the Type-III Seesaw is allowed.

In conclusion, the Type-III Seesaw mechanism predicts the existence of a light triplet ($\sim$ TeV) which is the easiest to be discovered at colliders. The basis of SM and how it could be enlarged to explain neutrino mass generation via various types of Seesaw mechanisms was reviewed. In Chapter 3 the phenomenology of this process and how can be experimentally accessed by ATLAS will discuss. Instead, in the next paragraph a previous analysis with a different final states is presented.

1.4.3 Search at colliders: state of the art

ATLAS already performed a complementary search of Type-III Seesaw heavy leptons in the two-leptons two-jets final state (2l2j in the following) [31].

Heavy leptons can decay through different channels as reported in Table 1.4. In Figure 1.6, the heavy neutrino branching ratios (BR) as function of its mass are plotted for a range of masses reachable at the LHC energies. For instance, an

$N^0 \to \nu H$	$L^\pm \to \ell^\pm H$
$N^0 \to \nu Z$	$L^\pm \to \ell^\pm Z$
$N^0 \to W^\pm \ell^\mp$	$L^\pm \to W^\pm \nu$

Table 1.4: Type-III Seesaw heavy leptons decay modes.

hypothetical heavy neutrino with a mass of 1000 GeV has a $\sim$50% probability to decay in a ℓW pairs while the probability is $\sim$25% for the other two decay modes. For each mass value the production of ℓW pairs is dominant, which implies the
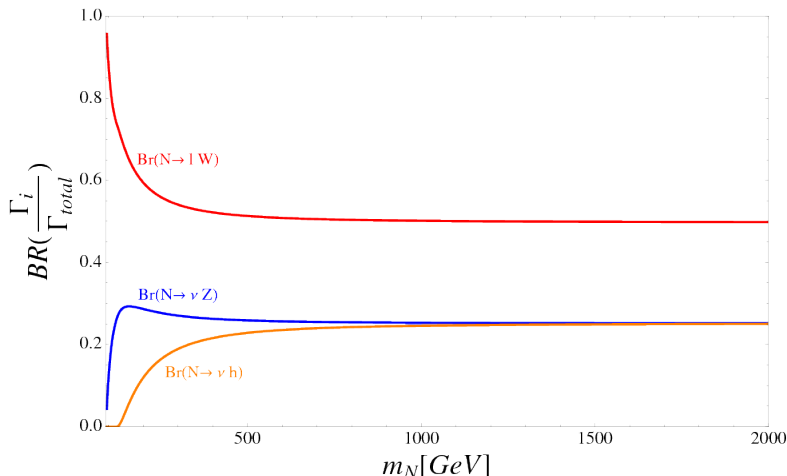
Figure 1.6: Branching ratios of the neutral component of the fermionic triplet considering the following lepton mixing matrix elements: $V_e=V_\tau=0$ and $V_\mu=0.063$. Because of the heavy leptons are assumed to be degenerate in mass, BRs into W, Z and H bosons are the same for the charged component [32].

largest cross-section for the process $pp \rightarrow W^* \rightarrow L^\pm N^0 \rightarrow W^\pm \nu W^\pm l^\mp$. The production cross-section does not depend on the mixing angles between Standard Model leptons and the new heavy lepton states. The considered search is performed only in final states in which both N^0 and $L^\pm$ decay into W boson. One of the W boson decays leptonically and the other decays hadronically.

The Feynman diagram considered in this analysis is reported in Figure 1.7. The signature of the final states contains two high-p_T leptons, two jets from the hadronically decay of the W boson and a large missing transverse energy due to the presence of two neutrinos. The two leptons can either have same charge or opposite charge, corresponding to the same sign (SS) and opposite sign (OS) pair respectively. Furthermore, they can also be of same flavour (ee or $\mu\mu$) or different flavour (eμ), while τ-leptons were not considered.

In Figure 1.8 the expected 95% CL exclusion plot with one and two standard deviation bands is shown. The expected lower mass limit of the Type-III Seesaw heavy leptons N^0 and $L^\pm$, corresponding at the intersection between the predicted cross section (red curve) and the expected limit (dashed line), is 550^{+68}_{-77} GeV. The observed limit is 560 GeV. A previous analysis of the ATLAS Collaboration using 8 TeV data with an integreted luminosity of 20.3 fb^{-1} excluded mass values below 335 GeV [33]. The CMS experiment performed similar analyses in the multilepton final states using 7 TeV data [34] and 13 TeV data [35]. In these searches, heavy leptons are assumed to be degenerate in mass.
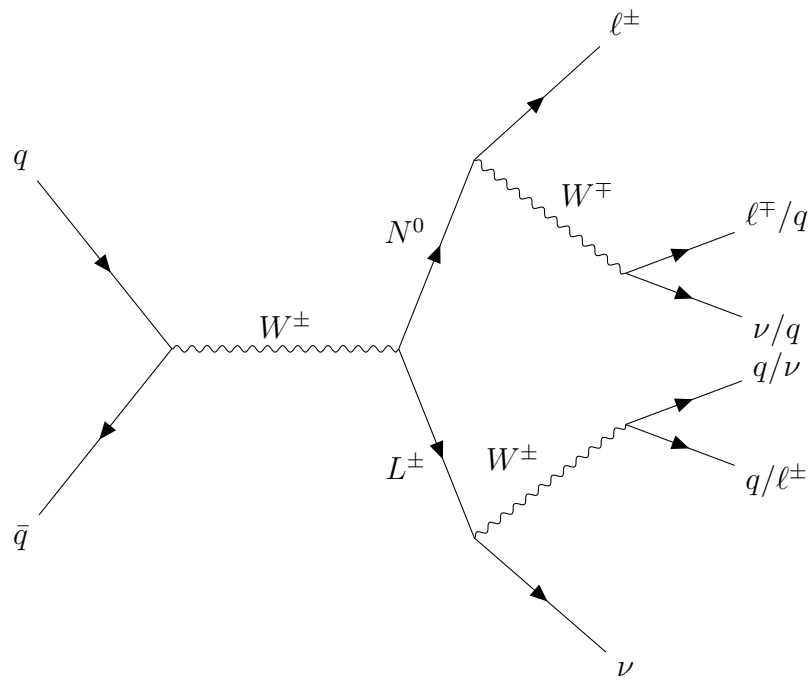
Figure 1.7: Feynman diagram for the dominant contribution to two-charged-leptons, two jets and two neutrinos final states in pair production of N^0 and $L^\pm$ in the Type-III SeeSaw mechanism.
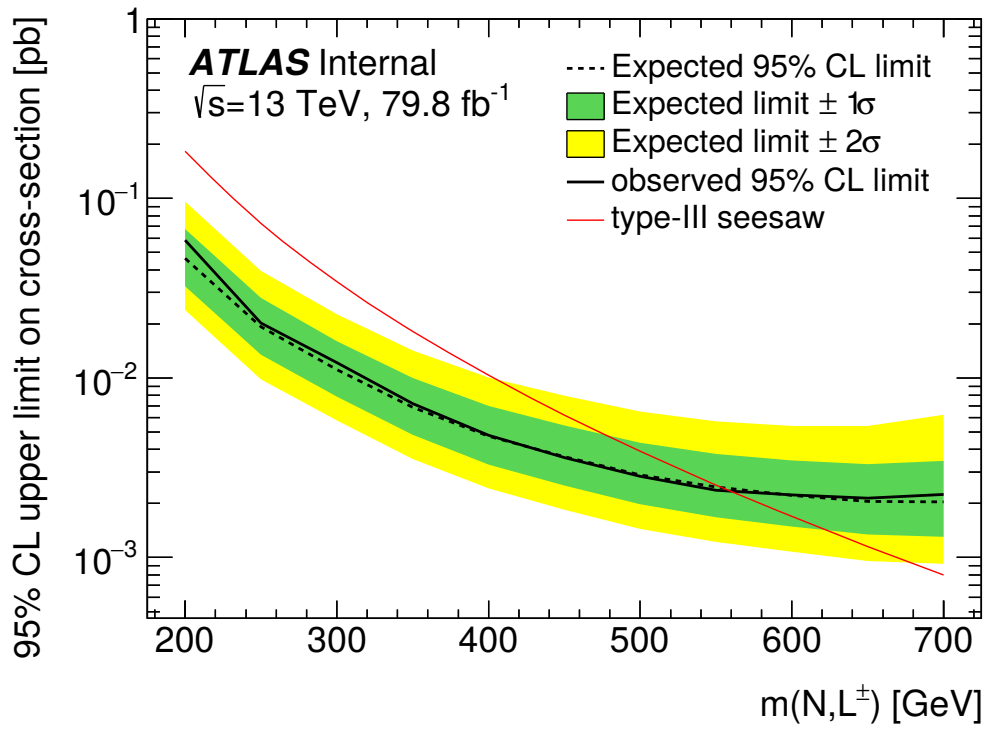
Figure 1.8: Expected 95 % CLs upper limit on cross-section for the type-III seesaw process with the corresponding one and two standard deviation bands.

CHAPTER 2

THE ATLAS EXPERIMENT AT LHC

Founded in 1954, CERN (from French: Conseil Europé en pour la Recherche Nuclé aire)[1] is the world's largest particle physics laboratory. It is placed in a north-west suburb of Geneva on the Franco-Swiss border and has 22 member states that cooperate to explore the fundamental laws of Nature. Built at CERN, the Large Hadron Collider (LHC) is the world's largest and most powerful particle accelerator. It is designed to explore unknown regions of physics and to discover new particles up to the TeV scale. The LHC is a ring where four particle detectors are located: ATLAS, CMS, ALICE, LHCb.

2.1   The LHC: Large Hadron Collider

The LHC is installed from 50 to 175 meters under the ground of Geneva suburb (see Figure 2.1), in the tunnel previously hosting the Large Electron-Positron Collider (LEP). It consists of a 27 kilometer ring of superconducting magnets with radio-frequency cavities to boost the energy of the particles. LHC is designed to accelerate protons or heavy ions (mainly lead ions) up to a center of mass energy of $\sqrt{s} = 14$ TeV and $\sqrt{s} = 2.76$ TeV per nucleon, respectively. After the upgrade shutdown in 2013, phase II started reaching a center of mass energy of $\sqrt{s} = 13$ TeV and an instantaneous luminosity of $2 \cdot 10^{34} \mathrm{cm}^{-2}\mathrm{s}^{-1}$. In Table 2.1 the main machine performances are reported. In pp collision mode, two protons circulate in opposite directions and collide every 25 ns, in correspondence of the four detectors. They travel into two separate ultra-high vacuum chambers at a pressure of 10^{-10} Torr. The LHC protons don't flow as a continuous beam but

---

[1]European Organization for Nuclear Research.
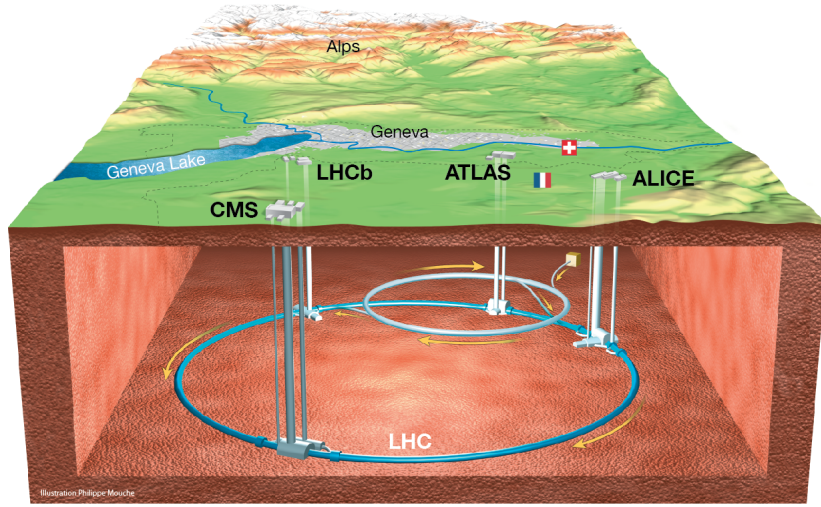
Figure 2.1: The LHC complex in the underground of Geneva.

Parameter	2015	2016	2017	Design
Beam Energy (TeV)	6.5	6.5	6.5	7
Bunch spacing (ns)	25	25	25	25
Max number of bunches	2244	2220	2736	2808
Protons per bunch	$1.1 \cdot 10^{11}$	$1.1 \cdot 10^{11}$	$1.25 \cdot 10^{11}$	$1.1 \cdot 10^{11}$
Peak Luminosity ($cm^{-2}s^{-1}$)	$5 \cdot 10^{33}$	$1.1 \cdot 10^{34}$	$1.4 \cdot 10^{34}$	$1 \cdot 10^{34}$
Average Pile-up ($<\mu>$)	~ 15	~ 25	~ 37	~ 20

Table 2.1: LHC performance during the operation of 2015-2017 compared to the machine design values [37].

they are packed into bunches[2]. In principle a maximum of 3564 bunches could fit the ring but in practice, not every bunch is filled, and there is an effective maximum of 2808 filled bunches. In order to keep the beams into circular trajectories, 1232 superconducting dipole magnets generate a magnetic field of 8.4 T at a current of

---

[2]Into a single bunch there are $\sim 10^{11}$ protons.
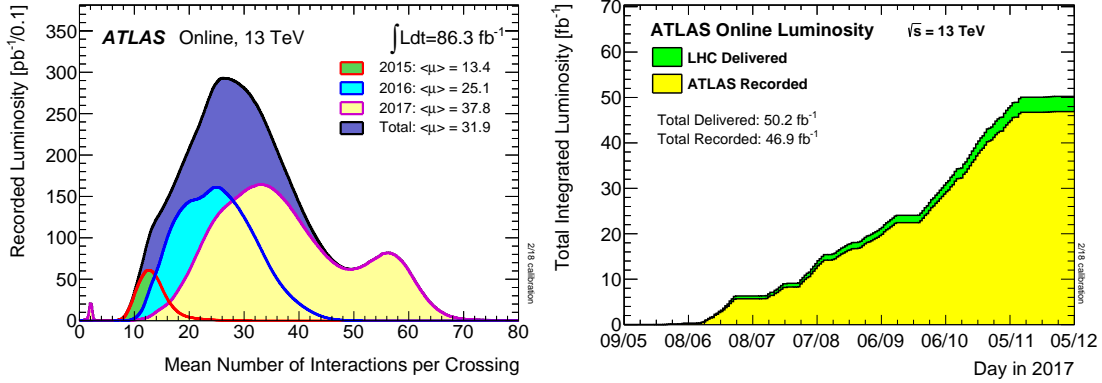
Figure 2.2: Left: Luminosity distribution as function of the mean number of interaction per crossing (pile-up) for the 2017 *pp* collision data recorded by ATLAS at $\sqrt{s}$=13 TeV. Right: Total integrated luminosity versus time delivered by LHC (green) and recorded by the ATLAS detector (yellow) in 2017.

11.85 kA and a temperature of 1.9 K. Instantaneous luminosity is one of the most important parameter of a collider's physics. It is independent from the physics process considered and it is defined as a function of the machine parameters. Considering two identical beams, with a Gaussian shape and perfectly overlapping at the Interaction Point (IP), the luminosity $\mathcal{L}$ is defined as

$$\mathcal{L} = f_r n_b \frac{N_1 N_2}{4\pi \sigma_x \sigma_y}, \tag{2.1}$$

σ_x and σ_y transverse profiles of the beams, N_1 and N_2 the number of protons per bunch, n_b number of bunches, f_r beam-revolution frequency.

Luminosity decreases every run because of the degradation of intensity in the circulating beam. This degradation is described by:

$$\mathcal{L} = \mathcal{L}_0 \cdot e^{-\frac{t}{\tau}} \tag{2.2}$$

where τ is a time constant which for LHC is ~ 15 h.

Two different type of luminosity are defined:

- *delivered* luminosity, that is the luminosity provided by the LHC;

- *recorded* luminosity, which is referred to the fraction of time during which both the detector and the data acquisition system were active.

In Figure 2.2 are reported, on the left, the luminosity collected by ATLAS during Run 2 (2015-2018) and, on the right, a comparison between the luminosity delivered by the LHC and the one recorded by the ATLAS detector. A data taking efficiency of $\sim 95\%$ in 2017.

2.2 Acceleration Chain

A complex acceleration chain is needed to produce and accelerate protons up to $\sqrt{s} = 13$ TeV (Figure 2.3).

The main proton source is a tank of Hydrogen gas which is used to create a plasma, separating protons from electrons. Protons are then ready to be injected
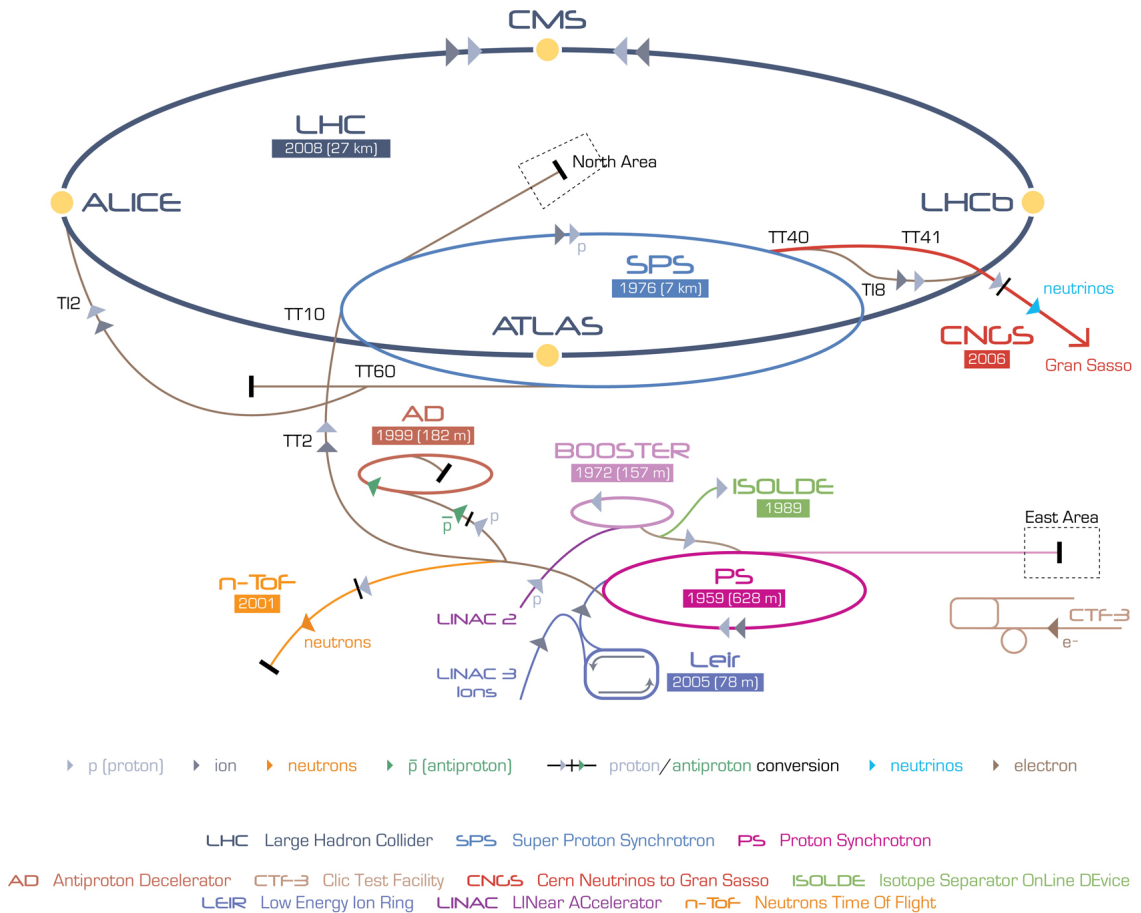
Figure 2.3: Scheme of the CERN accelerator complex.

in an acceleration chain consisting of:

Linac2: it is a linear accelerator to accelerate protons up to momenta of 50 MeV. A system of quadrupole magnets is used to focus the beam. Particles (protons or heavy ions) are then transferred to the Proton Synchrotron Booster (PSB);

PSB: it is composed of 4 superimposed rings to accelerate protons up to 1.4 GeV. After the beams have been focused, through a magnet deflector, they are sent into a single line for injection into Proton Synchrotron (PS);

PS: it is the oldest circular accelerator of the LHC with a circumference of 628 meters. A system of electromagnets and dipole magnets allow to have a circular trajectory. PS produces a proton bunch every 25 ns with 25 GeV of energy for each proton. The beam is then sent to the last injector of the accelerator chain, the Super Proton Synchrotron (SPS);

SPS: it is a circular accelerator with a circumference of 7 km with a system of magnets similar to the PS. The SPS accelerates protons up to an energy of 450 GeV.

LHC: at the end of the acceleration chain, beams are transferred to the LHC ring, one circulating clockwise and the other anti-clockwise. The accelerator uses two types of superconducting magnets cooled with a liquid helium system at -273.3 °C: 1232 dipole magnets and 392 quadrupole magnets. It takes around 20 minutes for each beam to reach its final energy of 6.5 TeV.

When proton bunches reach the energy of 6.5 TeV, the two beams are deviated to cross with each other in four interaction points in correspondence of the four experiments. They are:

ATLAS: A Toroidal LHC ApparatuS. It is a multi-purpose detector designed to work at high luminosity ($\mathcal{L} = 10^{34} \text{cm}^{-2}\text{s}^{-1}$). Its aim is the discovery of new physics' signatures and to perform precise Standard Model measurements;

CMS: Compact Muon Solenoid. It is a multi-purpose experiment working at high luminosity. It has the same physics goals of ATLAS but by means of different technologies;

LHCb: it investigates the flavour physics of B mesons and CP violation. LHCb works at lower values of luminosity ($\mathcal{L} = 10^{32} \text{cm}^{-2}\text{s}^{-1}$);

ALICE: A Large Ion Collider Experiment. It is designed for the study of quark-gluon plasma state produced in heavy ion collisions (mainly ions). Using nucleus-nucleus collisions, it can work with a luminosity $\mathcal{L} = 10^{27} \text{cm}^{-2}\text{s}^{-1}$.

2.3 Physics Requirements

The complexity of the data analysis of LHC events can be realized looking at Table 2.1, which shows a number of interaction per bunch-crossing (*pile-up*) of ~ 37, every 25 ns. These collisions between protons involve multiple inelastic scatterings of *partons* (the hadrons' constituents) that imply a non-null probability of multiple interactions in a single collision. These events are usually called *underlying events*,

which are due to *Initial State Radiation* and to *Final State Radiation*, i.e. gluon radiations in the initial and final states. To track and identify all the produced particles in a so dense environment, high granularity and multiple detectors are required. Detectors must satisfy:

- fast response, radiation-hard electronics and sensor elements. Due to the high particle fluxes and the influence of overlapping events, a high detector granularity is needed;

- good azimuthal angle (ϕ) coverage and large acceptance in pseudorapidity (η) (as defined in Section 2.4);

- good resolution in the electromagnetic calorimeter to identify electrons and photons and to reconstruct their energy deposits. The hadronic calorimeter needs a full-coverage for accurate jet and missing transverse energy measurements;

- good tracking capabilities by the Inner Detector for charged-particle momentum resolution and large reconstruction efficiency;

- good resolution on the secondary vertex location to identify τ leptons and b-jets;

- good muon momentum resolution and identification. In addition, a determination without ambiguities of the charge in the high-p_T region is needed;

- highly efficient trigger system with a sufficient background rejection.

2.4   The ATLAS Detector

Shown in Figure 2.4, the ATLAS detector is a multi-purpose particle detector placed ∼100 meters underground at the Point-1 site along the LHC tunnel. ATLAS has a cylindrical symmetry and it is composed of many different sub-detectors to reconstruct particles from pp collisions. Starting from the IP there are: the Inner Detector, the electromagnetic and hadronic calorimeters and the muon spectrometer. A magnetic system is also included to deflect charged-particle trajectories and to allow their momenta reconstruction.

A detailed description of each subdetector and their performances are reported in Table 2.2. ATLAS uses a cylindrical coordinate system with the IP in the origin of the axis (see Figure 2.5). The z-axis is defined along the beam line, the x-axis points from the IP to the centre of the LHC ring, and the y-axis points upward. The x-y plane is the *transverse plane*, perpendicular to the beam line, where the
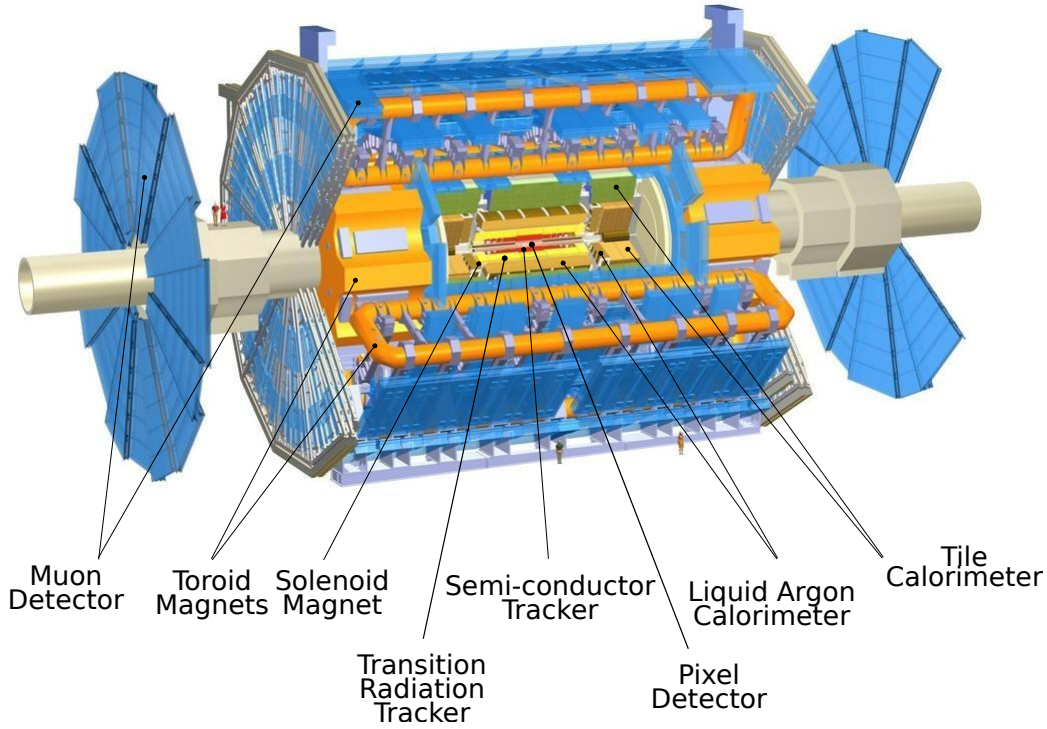
Figure 2.4: Sketch view of the ATLAS detector showing its various components. The ATLAS detector is 46 meters long, 25 metres radius, it weighs 7000 tons and consists of 100 million sensors.

Detector Component	Resolution	η coverage	
		Measurement	Trigger
Tracking	$\sigma_{p_T}/p_T = 0.05\% p_T \oplus 1\%$	± 2.5	
EM Calorimetry	$\sigma_E/E = 10\%/\sqrt{E} \oplus 0.7\%$	± 3.2	± 2.5
Hadronic Calorimeter			
barrel (Tile) and end-caps (LAr)	$\sigma_E/E = 50\%/\sqrt{E} \oplus 3\%$	± 3.2	± 3.2
forward (LAr)	$\sigma_E/E = 100\%/\sqrt{E} \oplus 10\%$	$3.2<|\eta|<4.9$	$3.2<|\eta|<4.9$
Muon Spectometer	$\sigma_{p_T}/p_T = 10\%$ at p_T=1 TeV	± 2.7	± 2.4

Table 2.2: General performance of the ATLAS detector. Units for p_T and energy are in GeV.

transverse momenta (p_T) and the missing transverse energy (E_T^{miss}) are conserved. The detector half at positive z-values is referred to as the "A-side" while the other one as "C-side". The azimuth angle ϕ is measured in the transverse plane to the beam line. The polar angle θ is measured with respect to the positive side of the z-axis. In pp collisions the longitudinal flow of the hard scatterers is unknown, hence the transverse components of momenta are used, being $\sum p_T \simeq 0$ for the
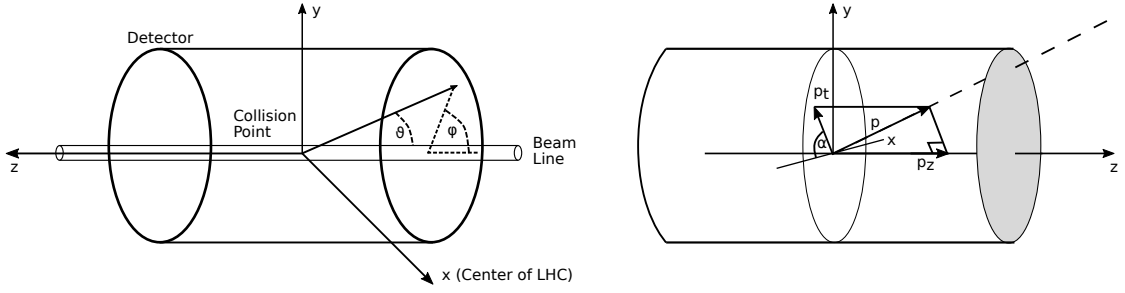
Figure 2.5: Left: ATLAS detector coordinate system. Right: Coordinate system in the tranverse momentum plane.

whole event. The rapidity y, a Lorentz-invariant variable, is defined as:

$$y = \frac{1}{2} \ln \left(\frac{E + p_z}{E - p_z} \right) \tag{2.3}$$

where E and p_z are the energy and the z-axis momentum component of the particle respectively. For relativistic particles the pseudorapidity, defined as:

$$\eta = -\ln \left(\tan \left(\frac{\theta}{2} \right) \right) \tag{2.4}$$

is also an invariant quantity asymptotically converging to the rapidity. In order to measure the isolation of an object, a cone around the reconstructed object direction is defined

$$\Delta R = \sqrt{(\Delta \eta)^2 + (\Delta \phi)^2} \tag{2.5}$$

where $\Delta \eta$ and $\Delta \phi$ are the differences of pseudorapidity and of azimuth angles between two objects.

2.4.1 The ATLAS Magnetic System

The curvature radius ρ of a particle with a charge q and a momentum p travelling in a magnetic field B is derived using the Lorentz force:

$$\rho = \frac{|\vec{p}|}{q \left| \vec{B} \right|}. \tag{2.6}$$

ATLAS has three superconducting magnetic field systems (see Figure 2.6) cooled at liquid helium temperature (4.8 K). In the inner part there is the **Central Solenoid (CS)**, a superconducting solenoid providing a 2 T magnetic field for the inner tracker. It has a radius of 1.2 m, lenght of 5.3 m and it is parallel to the beam axis.

34
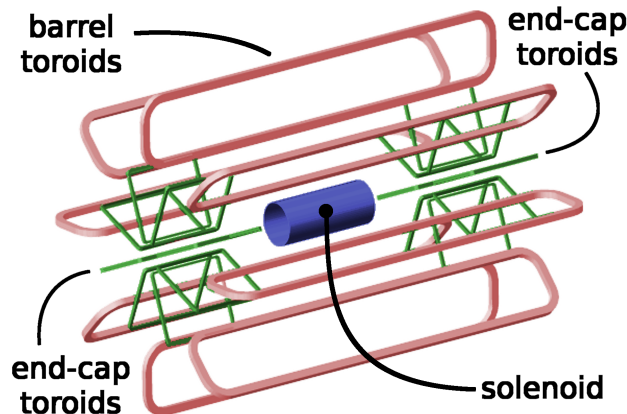
Figure 2.6: Magnetic system of the ATLAS detector.

The **Barrel Toroid (BT)** is formed by 8 rectangular coils in a cylindrical configuration. It is 25 m long, with an inner core of 9.4 m and an outer diameter of 20.1 m. It provides a maximum magnetic field of 4 T to measure particle bendings in the region of $|\eta| \leq 1$.

The **End-Cap Toroid (ECT)** is composed of 8 rectangular coils in a single cylindrical vessel, for a total length of 5 m. Is has an inner core of 1.64 m and an outer diameter of 10.7 m. The ECT magnets bend the particle trajectories in the region $1.4 < |\eta| < 2.7$ with a maximum magnetic filed of 4 T. The configuration of ECT is chosen to obtain a magnetic field orthogonal to the beam axis and close to the magnetic field lines produced by the BT.

2.4.2 Inner Detector

The first sub-detector that a particle crosses from the IP is the **Inner Detector (ID)**. It is placed close to the IP inside the Central Solenoid. Its aim is to reconstruct the charged particles tracks and their production vertexes to allow the identification of long lived particles and to distinguish electrons from photons or charged hadrons. The ID has a cylindrical symmetry, an outer radius of 105 cm and covers the region up to $|\eta| < 2.5$. It can be divided into a barrel section and two identical end-caps, perpendicular to the z-axis. High precision measurements, require a high granularity, due to the large track density produced by pp collisions. The quantities used in the tracking system are the transverse impact parameter d_0, as the distance of the closest approach to the beam axis, and the longitudinal impact parameter z_0. Their resolution are

$$\sigma(d_0) = 12 \oplus \frac{88}{p_T\sqrt{\sin(\theta)}}\ \mu\mathrm{m}^{-1} \tag{2.7}$$
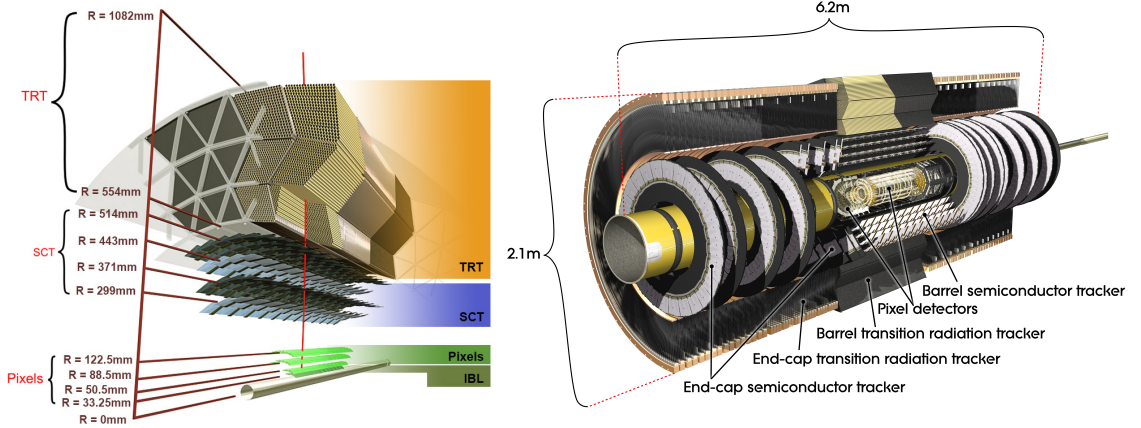
Figure 2.7: Left: Schematic layout of the Inner Detector including the new Insertable B-Layer. The distances to the interaction point are also shown. Right: Cut-away view of the ATLAS inner detector.

$$\sigma(z_0) = 95 \oplus \frac{160}{p_T \sqrt{\sin^3(\theta)}} \ \mu\text{m}^{-1} \tag{2.8}$$

where the track p_T is in units of GeV/c.

The **Pixel Detector (PD)** is the inner part of the ID. It is composed by 1744 pixel modules with 46080 readout channels per module organized into three barrel layers for a total of 80 million pixels, $50 \times 400 \ \mu\text{m}^2$ each. Pixel modules in the barrel region are tilted by $20°$ with respect to the cylinder's tangent to counterbalance the effect of the Lorentz angle. To maximize the angular coverage there are also five rings on each side with an inner radius of 11 cm and an outer radius of 30 cm.

The **Semi Conductor Tracker (SCT)** is designed to provide precision measurements of the impact parameter, momentum and vertex position in the intermediate radial range. The SCT barrel is composed of four layers of microstrip modules placed 30 cm to 52 cm from the IP. Each silicon detector-modules has 768 readout strips with a pitch of 80 μm, i.e. $6.36 \times 6.40 \text{ cm}^2$. To reach a coverage of $|\eta| < 2.5$, on both sides of the barrel layers 9 SCT disks are placed. In the end-cap region, strips are placed rotated of 40 mrad with respect to the front side. The spatial resolution of the SCT is 17 μm along the r - ϕ direction and 580 μm in the z direction.

The **Transition Radiation Tracker (TRT)** is the outer part of the Inner Detector. It is a combination of a straw tubes tracker and a Transition Radiation

36

Detector. The tubes are placed in 36 layers, with a diameter of 4 mm each one. TRT straws are filled with a Xenon or Argon gas mixture, which ionizes when a charged particle cross it. The low energy signal induced by the ionization is collected by a gold-plated 30 μm thin tungsten wire, placed in the middle of the tubes. Between each layer, polypropylene fibers cause Transition Radiation (TR) emission (X-Ray) when crossed by a particle. This TR is absorbed by the Xenon in the gas mixture that produces an high amplitude signal in the TRT electronic which can be distinguished from ionization signal by the voltage intensity. The spatial resolution of the TRT is 130 μm. TRT is fundamental to the identification of $e^{\pm}$, and it is also used to discriminate between light and heavy particles (as electrons from pions). In the barrel region there are about 50000 straws, 144 cm long, parallel to the beam axis with a coverage up to $|\eta| < 0.7$. In the end-cap region, about 320000 straws, 37 cm long, are arranged radially, covering a rapidity interval $0.7 < \eta < 2.5$.

2.4.3 The ATLAS Calorimeters

Calorimeters used in ATLAS are designed to trigger and to provide precision energy and positions measurements of electrons, photons, jets, neutrons and E_T^{miss}. This type of apparata measures the kinetic energy of the incoming particle, which initiates a particle shower inside it. For a complete measure of the energy, a total containment of the particle shower is required. The ATLAS Calorimetric System (see Figure 2.8) consists of two sampling calorimeters, the **Electromagnetic Calorimeter** (**EM**) and the Hadronic Calorimeter (**HCAL**).

A sampling calorimeter has a *passive medium*, composed by a material with high interaction cross-section (depending on the type of particle to detect), and an *active medium* to provide the detectable signal.

Electromagnetic Calorimeter

The Electromagnetic Calorimeter is composed of a sequence of lead absorber plates, as passive medium, and liquid Argon gaps as active material. Lead plates were chosen due to their large electromagnetic cross-section: high energy electrons and photons mainly interact via bremsstrahlung or pair production, causing an electromagnetic shower. The Argon is thus ionized and a signal related to the energy of the incident particle is acquired by a read-out system.

The calorimeter is divided into a central barrel, with a cylindrical coverage in pseudorapidity of $|\eta| <$1.475, and two end-cap elements with a coverage range of 1.375$< |\eta| <$3.2, perpendicular to the beam axis. The first component is composed of two half-barrel parts separated by a gap of 6 mm at $z = 0$; the second is divided
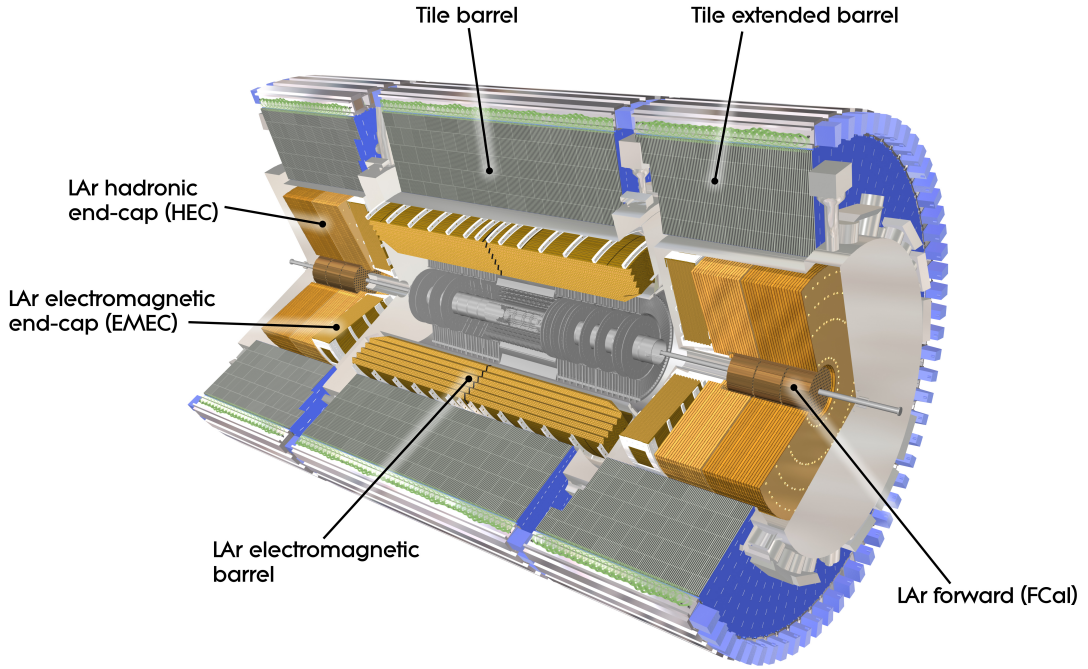
Figure 2.8: A 3-dimensional image of the electromagnetic and hadronic ATLAS calorimeters.

into two coaxial wheels, the outer with a coverage of 1.375< $|\eta|$ <2.5, the inner one with 2.5< $|\eta|$ <3.2.

Similar to an accordion geometry (see Figure 2.9), a complete ϕ symmetry without azimuthal cracks is allowed. EM calorimeter has a total thickness of more than 22 radiation lengths[3] (X_0) in the barrel and more than 24 X_0 in the end-caps. To enhance the precision in the central region the EM calorimeter is segmented into three longitudinal sections in the $|\eta| < 2.5$ region. The first compartment is realized with narrow cells ($\sim$5 mm in η) to provide high precision angular measurements and to improve particle identification. The second compartment measures the released energy using cells of $\Delta\eta \cdot \Delta\phi = 0.025\times0.025$. The last compartment, made of $\Delta\eta \cdot \Delta\phi = 0.025\times0.05$ square towers, measures the energy of particles that are not contained in the central compartment. Its thickness can vary between 2 X_0 and 16 X_0.

The region within $1.375 < |\eta| < 1.52$, between the barrel and the end-caps, contains inactive material providing necessary services to the ID. Then a reduced

---

[3]It is the mean distance over which the electron energy is reduced of a $1/e$ factor only by the bremsstrahlung process.
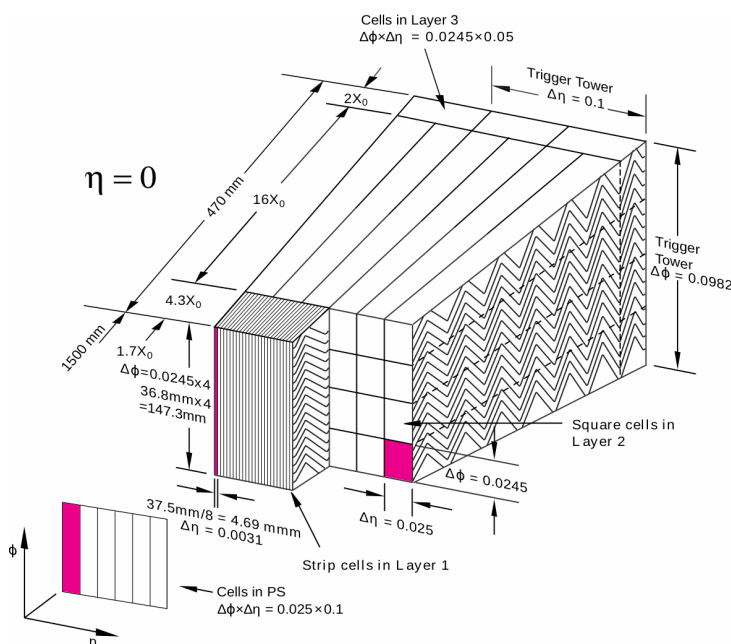
Figure 2.9: Sketch of a barrel module with the accordion geometry. The granularity in η and ϕ cells of each of the three layers and of the trigger towers is also shown.

performance in the energy measurements is present in this region.

EM calorimeter can identify photons and electrons in a range within 5 GeV and 5 TeV. Its energy resolution was calibrated with electron beams in a energy range of 10 GeV and 245 GeV. The fit result gave a resolution of:

$$\frac{\sigma_E}{E} = \frac{9.4\%\sqrt{\text{GeV}}}{\sqrt{E[\text{GeV}]}} \oplus 0.1\% \tag{2.9}$$

in agreement with dedicated Monte Carlo (MC) simulations.

The Hadronic Calorimeter

The Hadronic Calorimeter is designed to detect jets from hadronic showers and to measure their kinetic energy. Furthermore, it is used to measure the E_T^{miss} and to avoid strong-interacting particles to reach the muon system. HCAL covers a region within $|\eta| < 4.9$ using different techniques to reconstruct jet energy. For a good resolution of high energy jets at least $\sim 10\ \lambda$ thick is required, where the *interaction length*[4] $\lambda \simeq 35\ \text{A}^{1/3}\ \text{g cm}^{-2}$.

---

[4]Nuclear interaction length is the mean path length required to reduce the numbers of relativistic charged particles by the factor $1/e$ as they pass through matter.

HCAL is divided into an *Hadronic Tile Calorimeter* (HTC), two *Hadronic End-Caps Calorimeter* (HEC) and a *Forward Calorimeter* (FCAL) (see Figure 2.8).

The **HTC** is a sampling calorimeter with iron as passive material and plastic scintillators as active material. It covers a region of $|\eta| < 1.7$. The signal produced by scintillators when the hadrons interact with iron is proportional to the secondary particles produced in the interactions and then to the particle energy deposit. A calibration with pions in test beams gave a resolution of:

$$\frac{\sigma_E}{E_\pi} = \frac{(52.7 \pm 0.9)\,\%\sqrt{\text{GeV}}}{\sqrt{E[\text{GeV}]}} \oplus (5.7 \pm 0.2)\,\% \tag{2.10}$$

in agreement with MC simulations.

The **HEC** uses LAr as active medium, covering a range $1.5 < |\eta| < 3.2$. It consists of two independent wheels per end-cap, located in the same cryostat of the electromagnetic calorimeter. The resolution was measured in beam tests with electrons, pions and muons which gave:

$$\frac{\sigma_E}{E_e} = \frac{(21.4 \pm 0.1)\,\%\sqrt{\text{GeV}}}{\sqrt{E[\text{GeV}]}} \qquad \rightarrow \quad \text{Electrons} \tag{2.11}$$

$$\frac{\sigma_E}{E_\pi} = \frac{(70.6 \pm 1.5)\,\%\sqrt{\text{GeV}}}{\sqrt{E[\text{GeV}]}} \oplus (5.8 \pm 0.2)\,\% \qquad \rightarrow \quad \text{Pions} \tag{2.12}$$

in agreement with MC simulation.

The **FCAL** is situated very close to the beam pipe, covering the region $|\eta| < 4.9$. It is made of LAr, iron and tungsten. The FCAL allows the detection of hadronic jets at angles less than 1 degree. Also the FCAL was calibrated with electrons and pions, giving a resolution of:

$$\frac{\sigma_E}{E_e} = \frac{(28.5 \pm 0.1)\,\%\sqrt{\text{GeV}}}{\sqrt{E[\text{GeV}]}} \oplus (3.5 \pm 0.1)\,\% \qquad \rightarrow \quad \text{Electrons} \tag{2.13}$$

$$\frac{\sigma_E}{E_\pi} = \frac{(94.2 \pm 1.6)\,\%\sqrt{\text{GeV}}}{\sqrt{E[\text{GeV}]}} \oplus (7.5 \pm 0.4)\,\% \qquad \rightarrow \quad \text{Pions.} \tag{2.14}$$

2.4.4 The Muon Spectrometer

Due to the large mass with respect to electrons, the muon energy loss during its travel up to the HCAL is of the order of a few MeV/mm, surviving the previous layers. This is the reason why the **Muon Spectrometer** (**MS**) is located in the
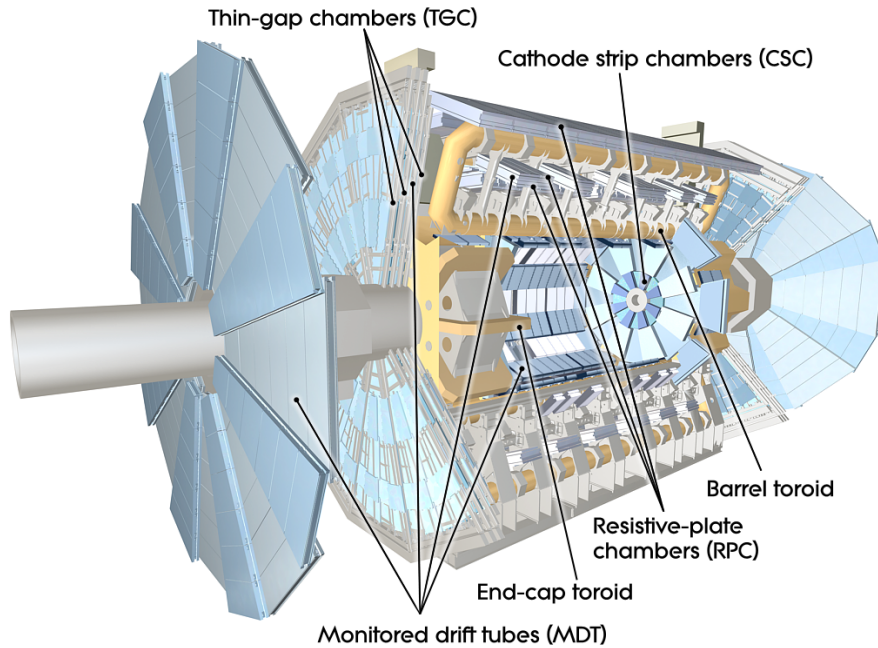
Figure 2.10: Digital layout of the muon spectrometer.

outer part of the detector (see Figure 2.10). Good muon reconstruction efficiencies are obtained combining ID and MS informations. The toroidal magnets arranged outside the calorimeter provide a magnetic field perpendicular to the beam line. Due to the muon trajectory deflection in the field, an independent measurement of its momentum with respect to the one given by the ID is allowed. For muons with p_T lower than 30 GeV, MS gives a less accurate momentum resolution due to the energy loss in the previous layers of the detector.

The MS has an outer diameter of 22 meters and it is composed of *trigger chambers* and *precision chambers*.

Trigger chambers

The trigger chambers allow fast muon detection exploiting both **Resistive Plate Chambers** (**RPC**) and **Thin Gap Chambers** (**TGC**) technologies.

The **RPC**s are gaseous parallel electrode-plate detectors, with a gas mixture of 97% tetrafluoroethane ($C_2H_2F_4$) and 3% isobutane (C_4H_{10}). They provide a spatial resolution of 1 cm in two coordinates and a time resolution of 1 ns. The RPCs have three layers of detection, each one reads out by two orthogonal series of pick-up strips to give information on both η and ϕ coordinates.

Working in an avalanche regime with an electric field of 4.9 kV/mm, when

muons traverse the chambers produce primary ionization electrons that are multiplied into avalanches.

The **TGC** are placed into the end-cap region of trigger chamber. They are filled with a quenching gas mixture of 55% CO_2 and 45% n-pentane C_5H_{12}. Due to the smaller anode-cathode spacing with respect to the anode-anode spacing, a drift time less than 20 ns is allowed. To reach a good performance in an high particle flux and a time resolution of 4 ns, the chamber works in saturation regime. The spatial resolution of TGC is 4 mm in the radial direction and 5 mm in the ϕ coordinate.

Precision Chambers

The aim of precision chambers is to reconstruct the trajectory of the muons. They are composed by **Monitored Drift Tubes (MDT)** and **Cathod Strip Chambers (CSC)**.

The **MDT** are drift chambers made of two multi-layer aluminium drift tubes, with diameter of 30 mm filled with Ar/CO_2 at 3 bar. They measures the z coordinate up to $|\eta| < 2$ in the barrel and end-cap region respectively.

The full particle trajectory is reconstructed by the drift time in a single tube with a spatial resolution of 80 μm.

The **CSC** are multi-wire proportional chambers with segmented cathode readout. They provide measurements of muon momenta in the region $2 < |\eta| < 2.7$. The cathodes are segmented to provide excellent spatial resolution and high counting rate capability. One is perpendicular to the wires providing the precision coordinate, the other one is parallel to the wire to give information on the transverse coordinate. The anode-cathode spacing is equal to the anode-wire pitch by design (2.5 mm). The spatial resolution is of 60 μm in the ϕ direction and of the order of 1 cm in η. The time resolution is of 7 ns.

2.4.5 The ATLAS Trigger and Data Acquisition System

With the increasing of the LHC performance during Run 2, about one billion of events per second have to be collected and analyzed. Then, a filter to manage these data is required. It is obtained with a trigger and data acquisition system (TDAQ), an online events selection rejecting all of the non interesting events and reducing the information rate from about 40 MHz to about 100 Hz. The TDAQ limitations are due to the high peak luminosity and pile-up which increase the probability of fake events selection.

ATLAS trigger system is divided into an hardware **Level 1 (L1)** system and a software-based **High-Level Trigger (HLT)** system (see Figure 2.11).
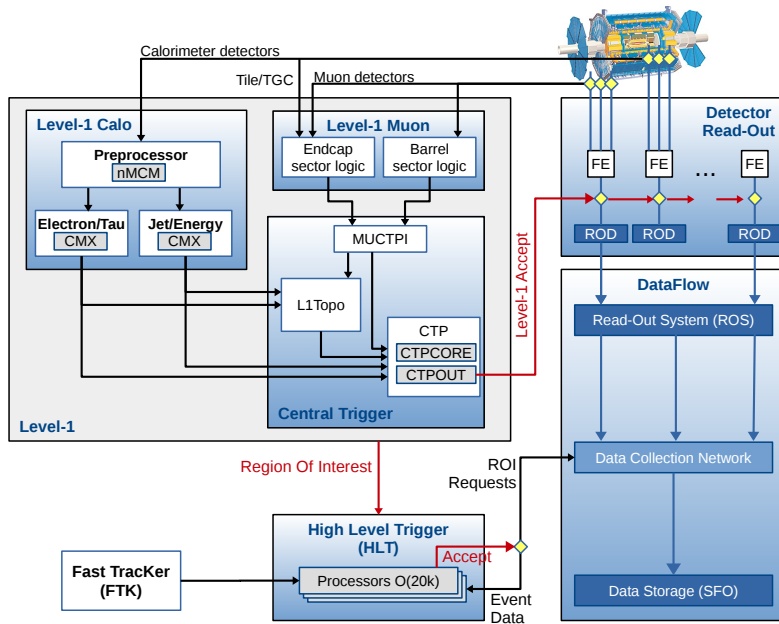
Figure 2.11: Scheme of the ATLAS trigger and data acquisition (TDAQ) system in Run-2.

Level 1

The **L1** trigger searches for high transverse-momentum muons, electrons, photons, jets and τ leptons, as well as large missing energy and total transverse energy. It collects information from both the calorimeter (L1 Calo) and the muon detector (L1 Muon). L1 Muon identifies high transverse-momentum muons using trigger chambers of the MS. L1 Calo gives informations from all of the calorimeters about cluster measuring energy, E_T^{miss} and τ-like objects. In Run 2 a new topological processor is introduced, the **L1 Topo**. It calculates event topological variables used to generate triggers and combines information from L1 Calo and L1 Muon systems. The Central Trigger Processor handles the results of previous levels producing the L1 trigger decision. At the end of the chain, the event-rate is reduced from 40 MHz to 100 kHz.

High Level Trigger

Downstream the L1 system, the High Level Trigger (HLT) system refines the decision of the previous level. On the right of the Figure 2.11 the sub-system of HLT is shown. It is composed by:

- the Region of Interest Builder (RoIB) reads and combines L1 triggers informations to send them to HLT Supervisor;

- the HLT Supervisor (HLTSV) organizes events to HLT cluster and clears the Readout system buffers;

- the Data Collection Manager (DCM) schedules the input/output data to the HLT nodes;

- the HLT Process (HLTPU) wraps the ATLAS reconstruction software, Athena, and interfaces it to the DAQ system.

Triggered events are then saved on a physical disk and sent to a permanent storage by the Data Loggers. To reduce the data size a *prescale factor* can be applied to each trigger tools. In Figure 2.12 some examples of the trigger efficiency are reported.
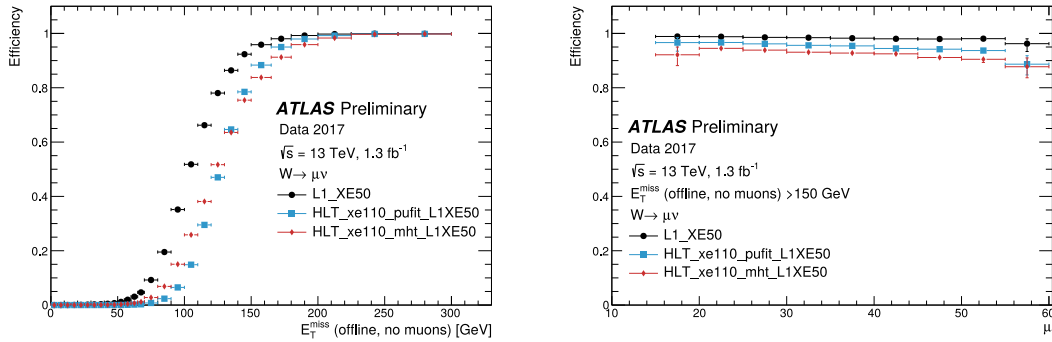
Figure 2.12: Left: The combined L1 and HLT efficiency of the missing transverse energy triggers `HLT_xe110_mht_L1XE50` and `HLT_xe110_pufit_L1XE50` as well as the efficiency of the corresponding L1 trigger (L1XE50) are shown as a function of the reconstructed E_T^{miss} (modified to count muons as invisible). Right: Previous but as a function of the mean number of simultaneous interactions in a given proton-proton bunch crossing (pile-up).

2.4.6 The Forward Detectors

To detect particles with high pseudorapidity, missing the central detectors, forward detectors are needed. The ATLAS Forward Detectors (Figure 2.13) are:

- **Minimum Bias Trigger Scintillator** (**MBTS**) is designed to detect low momentum particles and to select events from low luminosity collisions. It is situated at 356cm from the IP and covers a region $1.9 < |\eta|\, \eta < 3.8$;

- **Beam Conditions Monitor (BCM)** is placed at a distance of 1.84 meters from the IP, covers the region $3.9 < |\eta|\,\eta < 4.1$. It consists in diamond sensors revealing the passage of charged particles. The BCM gives a measurement of the instantaneous relative luminosity detecting signals of beam instability, measuring interaction rate and discriminating signals from background;

- **Luminosity measurements Using Cherenkov Integrating Detector (LUCID)** is a Cherenkov detector designed to measure the relative luminosity measurements in the region $5.6 < |\eta|\,\eta < 5.9$. It is placed at 17 meters from IP. It is the detector that gives the ATLAS official luminosity measurement;

- **Zero Degree Calorimeter (ZDC)** is a quartz-tungsten calorimeter designed for relative luminosity measurements during heavy ion runs. It measures forward cross-section detecting neutral particles (mainly photons and neutrons) very close to the beam axis. It is placed at 140 meters from IP and covers the region $|\eta| > 8.3$;

- **Absolute Luminosity for ATLAS (ALFA)** measures the proton cross section in elastic scattering collisions in the coulomb nuclear interference region, used to evaluate the absolute luminosity of ATLAS. It covers the region $10.6 < |\eta|\,\eta < 13.5$, to detect small-angle scattered protons. ALFA is located at 240 meters from IP;

- **ATLAS Forward Proton (AFP)** it was installed for Run 2 data taking, to improve measurements of protons positions and directions. It is a two station spectrometer placed at ± 220 meters and ± 420 meters from IP.
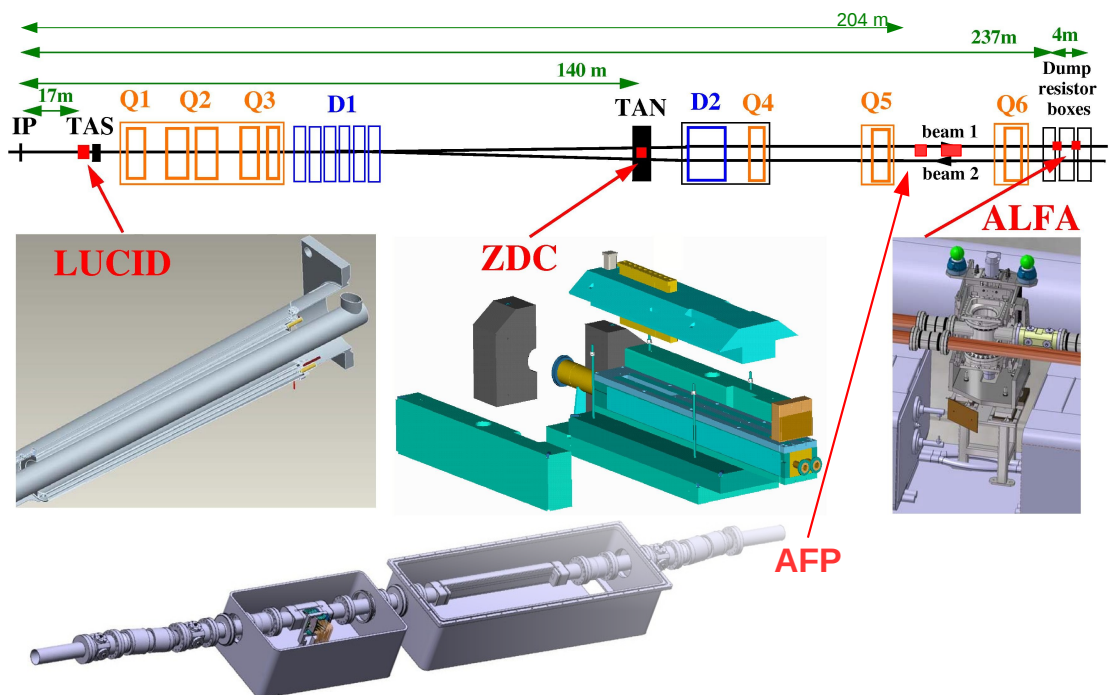
Figure 2.13: ATLAS Forward Detectors and their relative positions with respect to the IP.

CHAPTER 3

OBJECTS RECONSTRUCTION AND EVENTS SELECTION

The first step of the ATLAS analysis is the *objects reconstruction*. It consists in the reconstruction and identification of the observed particles produced in *pp* collisions and travelling inside the ATLAS detector. These objects are typically: *electrons*, *muons*, *tau leptons* and *jets*.

The reconstruction has the aim to provide an high efficiency also rejecting background events.

Lepton selection efficiency depends on all the steps subsequently described. Then, the total efficiency ϵ_{tot} is described as:

$$\epsilon_{tot} = \epsilon_{reco} \cdot \epsilon_{ID} \cdot \epsilon_{iso} \cdot \epsilon_{trigger} \tag{3.1}$$

where each single efficiency value depends only on each selection step. To reproduce the measured data efficiencies with Monte Carlo (MC) simulations, a *scale factor*, is required. This is defined as the ratio between data and MC and it is used as a multiplicative scale factor for the simulations. These correction factors, which are of the order of unity allow to cope with Monte Carlo mismodeling.

3.1 Electron reconstruction

In ATLAS, electrons identification is provided by a reconstruction algorithm which combines both ID and ECAL information (see Figure 3.1). The ID measurements give informations both on the electron angular direction and on the electron charge while ECAL measures electron energy. To improve the reconstruction performance, the algorithm combines informations on the energy leakage in the HCAL, the track
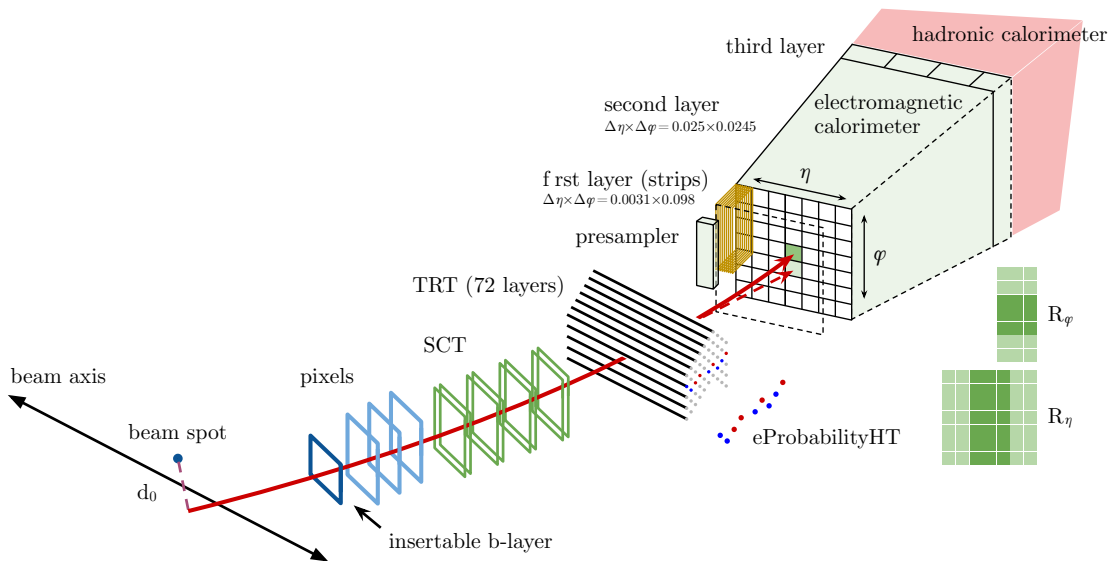
Figure 3.1: Schematic view of the electron reconstruction and identification [38].

quality criteria from ID objects and the cluster-track matching. In the ECAL, cluster are recreated using the section with the granularity of $\Delta\eta^{tower} \times \Delta\phi^{tower} = 0.025 \times .025$ (see Section 2.4.3), where the energy of cells in all longitudinal layers is summed to form the tower energy [39]. To this off-line procedure, called *seed-cluster* algorithm, an electron transverse energy above 2.5 GeV is required. These clusters are formed using a cluster algorithm which removes duplicates reaching a reconstruction efficiencies of 95% at $E_T = 7$ GeV and 99% at $E_T = 15$ GeV. Precise measurements of electrons identification and reconstruction in a range from 7 GeV to 50 GeV are performed using samples of isolated leptons from $Z \to ee$, $W \to e\nu$ and $J/\Psi \to ee$ events.

The track information from ID is obtained using both pattern recognition [40] (based on the pion hypothesis [41] for energy loss in the detector material) and track fit. The transverse momentum threshold for tracks reconstructed with the pion hypothesis is about 400 MeV. Then three hits in different silicon detector layers (IBL, PIX or SCT) with momentum larger than 1 GeV are required. The η and ϕ coordinates of the impact point are compared to a corresponding seed cluster position in both ID and ECAL. If one or more tracks is matched to a cluster, just the one that has the smallest ΔR is chosen as *primary track*. If any track is associated to the cluster, it is classified as an unconverted photon candidate. Electrons in the transition region $1.37 < |\eta| < 1.52$ are vetoed.

3.1.1 Electron identification

In the Particle IDentification (PID) algorithms a large set of observables are used. There are quantities related to the electron cluster and track measurements, as calorimeter shower shapes, information from TRT, track properties and variables measuring bremsstrahlung effects to discriminate signal from background. In the data analyses a likelihood-based method is used to obtain a PID. It is a multivariate analysis (MVA) technique which calculates the probability for the object to be signal or background evaluating signal versus background probability density functions (PDFs). The signal and background likelihoods, defined as $\mathcal{L}_{\mathcal{S}}$ and $\mathcal{L}_{\mathcal{B}}$
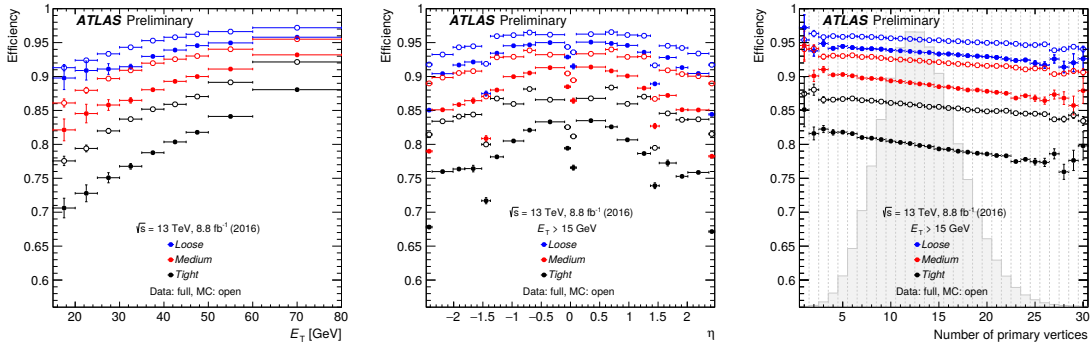
Figure 3.2: Electron ID efficiencies in $Z \rightarrow ee$ events as a function of transverse energy E_T (left), pseudorapidity η (center) and the number of reconstructed primary vertices (right). The low E_T range (from 7 to 20 GeV) is obtained using $J/\Psi \rightarrow ee$ events and suffers from a significant background contamination, while $Z \rightarrow ee$ events are used for measurements above 15 GeV [38].

respectively, are combined into the discriminant $d_{\mathcal{L}}$:

$$d_{\mathcal{L}} = \frac{\mathcal{L}_{\mathcal{S}}}{\mathcal{L}_{\mathcal{S}} + \mathcal{L}_{\mathcal{B}}}, \qquad \mathcal{L}_{\mathcal{S}(\mathcal{B})}(\vec{x}) = \prod_{i=1}^{N} P_{s(b)}, i(x_i) \qquad (3.2)$$

where $\vec{x}$ is the set of discriminating variables, $P_{s(b)}, i(x_i)$ the PDFs of the ith variable evaluated at x_i.

There are three levels of identification operating points for electron PID, defined in order of increasing background rejection: *Loose*, *Medium* and *Tight*. They have the same set of variables but use a different selection criteria. Loose electrons include also Medium and Tight electrons while Medium electrons include also Tight electrons. In Figure 3.2 the performance of the likelihood algorithms are shown, depending on the operating point. The signal efficiency for electrons candidates with $E_T = 30$ GeV is 75% for Tight electrons, 86% for Medium electrons and 91% for Loose electrons, increasing with E_T.

3.1.2 Electron isolation

To select prompt electrons, rejecting non-prompt lepton background, an isolation requirement is applied on electrons. Isolation consists in the definition of variables which quantify the energy of the particles produced around the electron candidates: $E_T^{cone0.2}$ variable is the calorimetric isolation energy defined as the sum of transverse energy of topological clusters within a cone of $\Delta R = 0.2$ around the electron cluster candidate; $p_T^{varcone0.2}$ variable is the track isolation defined as the sum of transverse momenta of all tracks within a cone of $\Delta R = \min(0.2, 10 \ / E_T \ [\text{GeV}])$ around the candidate electron track. Then a requirement on $|\Delta z_0 \sin \theta| < 3$ mm is applied.

In Table 3.1 the electron isolation operating points efficiencies are reported.

	Efficiency		
Operating Point	Calorimeter Isolation	Track Isolation	Total Efficiency
LooseTrackOnly	-	99%	99%
Loose	99%	99%	~98%
Tight	96%	99%	~95%

Table 3.1: Electron isolation operating point efficiency [39].

3.1.3 Electron trigger

The ATLAS online data processing system reconstructs and identifies electron candidates both at the L1 trigger and at the HLT. At L1, to calculate the energy in the inner region (core) and the surrounding (isolation) region the electron triggers use the signals recorded in ECAL and HCAL within the region of $\Delta \eta \times \Delta \phi \approx 0.4 \times 0.4$, which correspond to the so-called trigger towers. A veto on the hadronic leakage is also applied at L1 by requiring that the amount of energy measured in the HCAL behind the core of the EM cluster is below of a given threshold. It is also possible to set at L1 an isolation cut on the transverse energy around the EM core tower. This isolation and hadronic leakage veto requirements is not applied to electron candidates with $E_T > 50$ GeV.

At the HLT, electron candidates are reconstructed and selected in several steps to reject potential background candidates using information from calorimeter and tracking offline-like way. The clusters built from the deposit energy inside the ECAL cells are associated to the clusters reconstructed with the fast tracking algorithm[1] of ID within $|\eta| < 0.2$. Then, HLT uses offline-like algorithms, based on candidates selected in the first step, like described in Section 3.1.1. Except for the offline inclusion of the momentum loss due to the bremsstrahlung, online and

---

[1] A minimum p_T of 1 GeV is required.

offline likelihood-based identification work similarly. The discriminant is optimised with the online reconstructed shower shapes and track variables.

3.2 Muon reconstruction

Muon reconstruction in ATLAS consists in two parts: first the information is provided independently by the ID and MS; then the these two track segments are combined to form the muon tracks used in physics analyses. In the MS, trajectory is reconstructed by searching for hits inside each muon chamber. In each MDT chambers and nearby trigger chambers, the hits aligned on a trajectory in the not-bending plane are searched with the *Hough transform*, a pattern recognition algorithm. In the CSC detector, segments are formed using a separate combinatorial search in the η and ϕ planes.

The combined information between ID and MS allows to define four types of muons, as shown in Figure 3.3:

- **Combined (CB) Muon**: track reconstruction is performed independently in the ID and MS, then a combined track is obtained using both ID and MS information. The extrapolation takes into account the information from the outer part of the MS and performs a matching with the ID track;

- **Segment-tagged (ST) muons**: this type of classification is used for muons which cross only one layer of the MS chambers. A track reconstructed in the ID is classified as a muon if it is associated with at least one local track segment in the MDT and CSC;

- **Calorimeter-tagger (CT) muons**: a track in the ID is identified as a muon if it is matched to an energy deposit in the calorimeter compatible with a minimum-ionizing particle. They are used to recover the acceptance in the momentum range 15 GeV $< p_T <$ 100 GeV and $|\eta| < 0.1$;

- **Extrapolated (ME) muons**: also know as *Standalone muons*. For this type of muons, trajectory is reconstructed based only on the MS track with the addition of a loose requirement on compatibility with tracks originating from the IP. Crossing at least two layers of the MS and three layers in the forward region is required. They recover the acceptance in the region not covered by ID, $2.5 < |\eta| < 2.7$.

If two muon types share the same ID track, preference is given to CB muons, then to ST and finally to CT muons. In the MEs overlap, priority is given to the track with better fit quality.
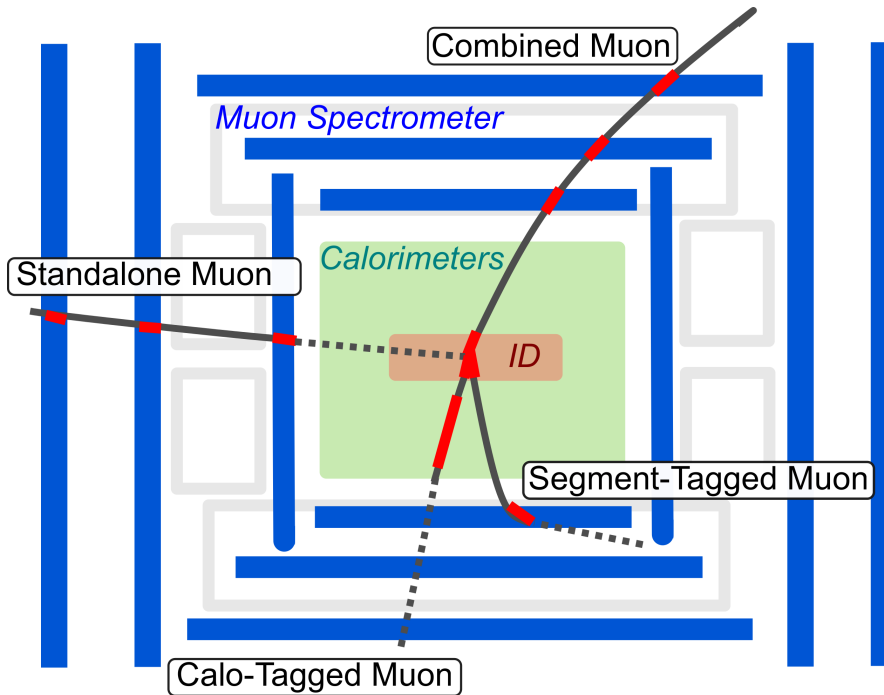
Figure 3.3: Schematic view of the reconstructed muon candidates in ATLAS.

3.2.1 Muon identification

Due to the high contamination from pion and kaon decays, tight quality require-
ments in the muon identification are required. Four types of muon identification
selection are provided:

- **Loose muons**: this identification is designed to maximize reconstruction
  efficiency while providing good-quality muons. CT and ST muons are con-
  sidered in the region $|\eta| < 0.1$ only. In the region $|\eta| < 2.5$ Loose muons are
  composed by $\sim 97.5\%$ of CB muons, $\sim 1.5\%$ of CT muons and $\sim 1\%$ of ST
  muons.

- **Medium muons**: they are designed to minimize the systematic uncertain-
  ties on the muon reconstruction and calibration. Only CB and ME muon
  tracks are considered. The former are required to have ≥ 3 hits in at least
  two MDT layers, except for tracks in the $|\eta| < 0.1$ region, where tracks with
  at least one MDT layer but no more than one MDT hole layer are allowed.
  ME muons are required to have at least 3 MDT/CSC layers and are used
  only in the region $2.5 < |\eta| < 2.7$. In the region $|\eta| < 2.5$, about 0.5% of
  Medium muons originate from the inside-out combined reconstruction strat-
  egy. All CB and ME muons included in the Medium classification satisfy

also the Loose criteria.

- **Tight muons**: this selection is designed to maximise the purity of muons preserving the reconstruction efficiency. Only CB muons with hits in at least two MS stations and satisfying the Medium selection criteria are considered.

- **High-p_T muons**: this working point was introduced to maximize the momentum resolution for muon with $p_T > 100$ GeV, as often required in BSM searches. CB muons passing the Medium selection and with at least three hits in three MS stations are selected. The requirement of three MS stations, while reducing the reconstruction efficiency by 20%, improves the transverse momentum resolution of muons above 1.5 TeV by about 30%.
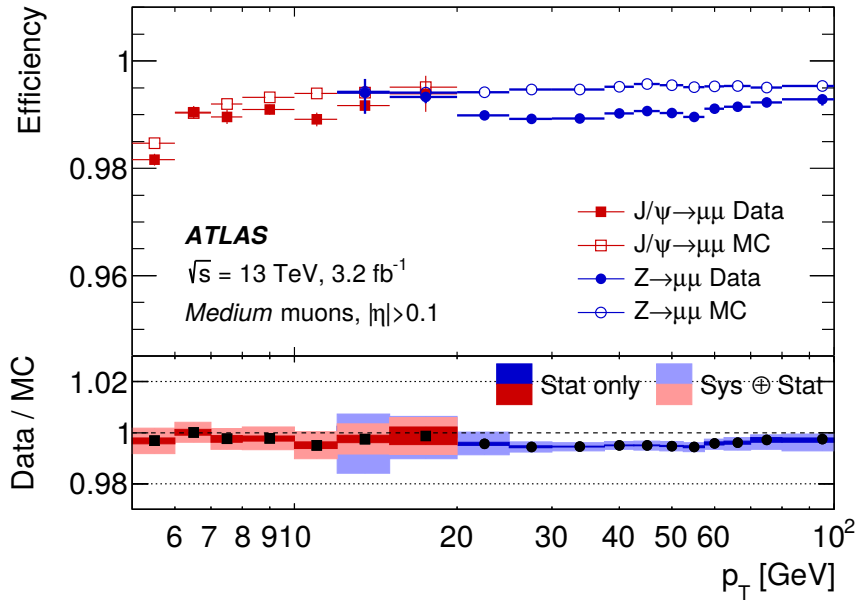
Figure 3.4: Reconstruction efficiency for the Medium muon selection as a function of the p_T of the muon, in the region $0.1 < |\eta| < 2.5$ as obtained with $Z \to \mu\mu$ and $J/\Psi \to \mu\mu$ events. The panel at the bottom shows the ratio of the measured to predicted efficiencies, together with the statistical and systematic uncertainties [42].

3.2.2 Muon isolation

Muons from heavy particle decays as W, Z or Higgs bosons tend to be isolated from other objects differently from muons produced by hadron decays background.
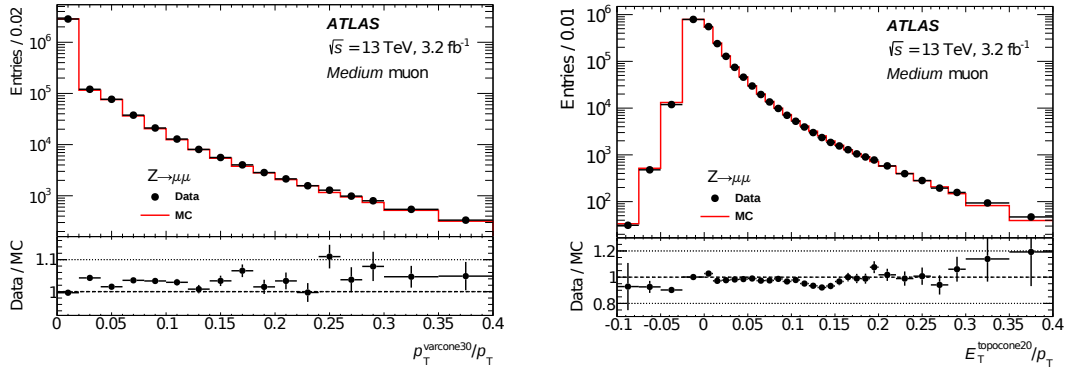
Figure 3.5: Left: Distribution of the track-based relative isolation variables measured in $Z \to \mu\mu$ events. Right: The same for the calorimeter-based variable. Muons are selected by the Medium identification algorithm [42].

The *muon isolation* is then a powerful tool to help in the signal to background discrimination.

Two variables are used to evaluate muon isolation: a track-based isolation variable ($p_T^{varcone30}$) and a calorimeter-based isolation variable ($E_T^{topcone20}$).

The $p_T^{varcone30}$ is defined as the scalar sum of the tracks transverse momenta. It considers muons with $p_T > 1$ GeV in a cone of $\Delta R = \min(10\text{GeV}/p_T^\mu, 0.3)$ around the muon direction, excluding the muon track itself. High-p_T muons reconstructions are improved by a p_T dependent cone size.

The $E_T^{topcone20}$ is defined as the sum of the transverse energy topological clusters in a cone of size $\Delta R = 0.2$ around the muon direction, after removing muon energy and corrections due to pile-up effects.

The *relative isolation variables* are used to determine the isolation criteria. They are defined as the ratio of the track- or calorimeter-based variable to the transverse momentum of the muon. In Figure 3.5 the distribution of these variables are reported.

3.2.3 Muon triggers

The L1 muon trigger selection uses informations about hits from the RPC in the barrel region and from TGC in the forward region. In the RPC a coincidence of hits in the three (two) layers for the highest (lower) muon trigger p_T thresholds is required. TGC measures directions in the wire-plane (bending) and in the strip-plane (non-bending). Except for muon with low p_T, the coincidence of both type of measurements in three layers is required.

The HLT reconstruction consists into two parts: a *fast* (trigger specific) and a *precision* (close to offline) reconstruction.
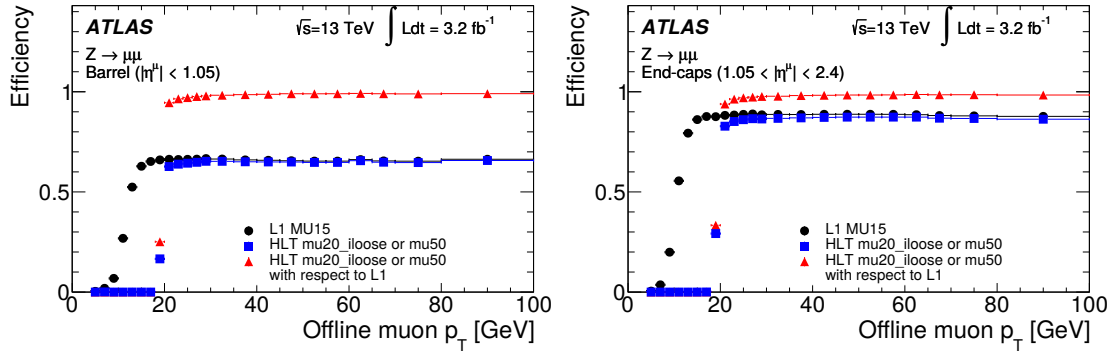
Figure 3.6: Efficiency of the L1 muon trigger `L1_Mu15` and the combined of the HLT muon triggers `mu20_iloose_L1Mu15` and `mu50` as a function of the probe muon p_T. Left: for the barrel region. Right: for the end-caps region [43].

In the fast stage, each L1 muon candidate is improved with the inclusion of precision data from the MDT chambers in the Region of Interest (RoI) defined by L1 candidate. Given the drift times and positions from the MDT, a track fit and a p_T measurements are performed to create MS-only muon candidates. It is combined with tracks reconstructed by the ID and using the offline track extrapolator is back-extrapolated to the IP to form a *combined* with refined track parameter resolution.

In the precision stage the RoI found in the fast stage to reconstruct the muon track are used. Similarly to the fast stage, muon candidates are formed as MS-only and than combined with ID tracks. If there are no ID tracks matching, combined muons are searched with the extrapolation of the ID track to the MS. In Figure 3.6 the efficiencies of few muons triggers as a function of the p_T of the offline muon track are reported.

3.3 Jet reconstruction

In ATLAS, jets are reconstructed using three-dimensional clusters of topologically connected cells (*topo-cluster*) of the calorimeters. The topo-cluster reconstruction involves seed cells identification with at least 4σ of energy significance above the noise level, where the noise is defined as:

$$\sigma_{\text{noise}} = \sqrt{\left(\sigma_{\text{noise}}^{\text{electronic}}\right)^2 + \left(\sigma_{\text{noise}}^{\text{pile-up}}\right)^2} \tag{3.3}$$

The nearby cells with an energy significance higher than 2σ with respect to the noise are iteratively added to form the clusters. After topo-cluster reconstruc-

tion, a splitting algorithm divides clusters in energy categories using a local energy maxima criterion. Individual clusters are calibrated using local properties as calorimeter depth, energy density and isolation with respect to close-by clusters. This procedure is called *Local hadron Cluster Weighting* (LCW). It is a calibration which classifies topo-cluster along a continuous scale as being electromagnetic or hadronic, using shower shapes and energy densities (see Figure 3.7). Due to the
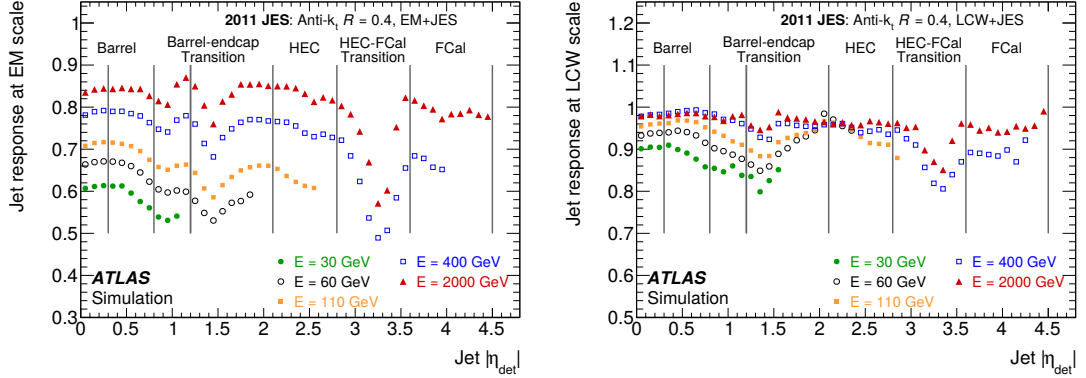
Figure 3.7: Average response of simulated jets formed from topo-clusters for the EM scale (left) and for the LCW scale (right). The response is shown separately for various truth-jet energies as function of the uncorrected jet pseudorapidity. Are also indicated the different calorimeter regions [44].

many higher order calculations (NLO, NNLO) available, an infrared and collinear (IRC)[2] safe algorithm is required.

One of the most used jet reconstruction algorithm in ATLAS is the *anti-k_T*. It is based on the distance d_{ij} between two particles or *proto-jets* (the intermediate reconstruction objects) and the distance d_{iB} between the particle i and the beam, B. For each cluster, the algorithm evaluates the distance d_{ij} with each other cluster or pseudo-jet j:

$$d_{ij} = \min\left(p_{T,i}^{2k}, p_{T,j}^{2k}\right) \frac{\Delta R_{ij^2}}{R^2} \tag{3.4}$$

where ΔR_{ij}^2 is the angular distance between i and j, defined as:

$$\Delta R_{ij}^2 = (\eta_i - \eta_j)^2 + (\phi_i - \phi_j)^2 \tag{3.5}$$

where $p_{T,i(j)}$, $\eta_{i(j)}$ and $\phi_{i(j)}$ are the transverse momentum, the pseudorapidity and the azimuthal angle of the $i(j)$ object respectively; R is a parameter to limit the

---

[2]An observable is defined as infrared and collinear safe if, in the limit of a collinear splitting, or the emission of an infinitely soft particle, it remains unchanged. This property allows cancellation of real and virtual divergences in higher order calculations.

cone radius of jet and k is an anti-k$_T$ parameter fixed equal to -1. For each cluster or proto-jet i, the distance from the beam is evaluated as:

$$d_{iB} = p_{T,i}^{2k}. \tag{3.6}$$

The two distances d_{ij} and d_{iB} are compared to find the minimum values among them. If the minimum distance is represented by d_{ij}, i and j are combined into the same proto-jet and the procedure is repeated from the first step. On the other hand, if $d_{iB} < d_{ij}$, the cluster i is considered as a final state and it is not considered in further iterations.

To remove effectively the pile-up jets, the jet-vertex-tagger (JVT) technique using track and vertex information, is provided [44].

3.4 τ-lepton reconstruction

The τ-lepton is the heaviest lepton of the SM with a mass of about 1.78 GeV and it can decay either leptonically or hadronically with a probability of 35% and 65% respectively. The hadronic decay produces one charged pion in the 72% of events and three charged pions in the 22% of events. In the 68% of the hadronic decays, at least one neutral pion is produced. Neutral and charged hadrons stemming from these decays provide the visible part of them, thus they are referred as $\tau_{\text{had-vis}}$.

Due to the high probability of hadronic decays, the main background is due to jets of energetic hadrons produced by fragmentation of quarks and gluons. To discriminate $\tau_{\text{had-vis}}$ candidates from jets, discriminating variables based on the narrow shower in the calorimeter, the distinct number of tracks and the displaced τ-lepton decay vertex are used.

Based on jet reconstruction, jets seeding tau candidates are additionally required to have $p_T > 10$ GeV and $|\eta| < 2.5$. Tau candidates in the transition region between the barrel and forward calorimeters, $1.37 < |\eta| < 1.52$, are vetoed. The tau primary vertex (PV) is identified as the vertex with the largest fraction of momentum from tracks associated with the jet within $\Delta R < 0.2$. The tracks must also have $p_T > 1$ GeV, $|d_0| < 1$ mm and $|\Delta z_0 \sin \theta|$.

If these requirements are satisfied the tracks are then associated to core ($0 < \Delta R < 0.2$) and isolation ($0.2 < \Delta R < 0.4$) regions around the tau candidate.

τ-lepton identification is designed to reject background from jets. It uses a Boosted Decision Tree (BDT) methods. BDT are trained with a simulated Z $\rightarrow \tau\tau$ for signal and data with dijet events for background. There are three working points: **Loose**, **Medium** and **Tight**, corresponding to different tau identification efficiency values, designed to be independent of p_T.

3.5 Missing Transverse Energy

The missing transverse energy may be indicative of weakly-interacting particles and it is mainly due to undetected particles. In the SM this arises mainly from neutrinos, but there are also candidate particles in theories beyond the SM. Then, E_T^{miss} is an important variable in searches for exotic signatures. However, contributions to the E_T^{miss} can also result from particles which escape the acceptance of the detector or it may originate from the electronic noise into the calorimeters and MS. To reconstruct the effective value of E_T^{miss} considering all these factors, many algorithms using the topological calorimetric clusters are applied.

The missing transverse energy vector is defined as:

$$\vec{E}_T^{miss} = \sum_{calocells} E_{Ti} \hat{u}_i \tag{3.7}$$

where $\hat{u}_i$ is the unit vector between the collision point and the position of the energy deposit observed in the ith cell of the calorimeter.

To distinguish real E_T^{miss} due to undetected particles from E_T^{miss} due to resolution smearing, E_T^{miss} significance $\mathcal{S}$ must be evaluated. It is defined as the log-likelihood ratio quantifying how likely the reconstructed missing transverse momentum $\vec{E}_T^{missReco}$ is consistent with true missing transverse momentum $\vec{E}_T^{missTruth}$. A high value of $\mathcal{S}$ indicates that the observed E_T^{miss} in the event is not well explained only by resolution smearing, suggesting that the event may contain unseen objects such as neutrinos or more exotic weakly interacting particles.

Then, significance $\mathcal{S}$ can be written as:

$$\mathcal{S} = 2 \ln \frac{\mathcal{L}\left(\vec{E}_T^{miss} = \sum_i \vec{E}_{Ti}^{missReco}\right)}{\mathcal{L}\left(E_T^{missTruth} = 0\right)}. \tag{3.8}$$

3.5.1 E_T^{miss} reconstruction and object selection

The $\vec{E}_T^{missReco}$ in ATLAS is characterised by two contributions:

Hard objects: which include fully reconstructed and calibrated particles, i.e. electrons, photons, τ-leptons, muons and jets;

Soft term: which consist of signals not associated with any of reconstructed hard objects.

Considering these two types of terms, the E_T^{miss} components in the x-y transverse plane are calculated as:

$$E_T^{miss} = E_T^{miss,e} + E_T^{miss,\gamma} + E_T^{miss,\text{Jets}} + E_T^{miss,\mu} + E_T^{miss,\tau} + E_T^{miss,\text{soft}} \tag{3.9}$$

where each object term is given by:

$$E_T^{miss} = -\sum_i \vec{p}_T(i) \tag{3.10}$$

for a visible particle with flavour i.

To improve the E_T^{miss} reconstruction efficiency, these reconstructed object are associated to the calorimeter signals in the following order: electrons, photons, hadronically decaying τ-leptons, jets and muons.

An important quantity to parametrize the event activity of the hard objects is H_T, which is defined as the scalar sum of the momenta from all the reconstructed hard objects:

$$H_T = \sum p_T^e + \sum p_T^\gamma + \sum p_T^\tau + \sum p_T^{\text{Jets}} + \sum p_T^\mu \tag{3.11}$$

The physics objects entering in Equation 3.10 and 3.11 are:

Electrons

Electrons are required to have medium reconstruction quality and an associated ID track matched to the ECAL cluster. They are calibrated using a loose isolation criteria. These electrons must also have $E_T > 7$ GeV and $|\eta| < 2.47$ or $1.37 < |\eta| < 1.52$.

Muons

Similarly to the electrons, muons are selected with medium reconstruction and loose isolation criteria. They are reconstructed matching tracks from the MS and from the ID. A muon with $p_T > 7$ GeV and $|\eta| < 2.5$ are required.

Jets

Jets are reconstructed with the anti-k_t algorithm using a distance parameter of R=0.4. After the calibration [46], which includes also a correction for pile-up, jets are required to have $p_T > 20$ GeV and $|\eta| < 4.5$.

Following the jet vertex tagger (JVT) [45], a fraction of jets track with $p_T < 60$ GeV and $|\eta| < 2.4$ must be produced from the primary vertex to reduce the pile-up effects.

Jets reconstructed with 20 GeV $< p_T < 60$ GeV and $|\eta| < 2.4$ are only accepted if they are tagged by JVT > 0.59.

τ-leptons

τ-leptons are reconstructed searching narrow jets from its hadronically decay with $p_T > 10$ GeV and $|\eta| < 2.5$ with a low track-multiplicity as well. They are calibrated at the τ-lepton energy scale (TES) using the LCW. Candidates must pass the medium quality selection and having $p_T > 20$ GeV after TES corrections.

Soft term

The soft term is an important variable of the E_T^{miss} reconstruction, mainly in final states with low hard-object multiplicity. It is reconstructed using only the ID tracks information, then using p_T of soft charged particles. Tracks associated with hard scatter vertex and which satisfy the following requirements are included:

- $p_T > 400$ MeV;

- $|d_0| < 1.5$ mm;

- $|z_0 \sin \theta| < 1.5$ mm;

- $\Delta R\,(\text{track}, e/\gamma \text{cluster}) > 0.5$;

- $\Delta R\,(\text{track}, \tau) > 0.2$.

A first order estimation of the Track-based Soft Term (TST) resolution can be taken from the $Z \to \ell\ell$ sample with a jet veto. In the right plot of Figure 3.8, the agreement of TST E_T^{miss} measured using 8.5 fb^{-1} of Run-2 ATLAS data and MC simulations from $Z \to ee$ events is shown. In the left plot of Figure 3.8, the mean of the TST distribution as a function of the hard term p_T measured using 36.5 fb^{-1} of Run-2 ATLAS data agrees with Monte Carlo simulation within the systematic uncertainty is shown.

3.6   Overlap removal

The Overlap Removal (OR) algorithm is used to identify and remove objects which pass the previous selections but are too close one each other having a high probability of bad reconstruction or object duplication. The OR is composed of several steps depending the objects considered:

- if a muon and an electron are in the same cone $\Delta R < 0.1$, only the muon is retained. This choice is due to the minimal fraction of lost energy (above 2 GeV, the value of the *minimum ionizing particle*), which could not allow a correct track identification;
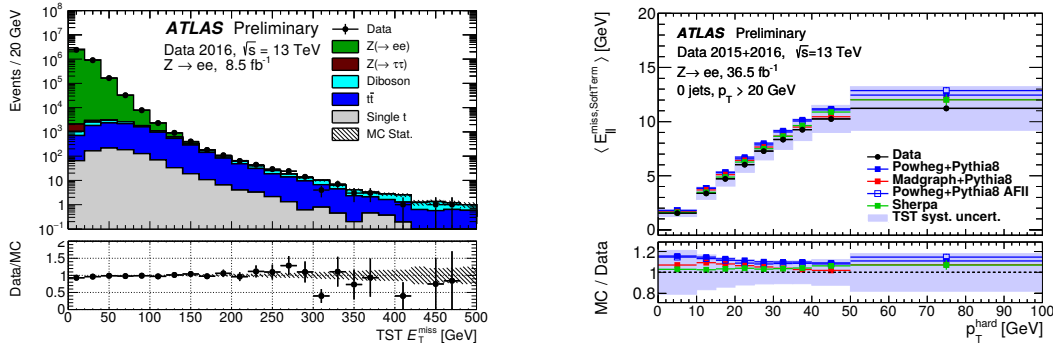
Figure 3.8: Left: TST E_T^{miss} distribution for a selection of Z boson decays to a pair of electrons at Run-2 ATLAS data. The shaded band represents the statistical uncertainty of Monte Carlo simulations. Right: The mean of the TST distribution projected in the direction longitudinal to the hard term p_T for $Z \rightarrow ee$ events measured using Run-2 ATLAS data and Monte Carlo simulation. The shaded band represent the systematic uncertainty [47].

- where a jet and an electron are in the same cone $\Delta R < 0.3$, only the electron is selected. In fact, an high energy electron can reach the HCAL being identified as a jet;

- where a muon and a jet are in the same overlapping cones, two types of distance can be used to define the overlapping cone. In final states with very high-p_T objects, a p_T dependent distance is used with $\Delta R < 0.4 + \frac{10 \text{ GeV}}{p_T}$; with lower p_T values a constant distance $\Delta R < 0.4$ is considered. In both cases the muon is removed.

3.7 ATLAS data format

In high energy physics, analysts need to be able to run over data sample frequently, performing a huge variety of event selections retrieving different sets of information of the data collected by the experiment. In ATLAS, data and MC events are managed and reconstructed using the software framework *Athena* [48]. After reconstruction, all events are stored into the *Analysis Object Data* (AOD) format, which includes also objects calibrations necessary to the ATLAS performance groups. Because of their large size, they are not practical to analyse. To speed up the analysis chain, a data reduction strategy was developed during Run 2 using an offline tool: the *Derivation Framework* [49]. Its operating scheme is shown in Figure 3.9. The derivation starts from data and simulated samples pro-
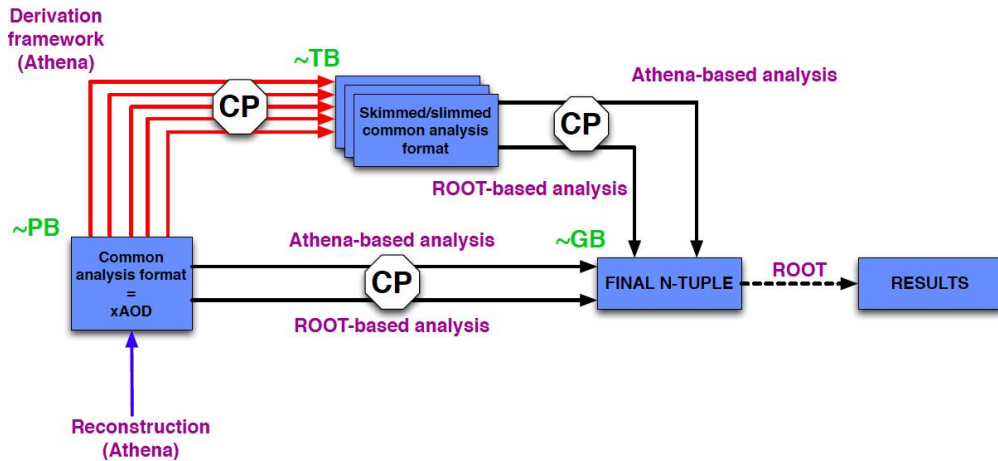
Figure 3.9: Scheme of the Derivation Framework used by ATLAS. The samples size is reduced from the order of PB to few GB.

cessed by Athena in a format called xAOD, providing an output of few % of events of the original ones (the so-called Derived-xAOD, DxAOD).

Each DxAOD is produced from the xAOD following four steps:

skimming: remove events that do not pass particular derivation requirements;

thinning: remove uninteresting reconstructed objects (jets, tracks, calorimeter clusters, etc.) from events;

slimming: remove not necessary informations from these objects;

augmentation: add additional content to the DxAOD not found in the input data.

There are many different derivation formats, each targeting a particular group of analyses[3]. In the analysis shown in Chapter 4, the `EXOT12` derivation is used. It consists in an events selection where at least two leptons (in any flavour combination) that satisfy the following requirements are contained: electrons with $p_T > 20$ GeV that pass `LHLoose` identification criteria, muons with $p_T > 20$ GeV that are identified as CB[4].

---

[3]Each targeting $\sim 1\%$ of the total size of the primary xAODs.

[4]These p_T requirements is applied only on the two most energetic leptons.

SEARCH FOR HEAVY LEPTON PRODUCTION

In this section a complete description of the analysis strategy for the search of Type-III Seesaw heavy lepton production in ATLAS is provided, focusing on the three-lepton final state. The analysis is performed using 2015, 2016 and 2017 data collected by the ATLAS detector at $\sqrt{s} = 13$ TeV corresponding to a total integrated luminosity of 79.8 fb^{-1}. A preliminary result on the search of an eventual signal due to heavy lepton production is also presented.

4.1 Signals and background description

The description of the analysis final state and the samples used to study the statistical sensitivity in the target channel are illustrated in the following sections.

4.1.1 Analysis final state

Differently from the analysis described in Section 1.4.3, which considers both hadronic and leptonic decays of the two W bosons, a topology where both W bosons decay leptonically (*3l channel* in the following) is considered. This final state has a total charge of ± 1, containing three high-p_T leptons and large E_T^{miss} due to three neutrinos, without any jets presence (see Figure 4.1). Unlike the 2l2j channel, in the 3l channel the presence of neutrinos in both heavy leptons decay chains does not allow a precise reconstruction of the main variables of the analysis, like the invariant mass of the heavy leptons. However, this topology has the great advantage to be a purely leptonic state so - from an experimental point of view - it is affected by low systematic uncertainties almost only associated to the lepton reconstruction resulting to be dominated by the statistical uncertain-
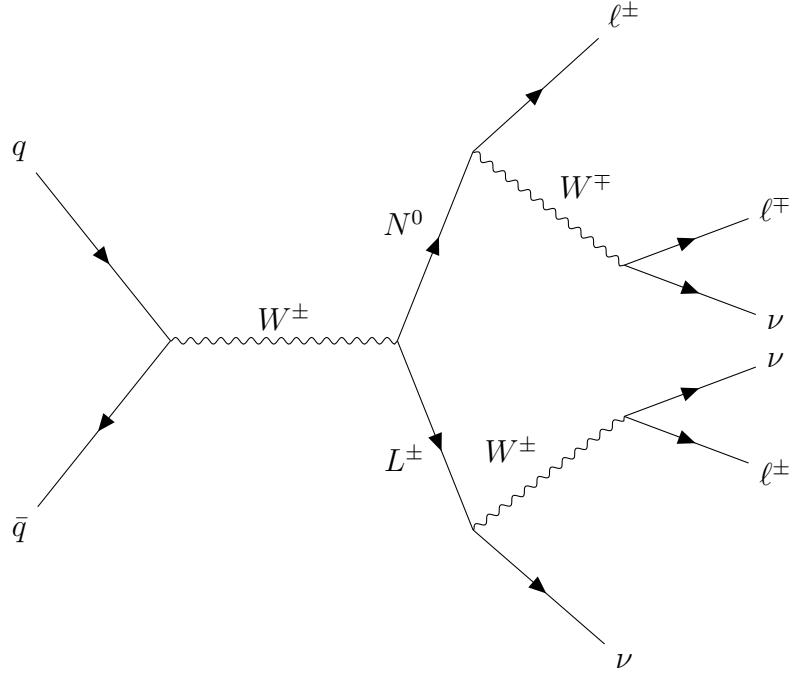
Figure 4.1: Feynman diagram for the dominant contribution to three-charged-leptons and three neutrinos final states in pair production of N^0 and $L^\pm$ in the Type III SeeSaw mechanism.

ties. Furthermore, the lower background in the three-lepton final state provides a higher discovery potential compared to the two-lepton final state.

Decay channels of heavy leptons into Z's and Higgs bosons are not considered in this analysis. Moreover, only "light" leptons ($\ell = e, \mu$) are considered, including light leptons from tau decays. The light-lepton flavour and charge combinations, with the requirement of total charge equal to ± 1, correspond to 12 different final states (see Table 4.1). However, these 12 final states are merged into a single final state to increase the number of events and therefore the statistical power of the analysis.

4.1.2 Collision Data and Monte Carlo samples

Collision Data

Experimental ("collision") data used in this analysis were collected during 2015, 2016 and 2017. The average number of pp interactions per bunch crossing (pile-up) is reported in Table 2.1. All data collected by the ATLAS detector are divided into Luminosity Blocks (LB) and the data in one LB are characterized by the

System Charge	+1	-1
Topology	$\mu^- e^+ e^+$	$\mu^+ e^- e^-$
	$e^- \mu^+ \mu^+$	$e^+ \mu^- \mu^-$
	$\mu^- e^+ \mu^+$	$\mu^+ e^- \mu^-$
	$e^- e^+ \mu^+$	$e^+ e^- \mu^-$
	$e^- e^+ e^+$	$e^+ e^- e^-$
	$\mu^- \mu^+ \mu^+$	$\mu^+ \mu^- \mu^-$

Table 4.1: The 12 final states obtained by three leptons combination.

same data taking conditions. Among all of the LBs, only the ones where all the sub-detectors were in good data-taking conditions are selected. This information is collected into the so-called *Good Run List* (GRL). The luminosities corresponding to the various GRLs used in this analysis are 3.2 fb^{-1}, 33.0 fb^{-1} and 43.6 fb^{-1} for 2015, 2016 and 2017, respectively.

The analysis is performed using the `EXOT12` derivations (see Section 3.7). Events are selected using single, double and three-lepton triggers, as reported in Table 4.2, used in OR logical combination.

Monte Carlo samples

Background processes were simulated using the MC generators and settings listed in Table 4.3. Signal MC samples are simulated for heavy leptons masses in the range 200-700 GeV with a mass step of 50 GeV. `MadGraph5_aMC@NLO` interfaced to `Pythia8.212` for parton showering is used for signal generation. These samples are generated at the leading order and the `NNPDF3.0LO` PDF is used for the matrix element calculation. Only processes decaying into W bosons are enabled, while Z and Higgs bosons decays are excluded. At the generator level, all the leptonic flavours and all types of W decays are considered in the final states.

An irreducible background for this analysis comes from SM processes producing three leptons in the final state, the so-called *prompt* background. It is mainly originated by the production and decay of dibosons (WZ and ZZ production). The most relevant contribution is due to the WZ production where both bosons decay into leptons; a smaller contribution comes from ZZ events where the Z bosons decay leptonically, and one of the leptons is either outside of the detector acceptance or mis-reconstructed. Backgrounds from jets and photons that are misidentified as leptons are also taken into account, including events from Drell-Yan ($q\bar{q} \rightarrow Z/\gamma^* \rightarrow \ell^+\ell^-$), W + jets, Z + jets and $t\bar{t}$ processes.

MC samples are normalised to their theoretical cross-sections, referenced in Table

Channel	2015	2016	2017
ee	HLT_2e12_lhloose_L12EM10VH	HLT_2e17_lhvloose_nod0	HLT_2e17_lhvloose_nod0_L12EM15VHI HLT_2e24_lhvloose_nod0
μμ	HLT_mu26_imedium OR HLT_mu50	HLT_mu26_imedium OR HLT_mu50 HLT_mu22_mu8noL1	HLT_mu26_imedium OR HLT_mu50 HLT_mu22_mu8noL1
eμ	HLT_e17_lhloose_nod0_mu14 HLT_e7_lhmedium_nod0_mu24	HLT_e17_lhloose_nod0_mu14 HLT_e7_lhmedium_nod0_mu24 HLT_e26_lhmedium_nod0_L1EM22VHI_mu8noL1	HLT_e17_lhloose_nod0_mu14 HLT_e26_lhmedium_nod0_mu8noL1
eee		HLT_e17_lhvloose_nod0_2e9_lhvloose_nod0	HLT_e24_lhvloose_nod0_2e12_lhvloose_nod0_L1EM20VH_3EM10VH
eeμ		HLT_2e12_lhloose_nod0_mu10	HLT_2e12_lhloose_nod0_mu10
eμμ		HLT_e12_lhloose_nod0_2mu10	HLT_e12_lhloose_nod0_2mu10
μμμ		HLT_mu20_2mu4noL1	HLT_mu20_2mu4noL1

Table 4.2: Overview of the lepton triggers used to select interesting events in all the considered Type-III Seesaw channels.

Physics process	Event generator	ME PDF Set	Cross-section normalization	Cross-section (pb)	Parton Shower	Parton Shower tune
Signal	MadGraph5_aMC@NLO	NNPDF3.0LO	LO		Pythia 8.212	A14
Drell-Yann $Z/\gamma^* \to e^+e^-/\mu^+\mu^-/\tau^+\tau^-$	Sherpa 2.2.1	NNPDF3.0NNLO	NLO	6254	Pythia 8.212	Sherpa default
Top $t\bar{t}$ Single top	Powheg-Box v2 Powheg-Box v2	NNPDF3.0NNLO CT10	NNLO NLO	76.9 71.7	Pythia 8.212 Pythia 6.428	A14 Perugia 2012
Diboson ZZ, WZ, WW	Sherpa 2.2.1 & 2.2.2	NNPDF3.0NNLO	NLO	74.5	Pythia 8.212	Sherpa default

Table 4.3: Simulated signal and background event samples used in the search for Type-III Seesaw heavy lepton production. For each sample the corresponding event generator, parton shower generator, cross-section normalisation, PDF set used for the matrix element and set of tuned parameters are reported.

4.3 and 4.4 for background and signal respectively.

Signal mass (GeV)	200	250	300	350	400	500	550	600	650	700
Cross-section (fb)	183	72.8	34.5	18.2	10.4	3.92	2.54	1.69	1.15	0.797

Table 4.4: Signal sample cross-sections for each of the test mass point simulated.

4.1.3   Background Estimation

Besides the prompt background contribution described in the previous section, another source of background comes from mis-reconstructed objects. Two types of mis-reconstructions are here identified:

- *Fake leptons*: they are objects originated from in-flight decays of mesons (*non-prompt leptons*), jets reconstructed as leptons and electron-photon conversions;

- *Charge-flipped leptons*: events where an electron is reconstructed with the wrong charge. This effect is negligible for muons, as confirmed by previous studies (where the probability for a muon to flip its charge was measured to be $< 10^{-5}$).

Due to the small contribution of these effects in this analysis, it was relied on the MC capability to correctly reproduce fake leptons and charge flips. An alternative procedure to obtain a data-driven correction is presented in appendix A.

4.2 Pre-selection criteria and event yields

To select the final states described in Section 4.1.1, some pre-selection criteria on signal and background MC samples have been applied before the selections needed to define the analysis regions.

4.2.1 Object definitions

In ATLAS, standard physical objects like leptons are reconstructed using different requirements on the reconstruction algorithms, called *working points* (WP). They are based on the lepton reconstruction, identification and isolation, illustrated in Chapter 3 and correspond to different efficiency and purity levels. The recommended WPs provides a good discrimination between prompt and fake leptons. For this analysis, a set of identification criteria defined in Sections 3.1.1 and 3.2.1 for electrons and muons, is used. For electrons `LHMedium` WP is chosen providing an efficiency of 95% for electrons of $E_T = 40$ GeV. The `LHMedium` WP classifies a subset of electrons tagged by the `LHLoose` WP. The object definition for electrons used in this analysis is reported in the middle column of Table 4.5. For muons, the

Requirements	Signal electrons (tight)	Signal muons (tight)
Identification	`LHMedium`	`Medium`
Isolation	`Loose`	`FixedCutTightTrackOnly`
p_T cut	$p_T > 10$ GeV	$p_T > 10$ GeV
η cut	$|\eta| < 2.47$ and veto $1.37 < |\eta| < 1.52$	$|\eta| < 2.5$
$|d_0|/\sigma_{d_0}$ cut	$|d_0|/\sigma_{d_0} < 5$	$|d_0|/\sigma_{d_0} < 3$
$|z_0 \sin\theta|$ cut	$|z_0 \sin\theta| < 0.5$ mm	$|z_0 \sin\theta| < 0.5$ mm

Table 4.5: A summary of the object definition requirements for electrons and muons.

selection criteria outlined in Table 4.5 are used. The track-based isolation variable $p_T^{varcone30}$ (defined in Section 3.2.2) is used to discriminate between isolated and not-isolated muons. `FixedCutTightTrackOnly` isolation WP is used, which corresponds to $p_T^{varcone30} < 0.6$ cut. Requirements on the transverse impact parameter significance and longitudinal impact parameter are used to distinguish between prompt and secondary leptons.

To measure the missing transverse energy of the system, due to the presence of the three neutrinos escaping detection or to other particles outside the acceptance, the E_T^{miss} variable described in the Section 3.5 is considered, with the tight WP.

4.2.2 Final samples at pre-selection level

The pre-selection allows a first isolation level of events which will be subject to further cut refinements during the analysis region definition. These events must satisfy the following requirements:

- presence of no jets;

- number of light leptons strictly equal to 3;

- minimum leptons $p_T = 10$ GeV;

- system charge equal to $\pm$ 1.

A veto on the Z mass window is also included, rejecting events where one of the same-flavour opposite-sign pairs has a mass in the window 85 GeV $< m_{\ell\ell} <$ 95 GeV. The number of events which survive the pre-selection cuts for each samples are reported in the Table 4.6. According to the Monte Carlo statistics generated, only diboson events survive all the analysis cuts, while other backgrounds are mainly suppressed by the three lepton requirements.

4.3 Analysis Strategy

Once signal and background events have been pre-selected, they are ready to be further studied to refine the analysis. The first step consists in looking for cuts which maximize the search sensitivity. Then, the *discriminating variables* which will allow to define the analysis regions will be searched for. The aim is to maximize the background rejection for a given signal mass point on the full range of variables. The cut optimization is performed studying multi-dimensional distributions and searching for variables' values which maximize the signal significance, which is defined as:

$$S = \sqrt{2 \cdot [(s + b) \log (1 + s/b) - s]} \tag{4.1}$$

where s and b are the number of signal and background events, respectively [50].

In order to perform a statistical interpretation of the data, two hypothesis are needed: one consistent with only SM background expectation, the other matching the background plus signal hypothesis at a certain *confidence level*. These two types of hypothesis are fitted using two regions where different categories of events are defined satisfying different sets of requirements, the so-called *analysis regions*. A schematic view of a template analysis strategy is illustrated in Figure 4.2. The region of the phase space where the signal is expected to produce an excess over the SM expectation is defined as *signal region* (SR). A good control of the backgrounds is necessary to understand the SM background contribution and

Background	Initial	Generated	Jets-veto	3 leptons	Z-veto	$Q = \pm 1$
Diboson	$4 \cdot 10^8$	$2.9 \cdot 10^7$	$3 \cdot 10^6$	$1.5 \cdot 10^6$	$6.9 \cdot 10^5$	$6.9 \cdot 10^5$
Drell-Yan	$3.7 \cdot 10^8$	$5.6 \cdot 10^7$	$1.2 \cdot 10^6$	0	0	0
Top	$1.6 \cdot 10^7$	$1.2 \cdot 10^5$	2254	1	0	0
$t\bar{t}$	$7.8 \cdot 10^7$	$5.6 \cdot 10^6$	$2.9 \cdot 10^4$	3	0	0
Signal mass-point (GeV)						
200	$2.3 \cdot 10^5$	$1.1 \cdot 10^5$	$1.4 \cdot 10^4$	4929	4637	4622
250	$2.3 \cdot 10^5$	$9.5 \cdot 10^4$	6828	4903	4694	4674
300	$2.3 \cdot 10^5$	$9.8 \cdot 10^4$	6598	4930	4749	4738
350	$2.3 \cdot 10^5$	10^5	6601	5002	4883	4865
400	$2.3 \cdot 10^5$	10^5	6412	4945	4830	4794
500	$2.3 \cdot 10^5$	10^5	6014	4837	4764	4740
550	$2.3 \cdot 10^5$	10^5	5989	4815	4759	4730
600	$2.3 \cdot 10^5$	10^5	5885	4796	4739	4708
650	$2.3 \cdot 10^5$	10^5	5731	4717	4650	4619
700	$2.3 \cdot 10^5$	$1.1 \cdot 10^5$	8092	4737	4698	4667

Table 4.6: Cutflow table showing the number of events passing each cut for background and signal samples. The column "Generated" is refers to the number of events at `EXOT12` derivation level.
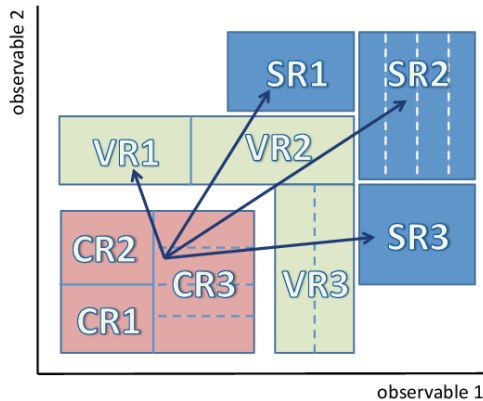
Figure 4.2: Scheme of a template analysis strategy with multiple control, validation and signal regions. Each region can be made with single or multiple bins.

to justify any possible excess of data. Whether the shape of signal differs from the background one, this also represents a powerful information to be used for signal-background separation. A *control region* (CR) is defined in order to constrain a specific background, while a *validation region* (VR) can be used to prove the goodness of the background estimation before applying it to the signal region.

4.3.1 Selection Optimization

The main observables used to identify and reconstruct a physics process are commonly related to the kinematic variables of the particles. The ones studied in this analysis are:

- Momentum of leptons, which depend on the mass of the decaying particles. Due to higher mass of signal particles with respect to the backgrounds ones, these variables can provide a good discrimination power;

- E_T^{miss} significance: since the signal regions are characterized by the presence of three neutrinos, E_T^{miss} significance is an important variable to investigate. The W bosons originated from the heavy lepton decays provide an average E_T^{miss} higher than that in the dominant SM processes such as W or Z decays.

Their distributions at the pre-selection level are shown in Figure 4.3 for a template mass point of 200 GeV. Other variables were tested to discriminate these events, as the invariant mass of the three leptons, but they are affected by a strong correlation of each lepton with the other one and are therefore slightly less discriminating.

71

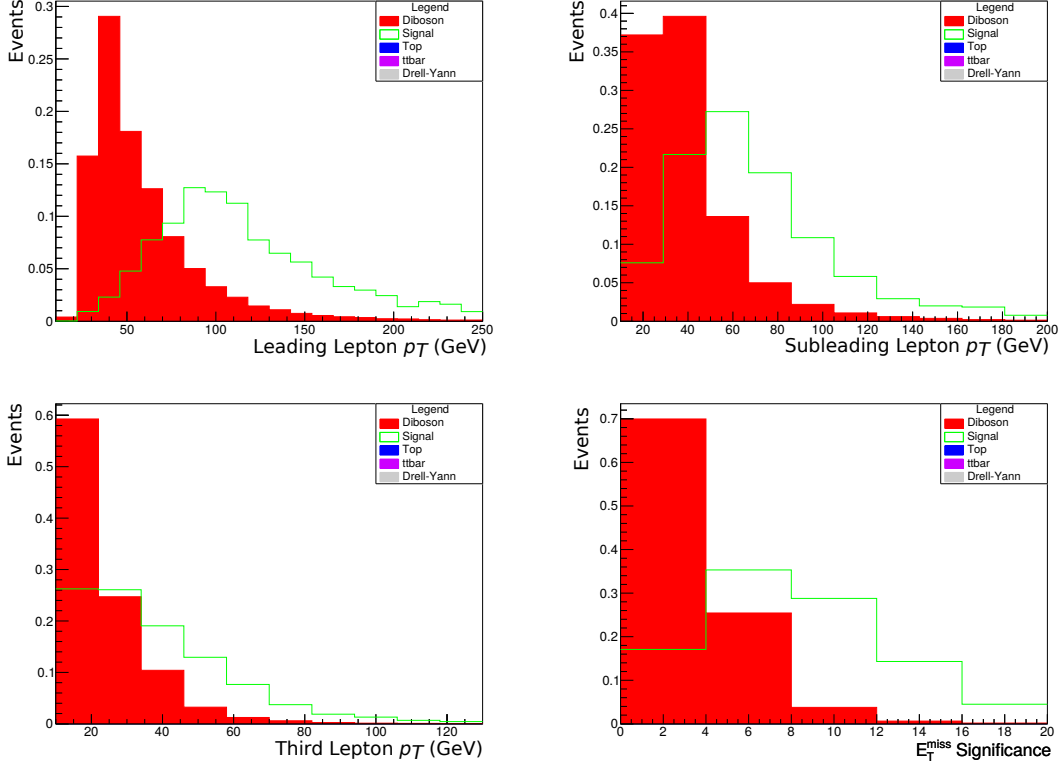A multi-dimensional analysis was then performed to study the phase space region

Figure 4.3: Distributions of p_T for the leading (top left), subleading (top right) and third (bottom left) lepton and E_T^{miss} significance (bottom right). The signal mass-point at 200 GeV is used as an example. The distributions are normalized to unity to ease the shape comparison.

obtained by scanning a selected range of these variables, as reported in Table 4.7. The resulting phase space regions were studied using the variable defined in Equa-

Variable	Minimum	Maximum	Number of bins
Leading lepton p_T (GeV)	26	150	100
Subleading lepton p_T (GeV)	20	100	100
Third lepton p_T (GeV)	10	30	5
E_T^{miss} significance	0	10	5

Table 4.7: Range of the variables used in the analysis and corresponding number of bins used for each kinematical variable.

tion 4.1, plotted in a multi-dimensional distribution as a function of each of the 3

leptons p_T and of the E_T^{miss} in order to define the analysis regions (in Appendix B all of the significance plots are reported). Analysing the multi-dimensional signifi-
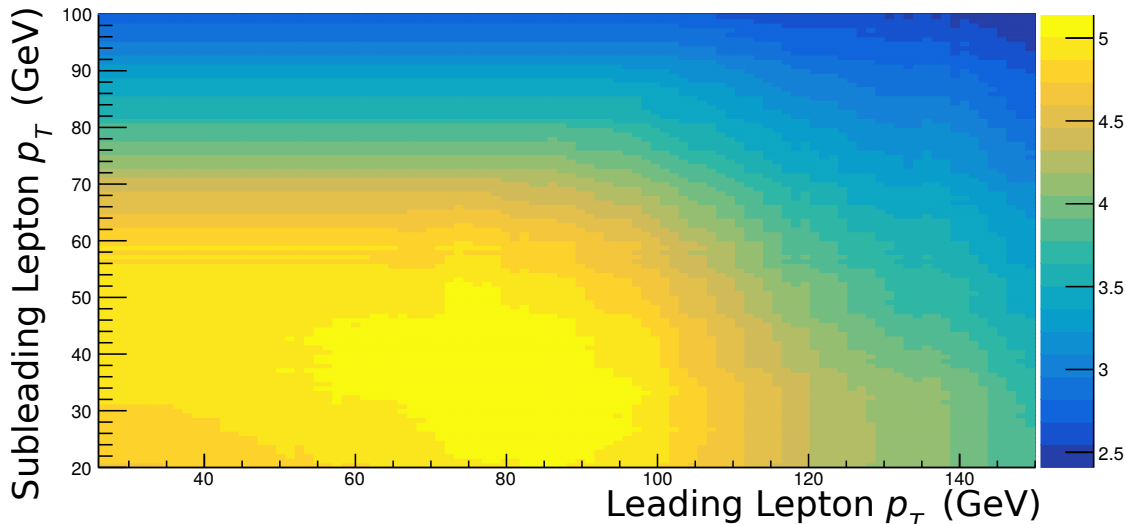

Figure 4.4: Example of significance plot in the leading vs subleading lepton p_T plane, with the third lepton $p_T \geq 14$ GeV and E_T^{miss} significance≥ 8.

cance plot (one slide is shown in Figure 4.4), the following cuts on the kinematical variables were chosen: leading lepton $p_T = 70$ GeV, subleading lepton $p_T = 35$ GeV, third lepton $p_T = 15$ GeV, E_T^{miss} significance $= 8$.

4.3.2 Discriminating variables

In order to define background-enriched regions (*control regions*, CR) and signal-enriched regions (*signal regions*, SR) a proper discriminating variable has to be found. To find the best discriminating variable, the so-called *ROC curve* will be studied, which reports the background rejection power as a function of the signal efficiency. Among all the variables analysed, it is found a good discriminating power in the invariant mass distributions of lepton pairs as a function of the chosen cut value. Since each event has three leptons, the following classification was performed. First, lepton pairs according to their charge was defined: one SS and two OS lepton pairs are possible (see Figure 4.5). Then lepton pairs are in turn divided into:

- Leading pair: formed by the most energetic leptons;

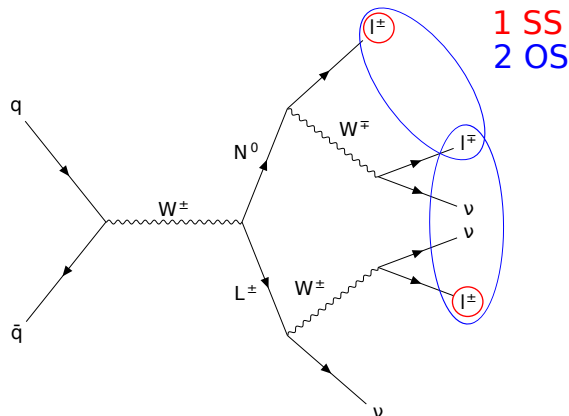- Subleading pair: composed by the least energetic leptons.

Figure 4.5: Representation of the two different types of lepton pairs in the considered final states. There are one same-sign pair (red circles) and two opposite-sign pairs (blue ellipses).

The 200 GeV signal mass sample was conservatively used since it contains the largest signal contamination in the CR. The related variables are computed and studied by looking at the corresponding ROC curves in Figure 4.6, which reports the background rejection as a function of the signal efficiency. The red line, representing the OS leading pair mass ($mllOSL$ in the following), provides the better signal efficiency and good background rejection in most of the variable range.

Based on this result, the value $mllOSL = 120$ GeV was chosen as the discriminating threshold. This choice keeps about 80% of signal events rejecting 60% of the background. In Figure 4.7 is reported the mass distributions of the OS and SS leading pairs to show the different discrimination power of the two variables.

4.4 Signal extraction technique

For the statistical data analysis, the statistical framework `HistFitter` [52] has been used. This package allows to study a potential data excess as well as to set an upper bound on the signal production cross-section as function of the mass hypothesis.

To built an hypothesis test, a likelihood (LH) function, considering all different regions defined in the analysis, is required. The LH function takes into account two different types of parameters: the *parameters of interest* (POI) and the *nuisance parameters* (NPs). The POI includes the signal strength μ, where $\mu = 0$ corresponds to the background only hypothesis and $\mu = 1$ is the signal plus background hypothesis. The most likely values of NPs and POI are obtained by the maximization of the LH in the fit. A description of the LH-based test is explained
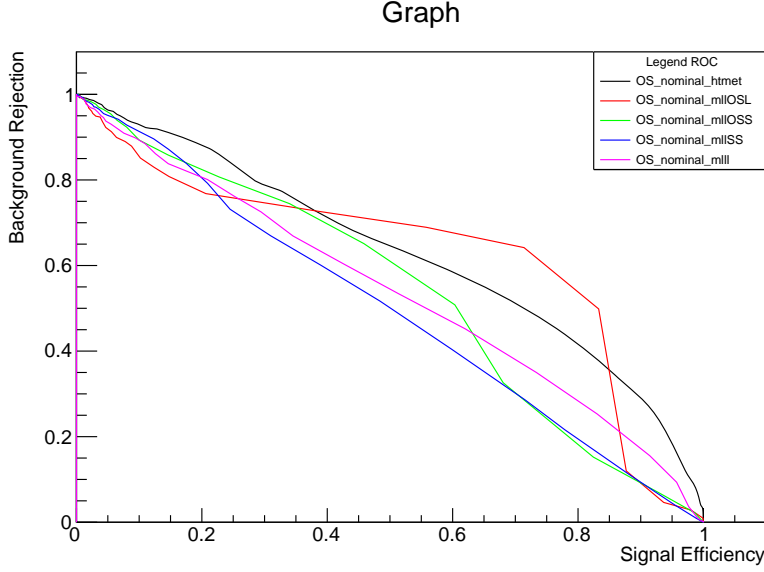
Figure 4.6: ROC curve of the main analysis variables at cuts optimization level. The lines represent the following variables: $H_T + E_T^{miss}$ (black), OS leading pair mass (red), OS subleading pair mass (green), SS pair mass (blue), three-lepton mass (magenta).The study was done using the 200 GeV signal mass sample.

in Section 4.4.2.

During the fitting procedure, systematic uncertainties are assigned to the signal and background predictions to account for possible modeling inaccuracies. In this analysis, the most influential sources of uncertainty affecting all simulated signal and background processes are the uncertainty on the total integrated luminosity and the theory uncertainties on diboson production cross-section. The uncertainty in the integrated luminosity is 2.1% [53]. The components of the uncertainty associated to the diboson production cross-section include the renormalization and factorization scales and PDF uncertainties, corresponding to 15%. This value is obtained by the difference between the predictions from different MC generators, `Sherpa` and `Powheg-Box` [54].

4.4.1 Region definition

On the basis of the study described in Section 4.3.2, the selection on the *mllOSL* variable is used to define the CR and the SR. All the analysis regions have the same physics requirements described in Section 4.2.2. Eventually CR and SR are orthogonally defined based on the cut summarised in Table 4.8. The CR defined in the analysis constrains the normalization for diboson background which
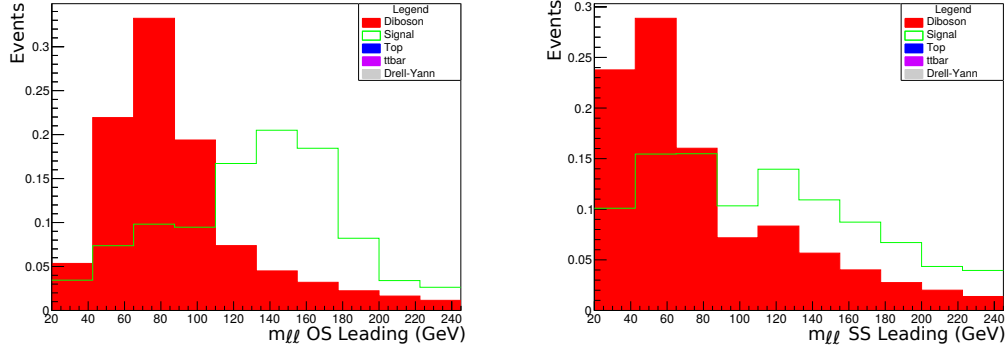
Figure 4.7: Mass distribution of the OS (left) and SS (right) leading pair. Both histograms are normalized to unity for illustration purposes.

	CR	SR
$mllOSL$ (GeV)	$[60, 120]$	$[120, \infty[$

Table 4.8: Summary of regions defined in the analysis.

is extrapolated to the SR by the fitting procedure. In Figure 4.8 the distributions of same variables in CR and SR are reported. After the analysis regions definition, it is also possible to evaluate the signal efficiency in SR and CR. The number of signals events for each analysis regions are reported in Table 4.9 with the respective efficiencies. In Appendix C the number of events in CR and SR divided for each type of the three leptons combination (see Table 4.1) are also reported.

Signal mass-point (GeV)	200	250	300	350	400
CR	420 (0.09)	333 (0.07)	263 (0.05)	183 (0.04)	164 (0.03)
SR	1294 (0.28)	2052 (0.44)	2540 (0.54)	2980 (0.61)	3212 (0.67)
Signal mass-point (GeV)	500	550	600	650	700
CR	117 (0.02)	87(0.02)	93 (0.02)	83 (0.02)	79 (0.02)
SR	3449 (0.73)	3501 (0.74)	3594 (0.76)	3470 (0.75)	3590 (0.77)

Table 4.9: The number of expected signal events for each mass-point in CR and SR are reported. The numbers in brackets represent the signal contamination (in CR) and signal selection efficiency (in SR) with respect to the last column of Table 4.6.
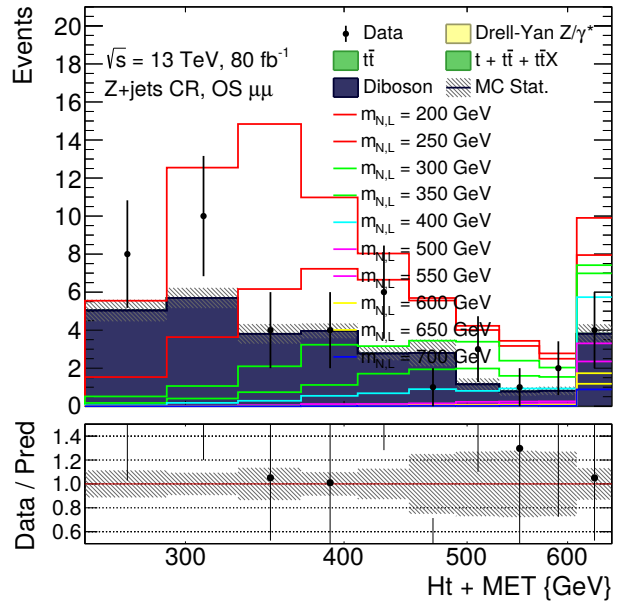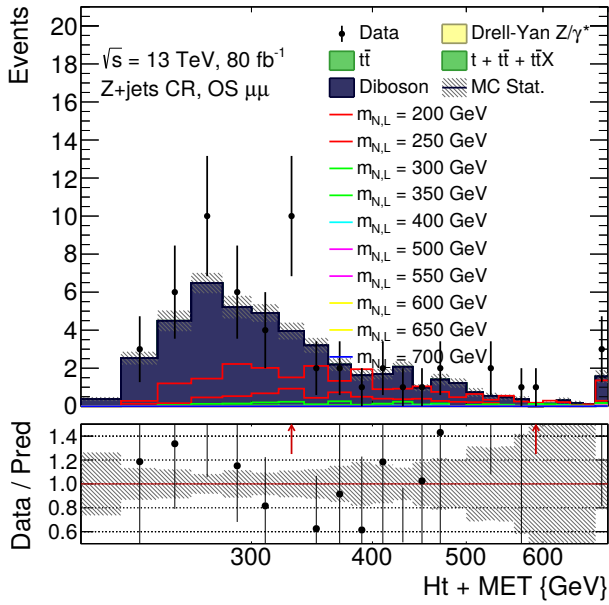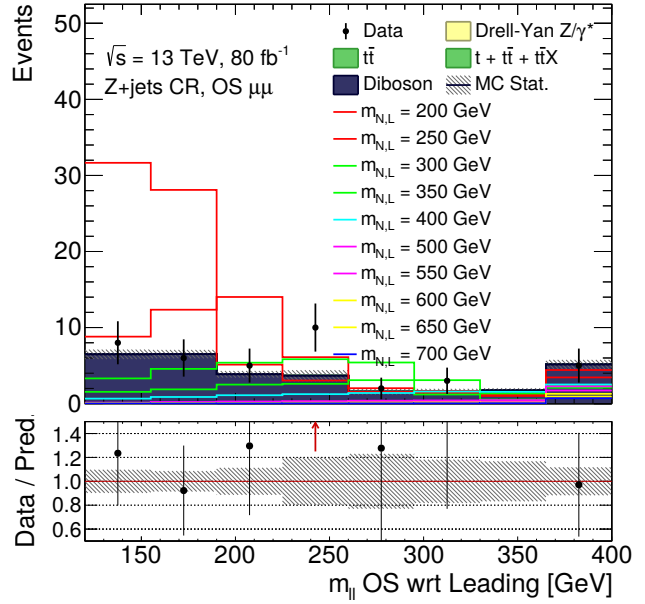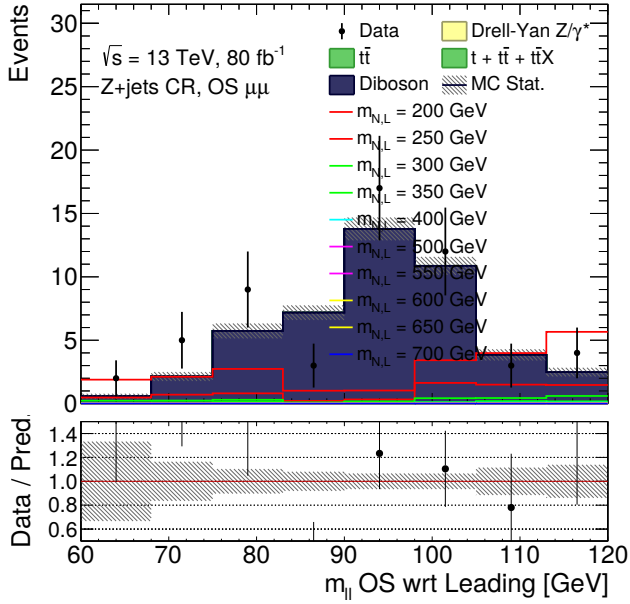
76

Figure 4.8: Distribution of $mllOSL$ mass (top) and $H_T + E_T^{miss}$ (bottom) for both SR (right) and CR (left).

4.4.2 Likelihood-based test

The LH function is defined as:

$$\mathcal{L}\left(\mathbf{n}, \boldsymbol{\theta}_0 | \mu_{sig}, \boldsymbol{\mu_b}, \boldsymbol{\theta}\right) = P_{SR} \times P_{CR} \times G_{NP}$$

$$= P\left(n_{SR} | \mu_{sig} \cdot S\left(\theta\right) + \sum_b^{bkgs} \mu_b B\left(\boldsymbol{\theta}\right)\right)$$

$$\times \prod_{i \in CR} P\left(n_{CR} | \sum_b^{bkgs} \mu_b B\left(\boldsymbol{\theta}\right)\right) \tag{4.2}$$

$$\times G_{NPs}\left(\boldsymbol{\theta}_0 | \boldsymbol{\theta}\right)$$

where P_{SR} is a Poissonian term describing the probability to observe n events given the signal plus background hypothesis

$$n_{expected} = \mu_{sig} \cdot S\left(\boldsymbol{\theta}\right) + \mu_b \cdot B\left(\boldsymbol{\theta}\right), \tag{4.3}$$

$S\left(\boldsymbol{\theta}\right)$ and $B\left(\boldsymbol{\theta}\right)$ being the expected signal and background yields depending on the nuisance parameters $\boldsymbol{\theta}$. The other parameters in the Equation 4.2 are: the number of events observed into the SR n_{SR} and the normalization factors for background and signal μ_b and μ_{sig} respectively. The second term is related to the CR and it is a product over the number of bins used to describe the variable entering the fit. The third term gives a NP parametrization constraining the *auxiliary measurements* $\boldsymbol{\theta}_0$ to its real measured value $\boldsymbol{\theta}$. The functions G_{NPs} can be a Gaussian or a Poissonian type. Systematic uncertainties are usually modelled using Gaussian functions, while Poissonian functions are used for the statistical uncertainties.

4.4.3 Hypothesis Test

A *test statistic* variable q_μ is defined to obtain the expected 95% *confidence level* (CL) limit on the production cross-section of signal events. It is evaluated using the *profile likelihood ratio* test, defined as:

$$q_\mu = -2 \cdot \ln \frac{\mathcal{L}\left(\mu, \hat{\boldsymbol{\theta}}_\mu\right)}{\mathcal{L}\left(\hat{\mu}, \hat{\boldsymbol{\theta}}\right)} \tag{4.4}$$

where $\hat{\mu}$ and $\hat{\boldsymbol{\theta}}$ maximize the LH function and $\hat{\boldsymbol{\theta}}_\mu$ maximize the LH for the specific value of the signal strength μ. The test-statistic is positive-defined. A q_μ value close to zero suggests a signal-like data distributions while a larger q_μ a background-like data distributions.

The PDF of the test statistic, $f(q_\mu|\text{hypothesis})$, must be determined to derive the CLs limits. The p-values corresponding to a background only hypothesis, p_B, and corresponding to a signal plus background hypothesis, p_{S+B}, for an observed value of the test-statistic $q_{\mu,obs}$, are defined as:

$$p_B = \int_{-\infty}^{q_{\mu,obs}} f(q_\mu|B)\, dq_\mu \tag{4.5}$$

$$p_{S+B} = \int_{q_{\mu,obs}}^{\infty} f(q_\mu|S+B)\, dq_\mu \tag{4.6}$$

To define the CL these two quantities are computed with the same $q_{\mu,obs}$. The excluded μ at 95% CL is defined requiring [55]:

$$\text{CLs} = \frac{p_{S+B}}{1 - p_B} < 5\%. \tag{4.7}$$

4.4.4 Fit Results

Two types of fit are used in this analysis: the *background only fit* which evaluates normalization of the background in CR, and the *exclusion fit* which sets the limits on the production cross section of the new particles.

The distribution which is fitted in the CR is the *mllOSL*, to extract the diboson normalization factor and extrapolate it to the SR. The normalization factor obtained after the background-only fit is:

$$\mu_b = 1.17 \pm 0.16 \tag{4.8}$$

compatible with one within the uncertainties. In Figure 4.9 the pre-fit and post-fit distributions in the CR are shown. After the background only fit, the exclusion fit is performed, combining control and signal regions. The distributions which are fitted in the SR is the variable $H_T + E_T^{miss}$. The choice of this fitting variable in the SR is due to the larger sensitivity to the shapes of the distribution in this region (bottom plots of Figure 4.8). The signal region is fitted under the hypothesis of a signal strength for heavy lepton production with $\mu = 1$. All heavy leptons masses with a fitted μ parameter below one can be excluded. On the contrary, the analysis is not enough sensitive to exclude all the heavy leptons mass points with a post-fit $\mu > 1$. The pre-fit and post-fit distributions in signal regions are presented in Figure 4.10. A good agreement between data and MC background simulation is observed before the fitting procedure in the SR, which is improved after the fit reaching a ratio close to one. Since no excess over the SM predictions are found, a limit on the heavy lepton cross section can be derived. The expected 95% CL exclusion plot with one and two standard deviation bands superimposed is shown

in Figure 4.11 with dashed lines. The theoretical cross-sections for both the heavy leptons are presented in red lines. The continuous black line is the experimental (observed) limit. The point in which the theoretical cross-section curve crosses the observed limit sets the lower mass limit. The observed lower mass limit of the Type-III Seesaw heavy leptons is $421^{+59.9}_{-53.7}$ GeV while the expected 95% CL cross-section upper limit reaches 5 fb at large mass values.
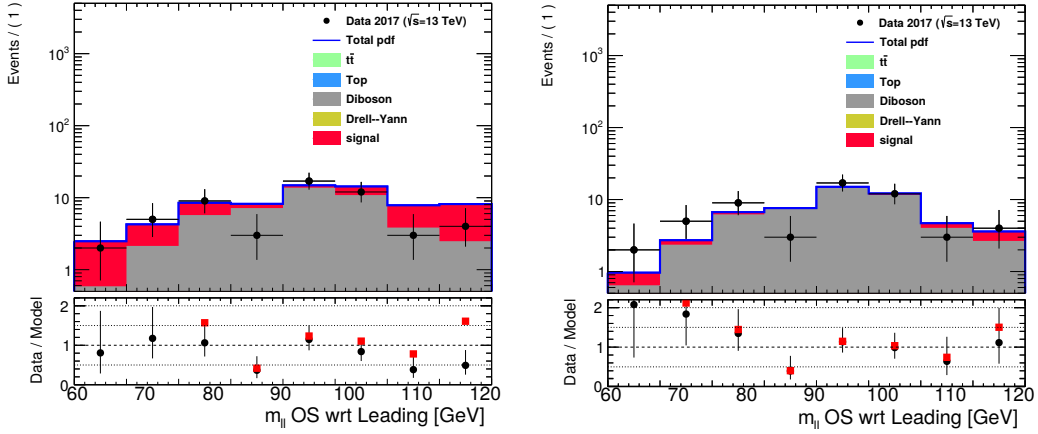
Figure 4.9: Pre-fit (left) and post-fit (right) *mllOSL* distribution for data and SM background predictions in the 3l channel in the CR. Here an integrated luminosity of 79.8 fb^{-1} is used.
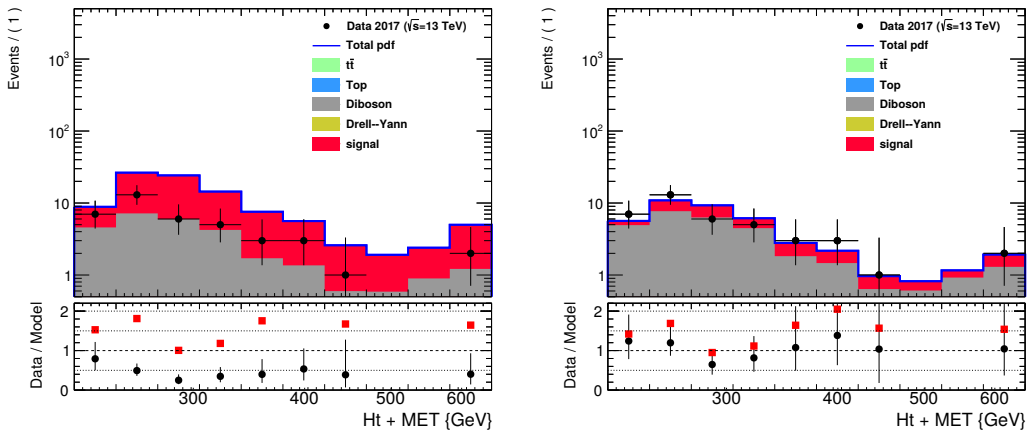

Figure 4.10: Pre-fit (left) and post-fit (right) *mllOSL* distributions for data and SM background predictions in the 3l channel in the SR. Here an integrated luminosity of 79.8 fb^{-1} is used.
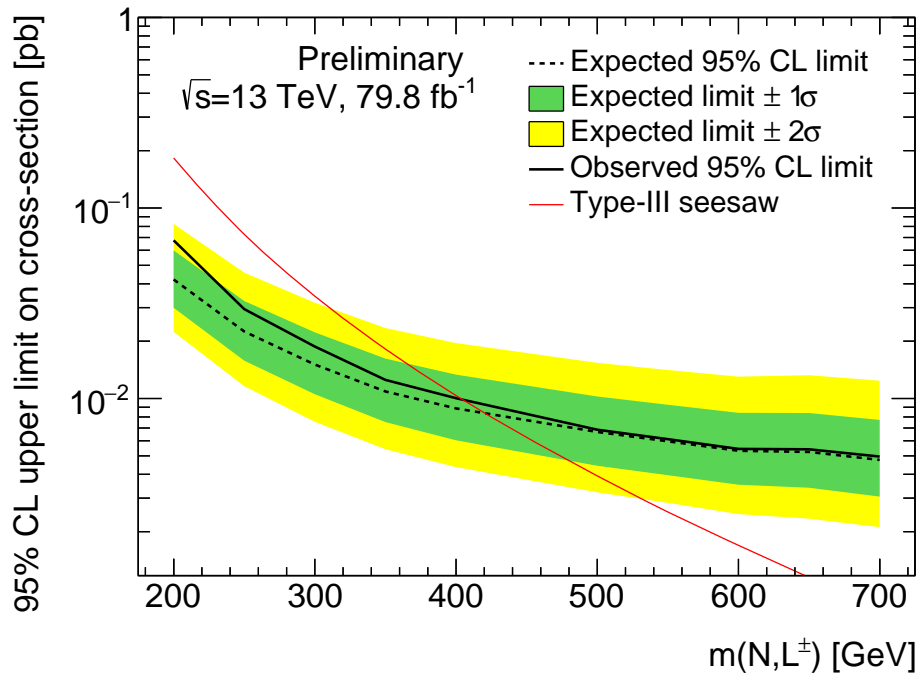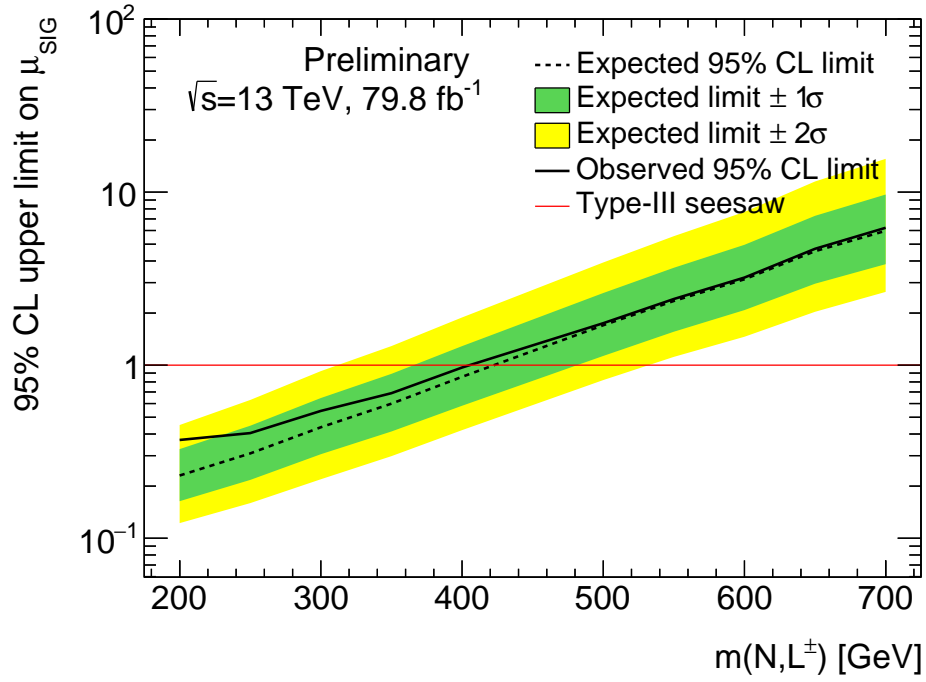
Figure 4.11: 95% CL upper limits for the cross-section (bottom) and the signal strength (top) of the Type-III Seesaw process, for the Type-III Seesaw process with the corresponding one and two standard deviation bands.

CHAPTER 5

CONCLUSIONS AND PERSPECTIVES

This work reports the results of the search for the production of Type-III Seesaw heavy leptons in the three lepton final state at the LHC, using data collected by the ATLAS detector in pp-collision at $\sqrt{s} = 13$ TeV in the years 2015, 2016 and 2017. The Type-III Seesaw mechanism explain in an elegant way the origin and the smallness of neutrinos masses.

In this thesis, the kinematical selection used to efficiently separate signal from background events was presented. Then, two analysis regions, enriched in signal and background respectively, were defined and used together in a statistical fit to extract the final value for the heavy leptons signal strength. The systematic uncertainties considered in this work are related to the uncertainty on the measurement of the integrated luminosity and on the diboson production cross-section. The analysis used a dataset corresponding to a total integrated luminosity of 79.8 fb^{-1}. No excesses over the SM background predictions were observed and no evidence for heavy leptons production was found. A lower limit on their mass was set at $421^{+59.9}_{-53.7}$ GeV at 95% confidence level.

This analysis can be considered the first step of a more general analysis which will include all Run 2 data set. Possible improvements of the analysis could be the inclusion of refined data-driven techniques for mis-reconstructed objects estimation. In the three-lepton final state, the leading background is due to diboson prompt decays to leptons and this is confirmed by the agreement between data and simulation, observed in the analysis control region. However, smaller background components, such as fake leptons from b-jets or electron charge-flips, here included in the simulation, could be directly estimated from the data. Furthermore, the inclusion of hadronically decaying τ-leptons and the heavy leptons decays into Z or Higgs bosons, will increase the sensitivity of the analysis.

This analysis provided a sensitivity similar to the 2l2j final state. Therefore, a combination of the two final states will eventually increase the sensitivity to heavy lepton production.

APPENDIX A

BACKGROUND OBJECTS

A.1 *Fake* leptons

Non-prompt leptons arise from hadrons decays, originated from the heavy or light quarks, inside a jet where they are reconstructed as originating from the IP. Then, non-prompt leptons are real leptons with a fake origin identification (see Figure A.1). For the electrons there is another background source which comes from
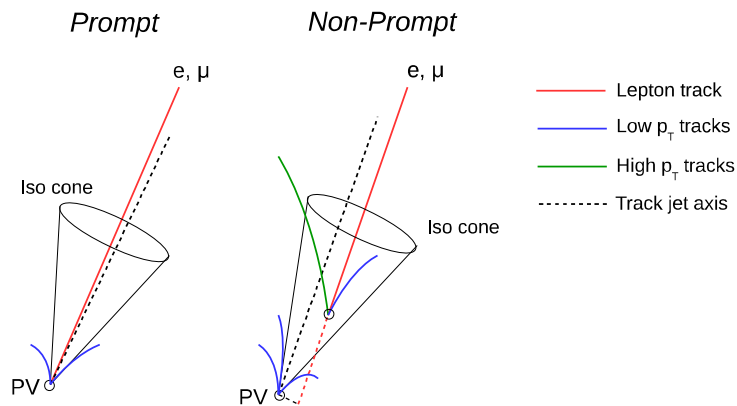

Figure A.1: Illustration of a prompt and non-prompt event. Electrons or muons originate from the secondary vertex are selected as fake leptons coming from the primary vertex.

jets production in the IP. Electrons and electrically charged component of an

hadronic jets provide a similar signal in the ID and deposit in the ECAL. If some information about the jet track from the ID is lost, it can be identified as a *fake* lepton. Simulations can not give precise measurement of these processes, then a very high MC statistics and a data-driven techniques to improve their estimation are needed.

An estimation method, the *Fake-factor Method* is described in the following.

A.1.1 Fake-factor Method

The Fake-factor method (FF) is a simplified[1] data-driven procedure used to model background from particle misidentification. The FF method selects a control sample of events enriched in the background being estimated (control region), and then use an extrapolation technique to relate these events to the background in the region rich of signal (signal region). To search electron or muon fakes, two different sets of identification criteria are used: *Tight* (*T*) and *Loose* (*L*) (see Sections 3.1.1 and 3.2.1). The weight (called "fake factor") of the events containing fake leptons is calculated using the misidentification probability for a fake lepton to satisfy the selection requirement of a prompt one. This probability is defined as the *fake rate f*

$$f = \frac{N_{pass}}{N_{pass} + N_{fail}},$$ (A.1)

where N_{pass} and N_{fail} are the number of fake leptons which satisfy and fail the identification requirement, respectively.

Then, the fake factor is defined as:

$$F = \frac{f}{1 - f} = \frac{N_{pass}}{N_{fail}}$$ (A.2)

F is measured as function of some kinematic variables and it is applied to fakes taken from data in control regions with different combinations of lepton definitions.

The extrapolation of fake background into the signal region can be obtained summing on all events in regions with a leading, subleading or third lepton identified as loose. A fake factor F is considered for each lepton candidates. The prompt contribution is evaluated with MC simulations.

---

[1]FF is derived from the Matrix Method which is a more complex technique to evaluate prompt background.

A.2   Charge Electrons Misidentification

In the channels which involve leptons pairs with at least one electron, the misidentification of the prompt electrons charge (the so called *charge-flip*) causes a large background contamination in the SS electron channels. It is due to events with two OS electrons where one is charge-flipped. A representation of this event is illustrated in Figure A.2.
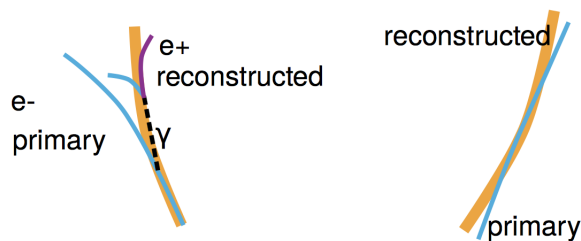

Figure A.2: Simplified representation of the electron charge mis-identification process due to electron interaction with the detector material.

Two different categories of physics processes bring to this type of background:

Trident events: these events are originated by the interaction between the electrons and the detector material producing bremsstrahlung processes ($e^{\pm} \rightarrow e^{\pm}\gamma^* \rightarrow e^{\pm}e^+e^-$). Then, with the photon conversion into an electron-positron pair, trigger requirements can be wrongly satisfied. The bremsstrahlung process can produce a wrong electron track matching inside the ECAL or also an EM shower inside the ID loosing the information of the original track;

Stiff tracks: in these events the radiated photon does not convert into a pair and the electron energy is correctly reconstructed in the ECAL. However, due to the few hits in the track and the momenta reconstruction, a charge-flip can occur.

For muons[2], charge misidentification can only be of the stiff tracks type.
To the complex and hard simulation of these events an accurate description of the detector material would be needed. Furthermore, a data-drive approach to measure the probability of an electron charge misidentification is used. The derived scale factor is then applied to SS pairs events.
Charge-flip probability is measured using data events with a Z decay into an

---

[2]Due to its high mass, muon has a smaller probability than electrons to involve into a bremsstrahlung process up to p_T of few hundreds of 100 GeV.

electron-positron pair, requiring the invariant mass of this pair to be into the Z mass window. The background is mainly composed by diboson events, top decays and fake electrons from $W +$ jets events which involve contamination in the SS regions. These events are mostly evident studying p_T and η distributions.

To the charge-flip measurements, the OS and SS pairs of Z decay are used (see Figure A.3). The SS peak is shifted by   1.5 GeV to lower energies with a larger width with respect to the OS pair, it is due to the energy loss during photon emission described before. SS electrons are selected to this measure because of it is assumed that one has incorrectly measured charge, coming from $Z \to ee$ only OS pairs are expected. The total number of electron pairs can be divided following
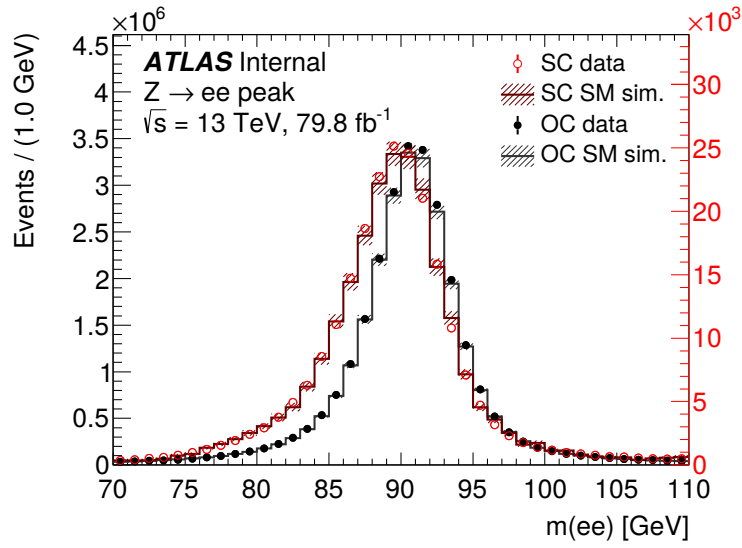

Figure A.3: $Z \to ee$ peak for opposite-sign (black) and same-sign (red) electrons, measured with the analysis objects and derived charge-flip scale factors already applied.

the charge: $N^{ij} = N^{ij}_{SS} + N^{ij}_{OS}$. The probability to observe SS events is a Poissonian probability:

$$f\left(N^{ij}_{SS}; \lambda\right) = \frac{\lambda^{N^{ij}_{SS}} e^{-\lambda}}{N^{ij}_{SS}!} \tag{A.3}$$

where $\lambda = \left(\epsilon_i \left(1 - \epsilon_j\right) + \epsilon_j \left(1 - \epsilon_i\right)\right) N^{ij}$ is the expected number of SS events in bin (i, j) given the charge misidentification probabilities ϵ_i and ϵ_j and N^{ij}_{SS} is the measured number of SS events.

Using a likelihood fit summing all the probabilities reported into Eq.A.3 and minimizing the likelihood, the charge-flip rates can be extracted. This procedure can

be obtained constructing a negative logarithm of the summed likelihood:

$$-\log\mathcal{L}\left(\vec{e}|\vec{N}_{SS}, \vec{N}\right) \approx \sum_{i,j} \log\left(N^{ij}\left(\epsilon_i\left(1-\epsilon_j\right) + \epsilon_j\left(1-\epsilon_i\right)\right)\right) N_{SS}^{ij}$$
$$-N^{ij}\left(\epsilon_i\left(1-\epsilon_j\right) + \epsilon_j\left(1-\epsilon_i\right)\right). \tag{A.4}$$

Likelihood can be minimized exploiting the ROOT minimization interface with `MINUIT2` package and `MIGRAD`.
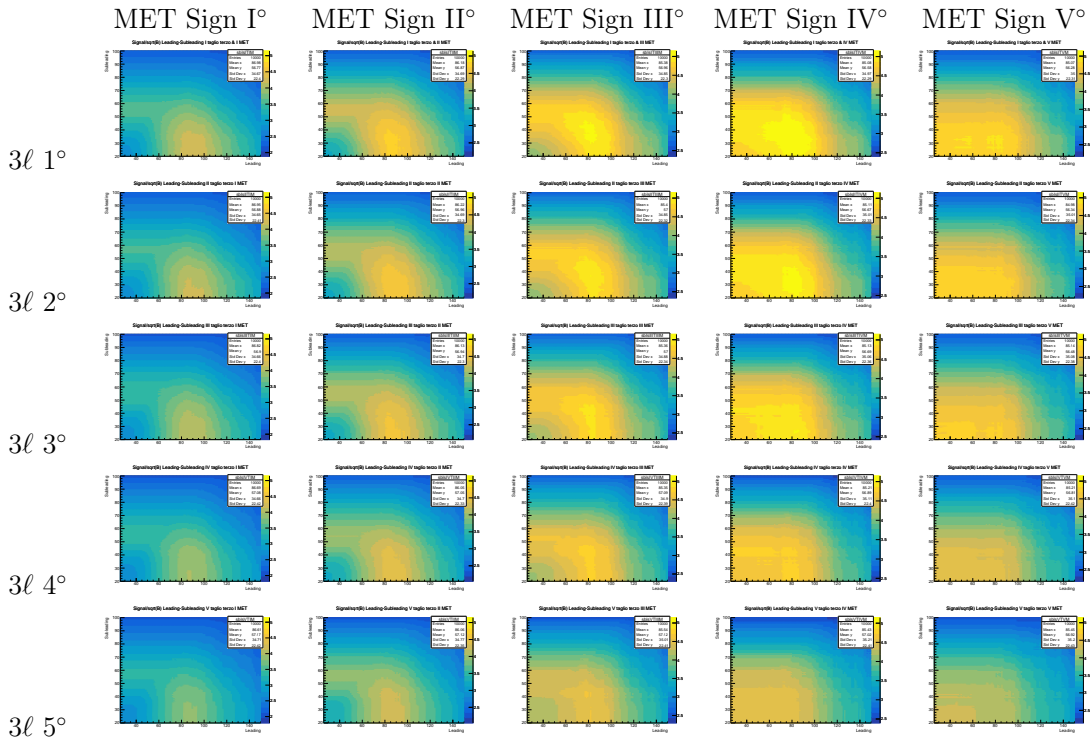
APPENDIX B

SIGNIFICANCE PLOT

Table B.1: Matrix overview of the multi-dimensional significance plots. They are ordered following third lepton p_T cuts on the rows and MET Significance cuts on the columns.

APPENDIX C

TOPOLOGICAL FINAL STATES

Signal mass-point (GeV)	200	250	300	350	400	500	550	600	650	700
$\mu^- e^+ e^+$	32	25	21	20	16	12	6	10	12	8
$\mu^+ e^- e^-$	15	18	7	6	4	6	3	5	1	4
$e^- \mu^+ \mu^+$	20	27	28	22	18	13	7	8	8	5
$e^+ \mu^- \mu^-$	9	8	10	6	7	7	4	5	3	2
$\mu^- e^+ \mu^+$	80	67	57	36	26	21	20	16	16	11
$\mu^+ e^- \mu^-$	53	28	22	10	14	8	6	9	5	7
$e^- e^+ \mu^+$	73	53	42	33	30	15	13	16	11	12
$e^+ e^- \mu^-$	40	27	19	8	13	5	5	3	8	5
$e^- e^+ e^+$	31	30	25	16	8	9	7	6	11	9
$e^+ e^- e^-$	18	16	8	5	5	3	6	6	3	5
$\mu^- \mu^+ \mu^+$	31	24	12	9	19	10	8	7	4	7
$\mu^+ \mu^- \mu^-$	18	10	12	12	4	8	2	2	1	4

Table C.1: Number of events for each topology in the CR.

Signal mass-point (GeV)	200	250	300	350	400	500	550	600	650	700
$\mu^- e^+ e^+$	110	165	203	283	259	325	325	338	324	342
$\mu^+ e^- e^-$	69	102	108	123	127	135	130	158	127	133
$e^- \mu^+ \mu^+$	128	180	241	249	293	340	330	314	299	324
$e^+ \mu^- \mu^-$	64	83	117	124	145	138	123	142	125	123
$\mu^- e^+ \mu^+$	221	341	442	497	584	590	603	668	614	634
$\mu^+ e^- \mu^-$	122	187	217	236	250	251	254	218	237	241
$e^- e^+ \mu^+$	180	367	417	512	571	609	676	680	675	705
$e^+ e^- \mu^-$	124	191	213	282	248	276	273	260	266	252
$e^- e^+ e^+$	103	154	189	243	274	293	301	358	324	366
$e^+ e^- e^-$	49	81	125	131	126	138	142	131	149	130
$\mu^- \mu^+ \mu^+$	80	126	197	208	220	253	249	234	230	246
$\mu^+ \mu^- \mu^-$	44	75	71	92	115	101	95	93	100	94

Table C.2: Number of events for each topology in the SR.

BIBLIOGRAPHY

[1] C. Quigg, "Gauge Theories of the Strong, Weak and Electromagnetic Interactions", Westview Press (1983)

[2] H. Fritzsch, M. Gell-Mann, H. Leutwyler. "Advantages of the color octet gluon picture". In: *Phys. Lett. B* 47 (1973), pp.365-368. ISSN: 0370-2693. DOI:10.1016/0370-2693(73)90625-4

[3] L.S. Glashow. "The renormalizability of vector meson interactions". In *Nuclear Physics* 10 (1959), pp.107-117. ISSN: 0029-5582. DOI:10.1016/0029-5582(59)90196-8

[4] S. Weinberg, J. C. Ward. "A Model of Leptons". In: *Phys. Rev. Lett.* 19 (1967), pp.1264-1266. ISSN: 1079-7114. DOI:10.1103/PhysRevLett.19.1264

[5] A. Salam. "Weak and electromagnetic interactions". In:*Il Nuovo Cimento* 11 (1959), pp.568-577. ISSN: 1827-6121. DOI:10.1007/BF02726525

[6] P. W. Higgs. " Spontaneous Symmetry Breakdown without Massless Bosons". In:*Phys. Rev.* 145 (1966), pp.1156-1163. ISSN: 1536-6065. DOI:10.1103/PhysRev.145.1156

[7] C. Patrignani et al. "Particle Data Group". In: *Chinese Phys. C* 40 (2006), pp.100001. DOI:10.1088/1674-1137/40/10/100001

[8] R. Feynman, "QED: The Strange Theory of Light and Matter ", Princeton University Press (1985)

[9] E. Fermi, "Tentativo di una teoria dei raggi β", in *Il Nuovo Cimento*, Societ 'a Italiana di Fisica (1934)

[10] K. Kleinknecht "CP Violation and K Decays", in *Annual Review of Nuclear Science* 26 (1976), pp.1-50. DOI:10.1146/annurev.ns.26.120176.000245

[11] N. Cabibbo "Unitary Symmetry and Leptonic Decays", in *Phys. Rev. Lett.*, 101 (1963), pp. 531-533. DOI:10.1103/PhysRevLett.10.531

[12] M. Kobayashi, T. Maskawa "CP-Violation in the Renormalizable Theory of Weak Interaction", in *Progress of Theoretical Physics* 49 (1973), pp.652-657. DOI:10.1143/PTP.49.652

[13] M. E. Peskin , D. V. Schroeder "An Introduction to Quantum Field Theory", Perseus Books (1995)

[14] D. Gross, F. Wilezek "Soft Strong Interaction - the asymptotic freedom of quarks", in *Phys. Rev. Lett.*, B30 (1973). pp.1343.DOI:10.1103/PhysRevLett.30.1343

[15] W. Pauli "Wissenschaftlicher Briefwechsel mit Bohr, Einstein, Heisenberg u.a. - Band II: 1930-1939", edited by Karl von Meyenn *Springer-Verlag Berlin Heidelberg New York Tokyo* (1985). pp. 39-41.

[16] M. Conversi, E. Pancini, O. Piccioni "On the Disintegration of Negative Mesons", in *Physical Review* 71 (1947). pp. 209-210. DOI:10.1103/PhysRev.71.209

[17] G. Danby, J. M. Gaillard, K. Goulianos, L. M. Lederman, N. Mistry, M. Schwartz, J. Steinberger "Observation of High-Energy Neutrino Reactions and the Existence of Two Kinds of Neutrinos", in *Phys. Rev. Lett.* 9 (1962). pp. 36-44. DOI:10.1103/PhysRevLett.9.36

[18] B. Pontecorvo "Electron and Muon Neutrinos", in *Journal of Experimental and Theoretical Physics.* 10 (1960). pp. 12361240.

[19] Super-Kamiokande Collaboration, Fukuda Y. et al "Evidence for oscillation of atmospheric neutrinos", in *Phys. Rev. Lett.* 81 (1998). pp. 1562-1567. DOI:10.1103/PhysRevLett.81.1562

[20] N. Arkani-Hamed, M. Schmaltz "Hierarchies without symmetries from extra dimensions", in *Phys. Rev. D* 61 (2000). 033005. DOI:10.1103/PhysRevD.61.033005

[21] M. Drewes "The phenomenology of right handed neutrinos", in *International Journal of Modern Physics E* 22 (2013). DOI:10.1142/S0218301313300191

[22] E. Majorana "Teoria simmetrica dellelettrone e del positrone", in *Il Nuovo Cimento* 14 (1937). pp. 171. DOI:10.1007/BF02961314

[23] T. Yanagida "Horizontal Symmetry and Masses of Neutrinos", in *Progress of Theoretical Physics* 64 (1980). pp. 11031105. DOI:10.1143/PTP.64.1103

[24] F. Bonneta, D. Hernandezb, T. Otac, W. Winter "Neutrino masses from higher than d = 5 effective operators", in *Journal of High Energy Physics* (2009). DOI:10.1088/1126-6708/2009/10/076

[25] R. Henning "Current status of neutrinoless double-beta decay searches", in *Reviews in Physics* 1 (2016). pp. 29-35. DOI:10.1016/j.revip.2016.03.001

[26] L.H. Ryder "Quantum Field Theory" Cambridge University Press (1996)

[27] B. Adhikary, P. Roy "Neutrino Yukawa textures within type-I see-saw", in *Advanced High Energy Physics* (2013). DOI:10.1155/2013/324756

[28] A. Melfo et al. "Type II Seesaw at LHC: The Roadmap", in *Phys.Rev. D* 85 (2012). DOI:10.1103/PhysRevD.85.055018

[29] S.M. Barr, I. Dorsner "A Prediction from the type III see-saw mechanism", in *Physics Letter B* 632 (2006). pp. 527-531.10.1016/j.physletb.2005.10.080

[30] P.F. Pé rez " Type III Seesaw and left-right symmetry", in *Journal of High Energy Physics* 03 (2009). pp. 142. DOI:10.1088/1126-6708/2009/03/142

[31] T. Novak, M. Franchini, A. Gorisek, B.P. Kersevan, E. Lytken, K.H. Mankinen, M. Mikuz, M.Muskinja, F. Scutti, A. Sidoti, M. Sioli, G. Ucchielli "Search for type-III seesaw heavy leptons using proton-proton collisions at $\sqrt{s}$ = 13 TeV with the ATLAS detector", in *ATL-COM-PHYS-2018-051*, 2018. https://cds.cern.ch/record/2301920

[32] Arindam Das "Searching for the Minimal Seesaw Models at the LHC and Beyond". In *Advances in High Energy Physics* 2018 (2018), pp.16. 10.1155/2018/9785318

[33] ATLAS Collaboration. "Search for Type-III SeeSaw heavy leptons in *pp* collisions at $\sqrt{s}$ = 8 TeV with the ATLAS Detector". In: *Phys. Rev. D* 92 (2015), p. 032001. DOI:10.1103/PhysRevD.92.032001

[34] CMS Collaboration. "Search for heavy lepton partners of neutrinos in protonproton collisions in the context of the type III seesaw mechanism". In: *Phys. Rev. B* 718 (2012), p.348-368. DOI:10.1016/j.physletb.2012.10.070

[35] A. M. Sirunyan *et al.* [CMS Collaboration], "Search for Evidence of the Type-III Seesaw Mechanism in Multilepton Final States in Proton-Proton Collisions at $\sqrt{s}$ = 13 TeV," Phys. Rev. Lett. **119** (2017) no.22, 221802. `DOI:`10.1103/PhysRevLett.119.221802

[36] A. Ahriche, A. Jueid, S. Nasri "Radiative Neutrino Mass & Majorana Dark Matter within an Inert Higgs Doublet Model", in *Phys. Rev. D* 97 (2018). pp. 095012. `DOI:`10.1103/PhysRevD.97.095012

[37] LHC Commissioning, "LHC 2017 Performance" https://lhc-commissioning..2017-performance.htm

[38] ATLAS Collaboration " Photon and electron identification with the AT-LAS detector ", in *Proceedings of Science* ICHEP2016 (2016). pp. 1235. `DOI:`10.22323/1.282.1235

[39] ATLAS Collaboration "Electron efficiency measurements with the AT-LAS detector using the 2015 LHC proton-proton collision data", in *51st Rencontres de Moriond on QCD and High Energy Interactions* (2016). https://cds.cern.ch/record/2157687

[40] K. Brendlinger, I.J. Kroll "Physics with Electrons in the ATLAS Detector", in CERN-THESIS-2016-144 (2018). https://cds.cern.ch/record/2228644

[41] ATLAS Collaboration "Electron efficiency measurements with the ATLAS detector using 2012 LHC proton-proton collision data. Electron efficiency measurements with the ATLAS detector using 2012 LHC proton-proton collision data", in *Eur. Phys. J. C* 77 (2016) pp. 195. https://cds.cern.ch/record/2237544

[42] ATLAS Collaboration " Muon reconstruction performance of the ATLAS detector in proton–proton collision data at $\sqrt{s}$ = 13 TeV", in *Eur.$\tilde{P}$hys.$\tilde{J}$.* C76 (2016) pp. 292. `DOI:`10.1140/epjc/s10052-016-4120-y

[43] ATLAS Collaboration "Performance of the ATLAS Trigger System in 2015", in *Eur.$\tilde{P}$hys.$\tilde{J}$.* C77 (2017). pp. 317. `DOI:`10.1140/epjc/s10052-017-4852-3

[44] ATLAS Collaboration "Jet energy measurement and its systematic uncertainty in proton-proton collisions at $\sqrt{s}$=7 TeV with the ATLAS detector", in *Eur. Phys. J.* C75 (2015). `DOI:`10.1140/epjc/s10052-014-3190-y

[45] ATLAS Collaboration "Tagging and suppression of pileup jets with the ATLAS detector", in ATLAS-CONF-2014-018 (2014). https://cds.cern.ch/record/1700870

[46] ATLAS Collaboration "Jet energy scale measurements and their systematic uncertainties in proton-proton collisions at $\sqrt{s}$=13 TeV with the ATLAS detector", in *Phys. Rev. D* 96 (2017). pp. 072002. `DOI:`10.1103/PhysRevD.96.072002

[47] ATLAS Collaboration " ATLAS jet and missing energy reconstruction, calibration and performance in LHC Run-2", in *JINST* 12 (2017). pp. C06038. `DOI:`10.1088/1748-0221/12/06/C06038

[48] A. Dell'Acqua "Athena: Inside the ATLAS Software Framework" http://www.bo.infn.it/coordinatorI/Seminari/2005/dellacqua_athena.pdf

[49] Derivation Framework https://twiki.cern.ch/twiki/bin/viewauth/AtlasProtected/DerivationFramework

[50] G. Cowan, E. Gross "Discovery signicance with statistical uncertainty in the background estimate", in *ATLAS Statistics Forum* (2008). https://www.pp.rhul.ac.uk/ cowan/stat/notes/SigCalcNote.pdf

[51] C.P. Bhat "Multivariate Analysis Methods in Particle Physics", in *Annual Review of Nuclear and Particle Science* 61 (2011) pp. 281. `DOI:`10.1146/annurev.nucl.012809.104427

[52] M. Baak et al. " HistFitter software framework for statistical data analysis", in *Eur. Phys. J.* C75 (2015) pp. 153. `DOI:`10.1140/epjc/s10052-015-3327-7

[53] ATLAS Collaboration " Search for resonant WZ production in the fully leptonic final state in proton-proton collisions at $\sqrt{s}$=13 TeV with the ATLAS detector" in *High Energ. Phys. - Experiment* (2018). arXiv:1806.01532

[54] ATLAS Collaboration "Search for heavy lepton resonances decaying to a Z boson and a lepton in pp collisions at $\sqrt{s}$= 8 TeV with the ATLAS detector" in *High Energ. Phys.* (2015). `DOI:`10.1007/JHEP09(2015)108

[55] D.R. Cox , D.V. Hinkley "Theoretical Statistics" Chapman & Hall (1974)

[56] ATLAS Collaboration. "Search for doubly charged Higgs bosons in like-sign dilepton final states at $\sqrt{s} = 7$ TeV with the ATLAS detector". In: *Eur. Phys. J.* C72 (2012), p.2244. `DOI:`10.1140/epjc/s10052-012-2244-2

[57] G. Corcella, C. Corianò, A. Costantini, P.H. Frampton. "Bilepton signatures at the LHC". In: *Phys. Lett. B* 773 (2017), pp. 544-552. `ISSN:` 0370-2693. `DOI:`10.1016/j.physletb.2017.09.015

[58] R. Franceschini, T. Hambye, A. Strumia. "Type-III seesaw mechanism at CERN LHC". In: *Phys. Rev. D* 78 (2008), p. 033002. DOI:10.1103/PhysRevD.78.033002

[59] P. Bandyopadhyay, S. Choi, E.J. Chun, K. Min. "Probing Higgs bosons via the type III seesaw mechanism at the LHC". In: *Phys. Rev. D* 85 (2012), p. 073013. DOI:10.1103/PhysRevD.85.073013